

INTERFACIAL MECHANISMS UNDERSTANDING AND
MATERIAL DESIGN FOR LITHIUM-SULFUR BATTERIES
VIA AN INTEGRATED COMPUTATIONAL APPROACH

By

Yuxiao Lin

A DISSERTATION

Submitted to
Michigan State University
in partial fulfillment of the requirements
for the degree of

Materials Science and Engineering — Doctor of Philosophy

2019

ABSTRACT

INTERFACIAL MECHANISMS UNDERSTANDING AND MATERIAL DESIGN FOR LITHIUM-SULFUR BATTERIES VIA AN INTEGRATED COMPUTATIONAL APPROACH

By

Yuxiao Lin

Lithium-Sulfur (Li-S) batteries promise high energy density and low cost, but is hindered by the rapid capacity and energy fading. In this thesis, several integrated computational models were developed to connect the electrode-electrolyte interface mechanisms with the discharge curves and capacity loss. The new insights were used to design the electrodes and electrolyte.

Between the Li anode and the electrolyte, the formation of an electrical insulating solid electrolyte interphase (SEI) is responsible for the initial irreversible capacity loss. Assuming the electron tunneling from the electrode to the electrolyte was blocked by the SEI inorganic components at a critical thickness, based on the results from density functional theory (DFT), an analytical model was developed to connect the initial irreversible capacity loss with the anode surface area. Good agreement with experimental measurements confirmed that the initial irreversible capacity loss was due to the self-limiting electron tunneling property of the SEI.

In typical cathodes, elemental sulfur is embedded in a carbon matrix. During discharging, soluble long-chain Li polysulfides (Li-PSs) were generated before the insoluble insulating Li_2S . In this thesis, it was found that the solvation status of Li-PS (fully, partially, or not dissolved) had a profound impact on discharging curves. The open circuit voltage (OCV) was first predicted using DFT calculated free energies at finite temperatures including solvation energy. This model revealed that the solvation stabilized the Li-PS. Thus, the formation of fully solvated Li-PS led to two-plateaued OCV; while non-solvated Li-PS is not favorable, so the direct transition from S to Li_2S led to one-plateaued OCV. Practically, the solvation status of

the Li-PS is related to electrolyte volume. A mechanism based analytical model was developed to illustrate the micrometer level porosity determined discharging curve by connecting electrolyte amount, pore volume, Li-PS solubility and carbon matrix surface area. This model was used to optimize the porosity to maximize the volumetric energy density of Li-S batteries.

Dissolved Li-PSs can diffuse in the electrolyte, and precipitate as insulating Li_2S on electrode surfaces, leading to quick capacity and energy drop. Nanopore and sub-nanopore size were important in controlling the Li-PS solvation status to prevent Li-PS shuttling. The Li-PS formation could be suppressed when partially solvated, suggested by DFT. Since decreasing pore size to nanometer level and increasing electrolyte concentration could both create partially solvated Li-PS, a new strategy to mitigate “Li-PS shuttle problem” based on this synergetic effect was proposed by modeling and verified by experiments. A more idealized structure would be sulfur filled in carbon nanotubes (CNT), with open rings only permeable to Li-ions. Reactive molecular dynamics (MD) simulations showed that the DFT determined optimum open ring size could be achieved by controlling the CNT oxidation.

Highly concentrated electrolytes can achieve the partially solvated Li-PS, and expand the electrochemical stability window by forming SEI. To solve the high viscosity issue, co-solvent was designed by adding low viscosity and electronically stable dichloromethane (DCM) to highly-concentrated LiTFSI in ethyl acetate (EA). The concentration of the DCM was designed to obtain a unique solvation structure, where clusters of partially solvated Li^+ , TFSI $^-$, and EA network were surrounded by the DCM so that the former inherited the expanded electrochemical window and the latter accelerated the Li transport.

Overall, this thesis demonstrated that atomic electrode-electrolyte interface structure, interaction, and properties can be directly connected to the cell-level discharge performance, thus modeling these connections provided an integrated approach for battery materials design.

ACKNOWLEDGMENTS

First of all, I would like to thank my advisor Prof. Yue Qi for her guidance and help. She has provided constructive guidance, which trained me to become an independent researcher. Without her constant encouragements, I would not be able to complete my research journey. Her integrity, enthusiasm, and companionship set an excellent example for me to follow, which will enlighten and guide my life. I also want to appreciate my committee member, Prof. Wei Lai, Prof. Scott Barton, and Prof. Hui-Chia Yu for their helpful directions and suggestions on my researches. Additionally, special thanks to our partners, Prof. Chunsheng Wang, and Prof. John Cumings, Prof. Yongyao Xia, Dr. Mei Cai and Dr. Yang Li for their helpful discussion and contributions.

I also want to acknowledge all my colleagues and friends in Michigan State University: Christine James, Tridip Das, Kwangjin Kim, Jialin Liu, Hong-Kang Tian, Thanaphong Phongprecha, Yunsong Li, Michael Swift, and Chi-ta Yang. They shared their expertise with me and support my research. It has been a pleasure to know you and share my life in graduate school.

Most importantly, I want to appreciate my family for their unconditional love and encouragements. Their trust and love made me a strong and confident person, which allowed me to complete this work.

Finally, I would like to acknowledge the support from Nanostructures for Electrical Energy Storage (NEES), an Energy Frontier Research Center funded by the U.S. Department of Energy, Office of Science, Basic Energy Sciences under Award number DESC0001160; an General Motors internship; and the National Science Foundation through grant number DMR-1832808 for the collaborative GOALI research with General Motors.

TABLE OF CONTENTS

LIST OF TABLES..... viii

LIST OF FIGURESix

1 Introduction and problems identification..... 1

1.1 Batteries and interfaces	1
1.1.1 Li-ion batteries and Li-S batteries.....	1
1.1.2 Unique interfacial challenges in Li-S battery	6
1.2 Current understanding of SEI on the anode	10
1.3 Current understanding of solvation status of Li-PS.....	14
1.3.1 The influence of Li-PS solvation on the open circuit voltage (OCV)	14
1.3.2 Influence of micrometer level pore structure on the energy density.....	17
1.3.3 Influence of nanopores and sub-nanopores on the mitigation of Li-PS shuttle problem	19
1.4 Highly concentrated electrolytes.....	21
1.4.1 Forming SEI in highly concentrated electrolytes.....	21
1.4.2 Co-solvent in the concentrated electrolyte at low temperatures	23
1.5 Integrated computational approach.....	25

2 Connecting irreversible capacity loss with electrical insulating properties of SEI components.....28

2.1 Summary	28
2.2 Introduction.....	28
2.3 Model details.....	31
2.3.1 DFT computed electron tunneling barrier and its relation with capacity loss	31
2.3.2 Loading conditions estimated by stress-strain relationship	34
2.4 Results and discussion	35
2.4.1 Work function and band gap	35
2.4.2 Capacity loss	38
2.4.3 Tunneling barrier change due to stress on SEI.....	42
2.5 Conclusions.....	45

3 Predicting open circuit voltage curves in Li-S battery depending on the solvation of Li-polysulfides46

3.1 Summary	46
3.2 Introduction.....	46
3.3 Model details.....	50
3.3.1 OCV and formation energy calculations.....	50
3.3.2 Solvation energy calculations	52
3.4 Results.....	55
3.4.1 Temperature effect in crystalline phases	55
3.4.2 Temperature effect for non-solvated Li_2S_4	55
3.4.3 Temperature and solvation effect for fully solvated Li_2S_4	59
3.4.4 Predicted OCV curve	63
3.5 Conclusions.....	63

4 S-C cathode design micrometer level pores: achieving high energy density by changing the porosity	65
4.1 Summary	65
4.2 Introduction.....	65
4.3 Summary of the experimental results	67
4.4 Calculation of diffusion distance of Li-PS.....	69
4.4.1 Calculation details.....	69
4.4.2 Calculated diffusion distance	70
4.5 Analytical model	72
4.5.1 Determination of the limiting factor for the capacity in the first plateau	73
4.5.2 Depression of the second plateau.....	75
4.5.3 The volumetric and gravimetric energy density	78
4.6 Conclusion	80
APPENDIX.....	81
5 S-C cathode design with nanopores: synergetic effect between pore size and electrolyte concentration	83
5.1 Summary	83
5.2 Introduction.....	83
5.3 Model details.....	85
5.4 Computational results	86
5.4.1 Partially solvated Li_2S_4 and the transition from the two-plateaued OCV to the one-plateaued OCV.....	86
5.4.2 Design of S-C cathode through the synergetic effect of pore size and salt concentration on the OCVs.....	89
5.5 Conclusion	95
APPENDIX.....	96
6 S-C cathode design with sub-nanopores: optimum pore size to prevent Li-PS formation	98
6.1 Summary.....	98
6.2 Introduction.....	99
6.3 Model details.....	102
6.4 Computational results	104
6.4.1 DFT calculation of Li transport barrier and the minimum open-ring size....	104
6.4.2 Comparison of molecular sizes and the maximum open-ring sizes.....	108
6.4.3 Stable ring size achieved by oxidation of CNT simulated by ReaxFF MD..	109
6.5 Conclusion	113
7 Improvement of Li transport property of concentrated low-temperature electrolyte by adding co-solvent.....	114
7.1 Summary	114
7.2 Introduction.....	114
7.3 Summary of experimental results	117
7.4 Model details.....	120
7.4.1 DFT calculation	120
7.4.2 MD simulation	121
7.5 Results.....	123
7.5.1 Li binding energy	123

7.5.2 Solvation structure	123
7.5.3 Diffusion coefficient	125
7.5.4 HOMO and LUMO levels	128
7.6 Conclusion	129
8 Conclusion and future research.....	131
BIBLIOGRAPHY	133

LIST OF TABLES

Table 2.1 Calculated results of the tunneling effect in different SEI components. ρ was the number of lithium ions per unit volume in SEI component, Φ , represented the work function, E_g was the band gap (computed from GGA and HSE06), which led to different electronic tunneling barrier, ΔE_t , the critical thickness of SEI, d^* , and the specific capacity loss, C	39
Table 3.1 List of free energy terms for all species (Unit: eV). E_{DFT} is calculated with basis set DFT in Dmol3. E_{vib} , S_{vib} , E_{rot} , S_{rot} , E_{tra} , S_{tra} are obtained through vibrational analysis. For the solvation model in the method part, E, Cl, I and Cm stands for explicit model, cluster model, implicit model, and combined model, respectively. For the calculation method, D stands for calculations with Dmol3 and V stands for calculations with VASP.....	57
Table 3.2 E_{solv} for the fully solvated Li_2S_4 in DOL solvent calculated by different solvation models (Unit: eV). The fluctuations are due to different configurations in the sampling scheme.	61
Table 4.1 List of composition, density, PS concentration and diffusion coefficient of DME and Li_2S_4 in each solution.....	71
Table 4.1A List of all parameters used for the analytical model.	82
Table 5.1 List of free energy terms for partially solvated Li_2S_4 (Unit: eV). EDFT is calculated with basis set DFT in Dmol3. E_{vib} , S_{vib} , E_{rot} , S_{rot} , E_{tra} , S_{tra} are obtained through vibrational analysis. For the solvation model in the method part, E and Cl, stand for explicit model and cluster model, respectively. For the calculation method, D stands for calculations with Dmol3 and V stands for calculations with VASP.	91
Table 6.1 Largest ring size created in each simulation case	112
Table 7.1 Physical properties of various electrolytes with different compositions. (In courtesy of Xiaoli Dong and Yongyao Xia from Fudan University.).....	118
Table 7.2 Calculated properties and Li^+ diffusion coefficient in the electrolytes, compared with commonly used ethylene carbonate (EC) solvent. A cutoff distance of 2.5 Å was used for CN of Li-O, and a cutoff distance of 4.5 Å was used for CN of Li-N.	122
Table 7.3 Summary of binding energy for Li^+ with different species.....	123
Table 7.4 Calculated LUMO and HOMO levels for different species in the electrolytes.	129

LIST OF FIGURES

Figure 1.1 Schematics of the charging and discharging mechanism in Li-ion battery[7]. (Copyright from Materials Today 2016).....	2
Figure 1.2 Schematics of the function [13] (a) and structure [14] (b) of SEI on the anode. (Copyright from Journal of the Electrochemical Society 2012 and 2004).....	4
Figure 1.3 Volumetric and gravimetric energy densities of different battery systems [15]. (Copyright from Advanced Energy Materials 2015).....	5
Figure 1.4 Schematic of Li-PS shuttle in Li-S battery [22]. (Copyright from Journal of Power Sources 2014).....	7
Figure 1.5 Schematic of the contribution of the various component in DOL electrolyte to the SEI on the anode in Li-S battery [41]. (Copyright from Journal of the Electrochemical Society 2009).....	11
Figure 1.6 One-dimension rectangular barrier model for electron tunneling through the SEI layer [51]. (Copyright from Journal of the Electrochemical Society 2015).....	13
Figure 1.7 Two-plateaued (a) and one-plateaued (b) discharging OCV curves observed in Li-S batteries summarized by Markevich <i>et al.</i> [79]. (Copyright from Journal of The Electrochemical Society 2017).....	16
Figure 1.8 (a) Convex hull of Li-S systems from DFT calculation by Yang <i>et al.</i> [84]. (b) Predicted OCV curve from DFT calculation with solvation and temperature effect included by L. Wang <i>et al.</i> [85]. (Copyright from Journal of Materials Chemistry A 2015 and Journal of Energy Chemistry 2013.).....	17
Figure 1.9 (a) Discharging curves of Li-S batteries with different carbon matrix observed by Zhang <i>et al.</i> [90] with relatively large pore volume. (Copyright from Journal of the Electrochemical Society 2013) (b) Discharging curves of Li-S batteries observed by further decreasing pore volume.	19
Figure 1.10 Illustration of expanded electrochemical stability window for water-in-salt electrolytes together with the modulated redox couples of LiMn ₂ O ₄ cathode and Mo ₆ S ₈ anode caused by high salt concentration [104]. (Copyright from Science 2015).....	23
Figure 2.1 Calculation of electron tunneling barrier (ΔE_t) by aligning the Fermi level (ϵ_f), work function (Φ) and band gap (E_g) of the lithium anode and SEI.....	33
Figure 2.2 Work function of Li ₂ CO ₃ , Li ₃ PO ₄ , LiF, and Li as a function of slab thickness.	35
Figure 2.3 Relaxed atomic structure of Li ₂ CO ₃ (001) slab model with increasing slab thickness.	37
Figure 2.4 Predicted initial irreversible capacity loss due to SEI component formation assuming	

the electrons are completely blocked at a tunneling barrier T of e^{-40} (a), e^{-30} (b), and e^{-20} (c). The original experimental data points and linear fitting from Joho were also added for comparison [60]......40

Figure 2.5 Schematic of the four loading methods (a), band gap and work function value as a function of σ/E (b) and η (c).42

Figure 3.1 The structures and formation energies of non-solvated Li_2S_4 . The optimized structure of (a) Li_2S_4 monomer and (b) $(\text{Li}_2\text{S}_4)_8$ cluster. Li and S atom are represented by purple and yellow, respectively. The distance of S-S and S-Li bonds are labeled for Li_2S_4 . (c) The calculated Gibbs free energy of Li_2S_4 as a function of cluster size n . The data points represent different configurations. (d) The predicted relative formation energy of non-solvated Li_2S_4 with respect to the crystalline S and Li_2S58

Figure 3.2 The solvation structure and energy for fully solvated Li_2S_4 monomer. Cumulative CN as a function of cutoff radius (a) and optimized geometry (b) of $\text{Li}_2\text{S}_4 \cdot 4\text{DOL}$ solvation shell with the dielectric continuum. The difference between the optimized geometry with and without dielectric continuum can be neglect. The Li, S, C, O, and H are represented as purple, yellow, grey, red and white, respectively. The distance of Li-S and Li-O are labeled. Cumulative CN as a function of cutoff radius (c) and optimized geometry (d) of $\text{Li}_2\text{S}_4 \cdot 20\text{DOL}$ after 0.5 ps ab initio NVT simulation. The relative formation energy of Li_2S_4 monomer under fully solvation status at 0 K and 300 K compared with crystalline S and Li_2S (e). The solvation energy is calculated with the implicit, cluster, combined and explicit models, which is labeled as (I), (Cl), (Cm) and (E). The energy of crystalline S and Li_2S are already shifted to 0 for easy comparison. The error bar indicates the results from the different initial configuration.61

Figure 3.3 The calculated (a) relative formation energies and (b) the corresponding OCVs for non-solvated Li_2S_4 at 300K. The energy of crystalline S and Li_2S are already shifted to 0 for easy comparison in (a).63

Figure 4.1 SEM images of the sulfur electrode with a porosity of 70% (a), 60% (b), and 50% (c). (In courtesy of Ning Kang, Li Yang and Mei Cai from General Motors.)67

Figure 4.2 Charge-discharge profile (a) and cycling performance (b) of Li-S cells with sulfur loading of 5 mg/cm² under different porosity. (In courtesy of Ning Kang, Li Yang and Mei Cai from General Motors.)69

Figure 4.3 Simulated average mean squared displacement (MSD) of Li_2S_4 (a) and DME (b) as a function of simulation time in each solution. A typical snapshot of solution 2.1m (c) and saturated 8.7 m (d) solution. Estimated self-diffusion distance of Li_2S_4 as a function of C-rate in each solution (e).72

Figure 4.4 Predicted PS concentration and S utilization as a function of porosity (a). Predicted total surface area and effective surface area as a function of porosity (b). Predicted discharging curves at different porosity (c).78

Figure 4.5 The predicted gravimetric energy density based on the mass of S and volumetric energy density based on the volume of cathode materials. The schematics showing the difference between low porosity and high porosity were also inserted. The unutilized S, carbon matrix and deposited $\text{Li}_2\text{S}_2/\text{Li}_2\text{S}$ layer were represented as yellow, black and red, respectively.

.....	80
Figure 5.1 Structures of the partially solvated Li_2S_4 . (a) The liquid structure of $10\text{Li}_2\text{S}_4 \cdot 20\text{DOL}$ and (b) its cumulative CN as a function of cutoff radius. (c) The optimized $\text{Li}_2\text{S}_4 \cdot 2\text{DOL}$ partial solvation shell and (d) its cumulative CN as a function of cutoff radius. Li, C, S, H and O atoms were represented as purple, grey, yellow, white and red, respectively.	88
Figure 5.2 The calculated (a) relative formation energies and (b) the corresponding OCVs for Li_2S_4 in different solvation status at 300K. The energy of crystalline S and Li_2S are already shifted to 0 for easy comparison in (a).....	92
Figure 5.3 Cyclic voltammograms and galvanostatic discharging curve of Li-S batteries: galvanostat discharging curves (a) and CV (b) in 1M LiTFSI/(DME+DOL) electrolyte paired with cathodes with different carbon matrix pore sizes (labeled in parenthesis), S@CMK3, S@CMK8, and S@CMS, respectively. (b) Galvanostat discharging curves (c) and CV (d) of S@CMK3 cathode in LiTFSI/(DME+DOL) electrolyte at concentrations of 1M, 3M, 6M and 9M. (c) galvanostat discharging curves (e) and CV (f) of S@CMS cathode in LiTFSI/(DME+DOL) electrolyte at concentrations of 1M, 3M and 6M. The cyclic voltammograms were tested with a sweep rate of 0.1 mV/s at the 5th cycle. The galvanostatic discharging curves were tested at a 0.1 C rate at the 10th cycle. (In courtesy of Jing Zheng and Chunsheng Wang from University of Maryland.)	94
Figure 5.1A Cyclic voltammograms of Li-S batteries at a sweep rate of 0.1 mV/s from 1 st to 5 th cycle: CV in 1M LiTFSI/(DME+DOL) electrolyte of S@CMK3 (a), S@CMK8 (b) and S@CMS (c) cathode, CV of S@CMS cathode in 3m (d) and 6m (e) LiTFSI/(DME+DOL) electrolyte, and CV of S@CMK3 cathode in 3m (f) and 6m (g) and 9m (h) LiTFSI/(DME+DOL) electrolyte. The pore size of the carbon matrix is also labeled in the parenthesis. (In courtesy of Jing Zheng and Chunsheng Wang from University of Maryland.).....	97
Figure 6.1 Schematic of the synthesis process of CNT-encapsulate-S Cathode.....	102
Figure 6.2 (a) Simulation cell used for the DFT calculation of E_b . (b) The configuration of rings with different size. The E_b , the ring size, and the two diameters were also labeled. Li, edge C atoms with fixed coordination, and other C atoms allowed to relax were represented as purple, blue and grey.	104
Figure 6.3 The calculated total energy of the configuration and the Bader charge on Li as a function of d for the 14r ring (a) and 18rA ring (b). Binomial trendlines were used to fit the data points.	106
Figure 6.4 E_b summarized as a function of the mean diameter of the open ring.	107
Figure 6.5 Comparison of molecular size of Li-ion, Li atom, S_2 , Li_2S_4 , DME and DOL with 18rA ring. The Li, S, C, H, and O are represented as purple, yellow, grey, white and red, respectively.	109
Figure 6.6 The oxidation process of CNT with O:C ratio 1:3 at 1000K. The C, O, and H were represented as grey, red and white, respectively.	110
Figure 7.1 Raman spectra (a) in all electrolytes, pure EA and DCM solvents and LiTFSI crystal.	

Linear scan voltammetry (LSV) of 1m and 5m EA-based electrolytes (b), 5m-1-4 cosolvent electrolytes (c). The LSVs were measured with a three-electrode system in which Pt plate, Pt plate and Li metal were used as working, counter and reference electrodes, respectively. The scan rate was set as 0.5 mV/s. Charge-discharge at +25 °C and -70 °C (d), Rate and cycle performance at the ultra-low temperature of -70 °C (e), Ragone plots at +25 °C and -70 °C (f), of the Li-PTPAn battery. ((Copy right from Angewandte Chemie International Edition 2019.) 120

Figure 7.2 The snapshot (a) of MD simulation, and coordination number (CN) (b) as a function of cutoff distance for 0.15m EA-based electrolyte. The snapshot (c) of MD simulation, and CN (d) as a function of cutoff distance for 5m EA-based electrolyte. The snapshot (e) of MD simulation, and CN (f) as a function of cutoff distance for the 5m-1-4 co-solvent electrolyte. 127

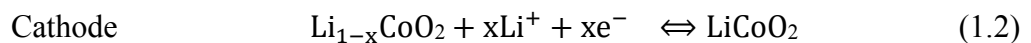
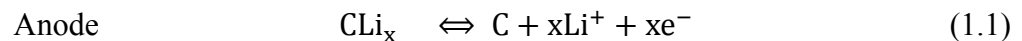
Figure 7.3 Coordinated numbers of EA molecules and TFSI⁻ anions around Li⁺, and mole fraction of free EA molecules in different electrolytes and LiTFSI crystal (a). The Li⁺ cation mean-squared displacements (MSD) in various electrolytes at +25 °C (b) and -70 °C (c). .. 128

1 Introduction and problems identification

1.1 Batteries and interfaces

1.1.1 Li-ion batteries and Li-S batteries

Conventional rechargeable lithium-ion (Li-ion) batteries consist of four main components: the positive electrode, the negative electrode, the separator, and the electrolyte, in addition to the current collectors. For commercial Li-ion batteries, the positive electrode materials are usually transition metal oxides containing Li, such as LiMn_2O_4 , LiCoO_2 , LiFePO_4 , LiNiO_2 and their derivatives [1][2]. The most commonly used negative electrode materials are graphite and other carbon (C) materials [3]. Alternative negative electrode materials including Sn, Si and Li metal are also promising due to their high theoretical capacity. The separator, sandwiched between the positive and negative electrode, is a porous thin film of polyethylene or polypropylene. The porous structure enables the transport of electrolyte, while its blocking nature isolates the cathode and anode by blocking electrons. The electrolyte is a solution with Li salt dissolved in a liquid solvent. The salt includes LiPF_6 , LiClO_4 , $\text{LiB}(\text{C}_2\text{O}_4)_2$, LiBF_4 , lithium bis(fluorosulfonyl)imide (LiFSI) and lithium bis(trifluoromethanesulfonyl)imide (LiTFSI). Carbonated based organic solvents are widely used in commercialized Li-ion batteries, including ethylene carbonate (EC), propylene carbonate (PC), diethyl carbonate (DEC) and dimethyl carbonate (DMC)[4][5]. Aqueous electrolyte with water as the solvent is also under research due to its safety and cleanliness [6].



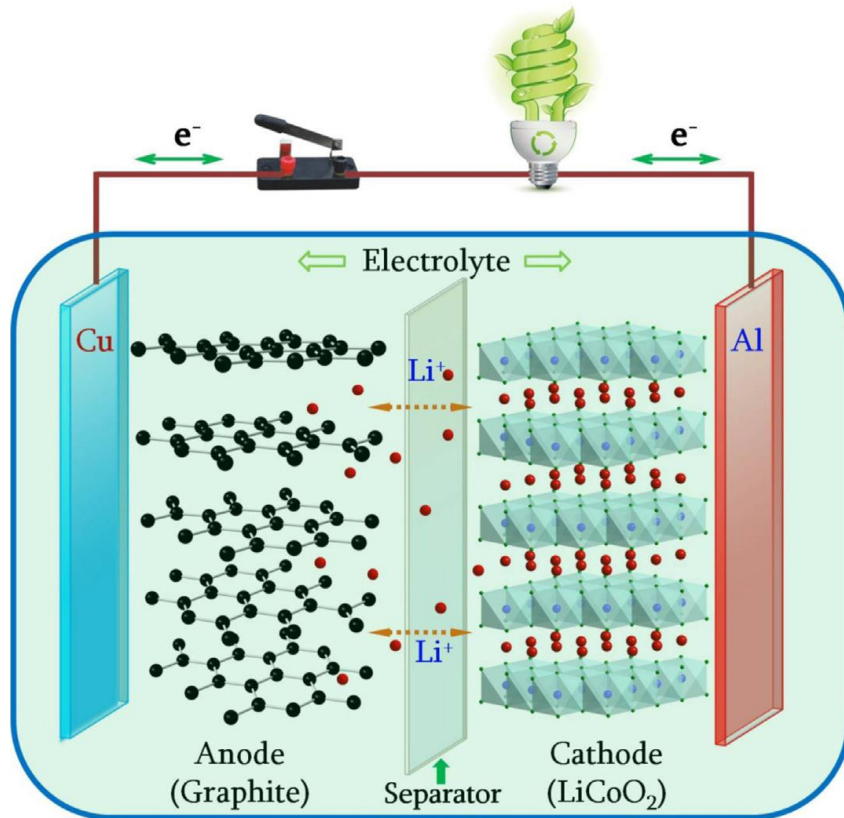


Figure 1.1 Schematics of the charging and discharging mechanism in Li-ion battery[7]. (Copyright from Materials Today 2016)

The working mechanism of Li-ion batteries is related to the redox reactions at both electrodes. Generally, the definitions of cathode and anode are based on the discharging reaction, in which the positive electrode serves as the cathode and the negative electrode serves as the anode. Taking LiCoO_2 cathode and graphite anode as an example, schematics of the charging and discharging mechanism is shown in Figure 1.1. The half reactions occurring on the anode, cathode, and the overall electrochemical reactions are listed in Equation (1.1~1.3), respectively[2][8]. During discharging, on the anode side, Li-ions and electrons are generated when Li_xC are oxidized into LiC , as shown in Equation (1.1). These Li-ions then transport from the anode to the cathode electrode spontaneously due to the difference in electrochemical potential. At the cathode, the Li ions and electrons are consumed in the reduction reaction from $\text{Li}_{1-x}\text{CoO}_2$ to LiCoO_2 , as shown in Equation (1.2). Thus, the energy is provided to the external load when LiCoO_2 and graphite are generated from the overall reaction between Li_xC and

$\text{Li}_{1-x}\text{CoO}_2$, as shown in Equation (1.3). Vice versa in the charging process, Li-ions and electrons are generated when LiCoO_2 is oxidized to $\text{Li}_{1-x}\text{CoO}_2$, and consumed when C is reduced to CLi_x . Thus, energy from external power source is stored in the battery.

Another unique and important component in Li-ion battery is the SEI, which is a thin layer found at the electrode/electrolyte interface. The SEI was formed by the decomposed products of the electrolyte [9] because the working voltage of most electrodes is outside of the redox voltage range of the electrolyte [10]. As shown in Figure 1.2a, this SEI prevents further decomposition of the electrolyte by blocking electrons but allowed the transport of the Li ions. It is also desired that the SEI should also protect the electrode by accommodating its deformation during cycling and preventing other side reactions between electrode and electrolyte. SEIs can be formed on the surface of both the cathode and anode, but SEI on the cathode is generally much thinner than that on the anode [11]. Thus, the SEI on the anode has more influence on the performance of the battery. On the carbon anode in a typical commercial Li-ion battery, a thin and stable SEI forms during the first cycle by consuming 10~20 % initial capacity. This is beneficial to inhibit the capacity fading and improve cycling stability in the following cycles. Figure 1.2b shows the generally accepted structure of the SEI, which consists of two layers: the inside inorganic layer with Li_2CO_3 , LiF and Li_2O ; and outside organic layer with $(\text{CH}_2\text{OCO}_2\text{Li})_2$ and ROLi (R stands for organic groups). The exact composition of SEI is related to many factors, such as the redox potential and pathways of electrolyte solvent, Li salt, and additives[12]. The materials properties of SEI, such as the mechanical property, Li transport property, and electrical insulating property are important as they are directly related to the functionality of SEI. However, they are still not fully known due to the experimental challenges associated with the complexity, chemical sensitivity and nano-meter thickness of the SEI layers [12].

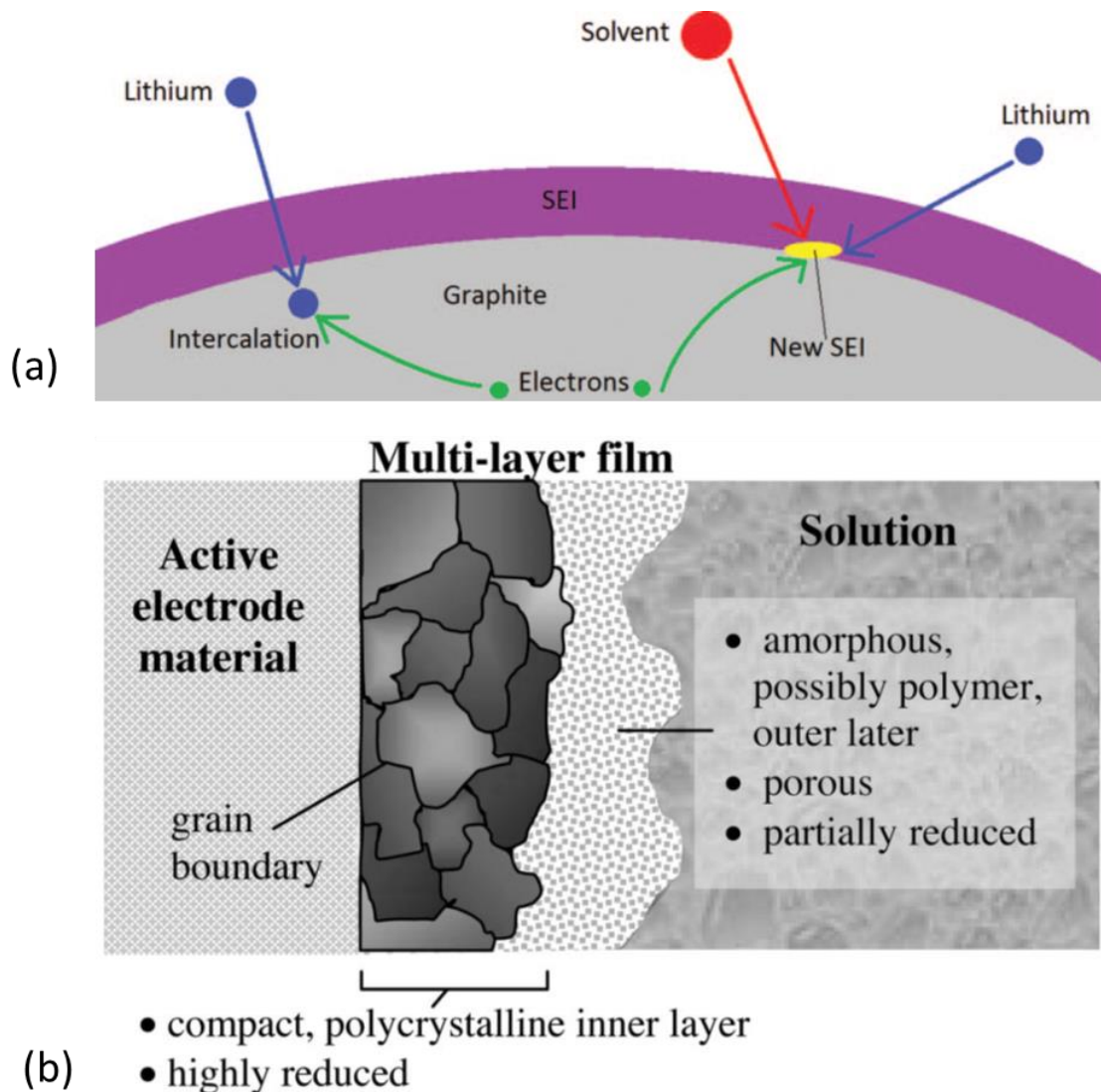


Figure 1.2 Schematics of the function [13] (a) and structure [14] (b) of SEI on the anode. (Copyright from Journal of the Electrochemical Society 2012 and 2004)

The capacity, gravimetric and volumetric energy density of Li-ion batteries are limited by the cathode and anode materials. The practical capacity of most cathode materials including LiMn_2O_4 , LiCoO_2 , LiFePO_4 , LiNiO_2 are less than 200 mAh/g, and the practical capacity of most carbon anode materials are between 300~372 mAh/g [16]. Based on this, the gravimetric and volumetric energy densities of Li-ion batteries are around 250~650 Wh/L and 120~250 Wh/kg, respectively, as shown in the plot summarized by Hagen *et al.* [15] in Figure 1.3. Even though these values can meet the requirement of most portable energy devices, including smartphones and laptops, a higher energy density is required for larger applications, such as

electric vehicles. For higher energy density and lower cost, Li-Sulfur (Li-S) batteries are quite promising. By replacing the cathode and anode materials with elemental sulfur (S) and metallic Li, the reactions become:

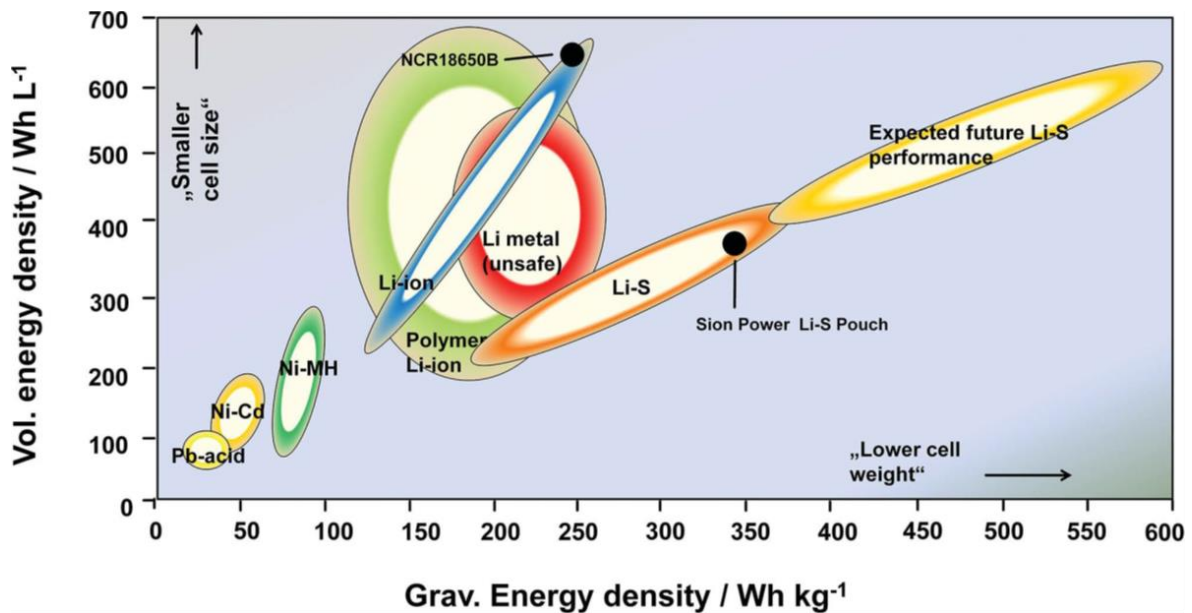
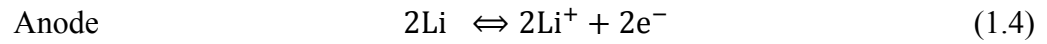


Figure 1.3 Volumetric and gravimetric energy densities of different battery systems [15]. (Copyright from Advanced Energy Materials 2015)

The configuration of a typical Li-S battery is as follows: composite cathode with elemental S embedded in carbon matrix (C-S cathode), Li metal anode, and ether-based electrolyte. The use of carbon in the S-C composite cathode is to compensate the electronic insulating nature of S and buffer the volume expansion of S upon lithiation. For Li-S batteries, the ether-based electrolyte such as dimethoxyethane (DME) and dioxolane (DOL) is typically used since its low reduction potential is more suited for Li metal anode comparing with carbonate-based

electrolyte [19]. The Li-anode not only provides high capacity and lower voltage (as an anode) but also provides the source of Li-ion for the S-cathode.

Although the Li-S batteries promise a higher gravimetric energy density, lower cost, and more environmentally friendly than the conventional Li-ion batteries, many challenges (to be discussed in the next section) still hinder its commercialization.

1.1.2 Unique interfacial challenges in Li-S battery

Li-S batteries still face many unique challenges regarding rapid capacity and energy fading. Fundamentally, all the Li-metal anode and elemental S cathode can participate in a redox reaction (1.4~1.6). This is quite different from the intercalation materials used in the conventional Li-ion batteries that shown in equation (1.1~1.3) when only Li-ions and electrons transport in the host materials through the intercalation reaction. The repeated stripping and plating of Li will result in large deformation and morphological changes, such as dead Li, dendrite growth, and repeated forming and cracking of SEI [20]. These phenomenon are responsible for the low columbic efficiency and rapid capacity fading during cycling, which highly affects the cycling stability. Secondly, considering that both the S and Li_2S are electronic insulators, it is necessary to add conductive materials (such as the carbon matrix) into the cathode. The repeated the stripping of elemental S and the plating of $\text{Li}_2\text{S}_2/\text{Li}_2\text{S}$ also result in an 80 % volume expansion from elemental S to the Li_2S . This requires extra pore volume in the carbon matrix to accommodate the volume expansion. Furthermore, the solvation of the Li-PSs, such as Li_2S_8 , Li_2S_6 , Li_2S_4 requires a proper amount of electrolyte. The introduce of porous carbon matrix and the electrolyte will decrease both the volumetrical and gravimetric energy density in practical use. Thirdly, the long-chain Li-PSs (Li_2S_8 , Li_2S_6 , Li_2S_4) can diffuse between from the cathode to the anode, and precipitate as the blocking and insoluble Li_2S_2 and Li_2S layer on both anode and cathode surfaces, as shown in Figure 1.4. This “Li-PS shuttle problem” causes severe degradations of the battery, such as loss of active S, blocking of electronic

pathways, low coulombic efficiency and rapid capacity fading during battery cycling, leading to poor cycling stability [21]. All these problems hinder the commercial applications of Li-S batteries. To improve the energy density and prevent the capacity fading, an integrated design at the electrode-electrolyte interface is important.

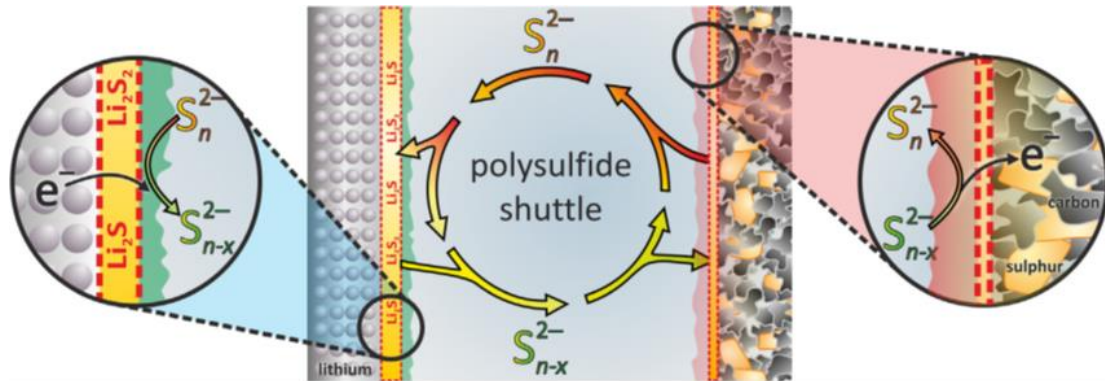


Figure 1.4 Schematic of Li-PS shuttle in Li-S battery [22]. (Copyright from Journal of Power Sources 2014)

On the anode-electrolyte interface, the SEI at the electrode-electrolyte interface can be designed to accommodate the lithium morphology change and avoid capacity fading with Li metal anode. As summarized by Wang *et al.* [23], many experiments showed that increasing the amount of LiF in SEI, a more electronically insulating component would slow down the capacity fading in electrode with large deformation, such as Li-metal and Si-anode [23–29]. To increase the LiF content, electrolyte either with high LiSFI or LiTFSI salt concentration [28,30], or fluorinated electrolyte additive [24,27,29], such as fluorinated ethylene carbonate (FEC), can be used. Q. Zhang *et al.* [31] had co-deposited Li_2CO_3 and LiF as artificial SEI layer on very thin Si film anode, and demonstrated that a higher ionic carrier concentration in the interface between Li_2CO_3 and LiF significantly improved lithium ion transport and reduced electron leakage. However, since the typical inorganic components in SEI cannot sustain large deformation with the thicker anode, polymer coatings [32–34] with large elastic range and high binding ability had been proposed as a protective coating layer. Li *et al.* [32] demonstrated that

lithium polyacrylic acid (Li-PAA) coating can reduce the side reactions and improve the cycling stability. Lopez *et al.* [34] further compared a series of polymer coating materials and their effectiveness in suppressing the large deformation of Li anode. It was suggested that besides the elastic range and binding ability, the chemical stability, modulus, flowability, and uniformity should also be considered in the design of polymer coating. Furthermore, when designing the electrolytes and their corresponding SEI (both naturally formed and artificial), the exact composition should be designed according to the property of the individual component. As a summary from the above statement, these properties included the Li-transport property, the mechanical property, and electrical insulating property. Therefore, quantifying the property of SEI components is highly important, but is still missing.

The cathode-electrolyte interfaces also include the poly-sulfide interaction with the electrolyte and these interfaces are important for an optimum energy density and mitigation of “Li-PS shuttle problem” in Li-S batteries. Considering a typical configuration when elemental S is embedded in the porous structure in a carbon matrix, interfaces can be formed among multiple species, including the electrolyte solvent, the elemental S, the porous carbon matrix, the mid-product Li-PSs, and the final product Li_2S , such as Li-PS-electrolyte, S-carbon interface, Li_2S -Carbon, etc. Specifically, the Li-PS-electrolyte interface also determines whether the Li-PSs is fully solvated, partially solvated or not dissolved, which is referred to as the “solvation status” in this thesis. The solvation status will subject to change with the amount of electrolyte and the pore size and volume of the carbon matrix. Both the evolution of the solvation status of Li-PS and the carbon pore structure can impact the energy density of the Li-S battery. A certain amount of electrolyte, filled in the S-C electrode porosity, is needed to dissolve the Li-PSs, however too much of solvents will only add unnecessary weight and volume to the battery, thus decreasing the energy density. Thus, the design of pore size and volume, in the carbon matrix with the corresponding solvation status of Li-PS is directly related

to the optimum energy of Li-S battery. Furthermore, the solvation status of Li-PS in the electrolyte is related to the “Li-PS shuttle problem”. The solvation status can be changed by either the concentration of the electrolyte [35] or by using extremely small nano-sized carbon matrix pores (ex: 0.5 nm) [36], as both have been demonstrated to mitigate Li-PS shuttle problem and increase cycling stability experimentally. Thus, understanding the relationship between the solvation status of Li-PS and the energy density of Li-S batteries is important. With this understanding, integrated design strategy for the S-C structure and electrolyte can be proposed to achieve the ideal solvation status.

The main focus of this thesis is to connect the understanding of the electrode-electrolyte interfacial mechanisms with the capacity loss and energy density of Li-S batteries, in order to provide integrated design approaches for Li-S batteries. More specifically, this thesis will investigate the SEI on the anode as an integrated component for the anode/SEI/electrolyte interface, and provide guidance to design the SEI according to the component-property relationship. On the cathode side, this thesis will reveal the relationship between the solvation status of Li-PS with the energy density and the discharging performance of Li-S battery. Furthermore, this thesis will seek the C-S porosity design at different length scales and the electrolyte concentration to alter the solvation status in order to mitigate the Li-PS shuttle problem. The rest of this introduction is arranged as follows. In section 1.2, we will review the current studies of the SEI on the anode and identify the remaining knowledge gap for the SEI properties: how the electrical insulating property of SEI components is connected to the irreversible capacity loss. In section 1.3, we will review the current studies related to the solvation of Li-PS, and identify a knowledge gap: why the energy density and the discharge voltage curves of Li-S batteries can be influenced by the solvation status of Li-PS. In section 1.4, we will further review the current understanding of the emerging highly-concentrated electrolyte, and identify a remaining gap: how to change the unique solvation structure to

improve the Li-transport property. Then, in section 1.5, the computational approach to address key questions in the identified knowledge gaps will be introduced.

1.2 Current understanding of SEI on the anode

Investigation of the components of SEI formed on the Li anode in Li-S battery is the first step to understand the SEI. EC will naturally reduce on the Li surface and form SEI following either one-electron[37] or two-electron pathway [38]. The main products include organic solids such as $(\text{CH}_2\text{CH}_2\text{OCO}_2\text{Li})_2$, $(\text{CH}_2\text{OCO}_2\text{Li})_2$, $\text{LiO}(\text{CH}_2)_2\text{CO}_2(\text{CH}_2)_2\text{OCO}_2\text{Li}$, $\text{Li}(\text{CH}_2)_2\text{OCO}_2\text{Li}$, and inorganic solids such as Li_2CO_3 , and gas such as CO and CH_4 . Li salt containing F is usually coupled with carbonate-based electrolyte solvent, whose reduction was suggested to be responsible for the LiF component in SEI [39,40]. For ether-based electrolyte such as DOL, Aurbach *et al.* [41] investigated the reduction product in an electrolyte containing LiTFSI, Li-PS, LiNO_3 , and DOL solvent. Using Fourier transform infrared and X-ray photoelectron spectroscopies, the contribution of each species to the SEI is represented in Figure 1.5. The SEI components mainly consist of inorganic species, such as LiF, Li_2S , Li_2S_2 , Li_xSO_y and Li_xNO_y and organic species such as LiOR and RCOOLi. Xiong *et al.* also found that the interaction between Li-PSs and LiNO_3 helped to generate more inorganic species of Li_xNO_y in the SEI [42]. Since there are common components in the SEI from both carbonate-based and ether-based electrolyte, investigation of the materials property of the SEI with both carbonate-based and ether-based electrolyte provide valuable information for that on the design of SEI on Li metal anode in Li-S batteries. These properties include the mechanical property, the Li transport property, and electrical insulating property because they are directly related to the functionality of SEI. By knowing the properties and the contribution from each component, a rational design of electrolyte and its resulted SEI can be achieved.

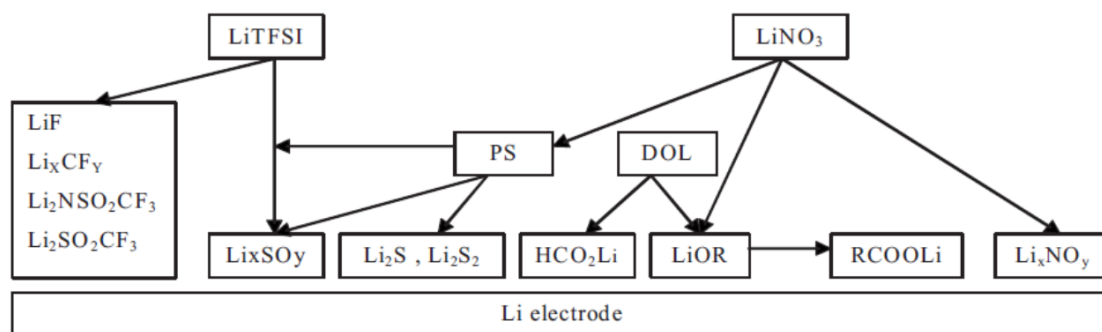


Figure 1.5 Schematic of the contribution of the various component in DOL electrolyte to the SEI on the anode in Li-S battery [41]. (Copyright from Journal of the Electrochemical Society 2009)

The mechanical and Li-ion transport properties for individual SEI component had been investigated and ranked by simulations. For the mechanical property, Shin [43] ranked the stiffness in the order of $\text{LiF} > \text{Li}_2\text{CO}_3 > (\text{CH}_2\text{OCO}_2\text{Li})_2 > \text{LiOCO}_2\text{CH}_3 > \text{polyethylene oxide}$ by calculating Young's modulus. It was also showed that the $\text{Li}_2\text{CO}_3/\text{Li}$ interface bore higher adhesion property than LiF/Li interface [44]. For Li transport property, Shi *et al.* determined the dominant carrier was Li-ion interstitials in Li_2CO_3 on the anode surface [45]. Jie *et al.* determined the dominant carrier was the Schottky pairs (Li-ion and F-ion vacancies) in LiF on the anode surface [46]. Recently, a space charging effect causing the accumulation of Li-ion carriers (Li-ion interstitials in Li_2CO_3) but the depletion of electronic carriers near the $\text{LiF}/\text{Li}_2\text{CO}_3$ interface was also predicted in computation [47] and confirmed in the experiment [48]. Understanding these properties provided new insights for the rational design of electrolyte and its resulted SEI.

However, the relationship between the electrical insulating property of SEI components and the irreversible capacity loss has not been clarified until our publication [49]. The electronic conductivity of SEI is less studied and the contribution from each component was unclear. The concept of electron tunneling model was first put forward by Peled, assuming that an SEI layer on an electrode needs to be thick enough to block electron tunneling [50]. In the

1-D analytical model by Li *et al.* [51], the SEI was modeled as a uniform tunneling barrier with a thickness $\sim 3\text{nm}$ to block the electrons, as shown in Figure 1.6. The tunneling barrier was estimated to be in the range of $2.8\sim 2.9\text{eV}$ by fitting to experimental data. But the change of the electrical insulating property due to varied SEI components was not considered in previous research. Using *ab initio* molecular dynamics (AIMD) and constrained DFT (cDFT), Leung demonstrated the energy barrier provided by a $0.7\sim 1\text{ nm}$ thick artificial oxide SEI can slow down the electron transfer rate because of its electron tunneling barrier [52][53]. But this study was specifically for the artificial oxide SEI without including other SEI components. Thus, how to quantify and rank the electrical insulating property of SEI components is still unknown.

Second, the connection between the electrical insulating property of SEI and the initial capacity loss during battery cycling has not been established. If the electrons are not completely blocked by SEI, SEI will continue growing since the decomposed product can still be generated by the reduction reaction. The consumed active Li ions due to the formation or continuous growth of SEI are the main cause of the irreversible capacity loss during the cycling of Li-ion batteries. Therefore, it is worth investigating the stable condition of SEI and its connection with the irreversible capacity loss during battery cycling. On the carbon anode in conventional Li-ion battery, a thin and stable SEI forms during the first cycle by consuming $10\sim 20\%$ initial capacity. This is beneficial to inhibit capacity fading in following cycles. In the inspiring research by Joho *et al.* [54], the irreversible capacity loss of various carbon anode materials was measured. A linear relationship was found between the irreversible capacity and BET surface area of carbon anode. That implied the thickness of SEI formed on the all carbon anode was similar. To further decrease the initial irreversible capacity loss, SEI components that can block the electrons by consuming fewer Li-ions were desired. Thus, understanding the connection between the electrical insulating property of SEI components and the irreversible capacity loss due to initial SEI formation is still needed.

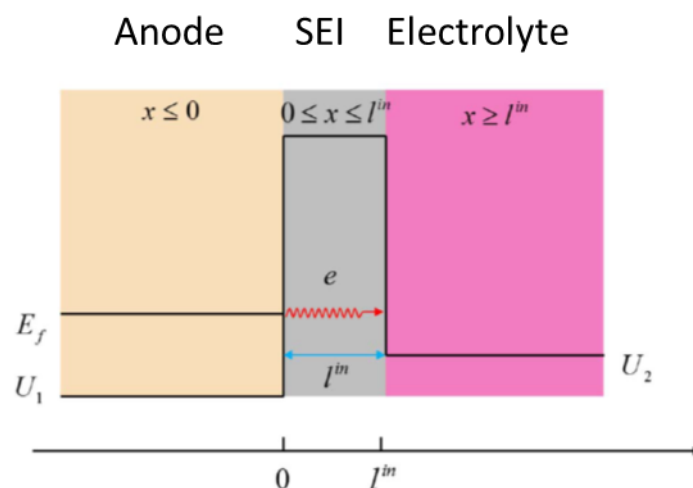


Figure 1.6 One-dimension rectangular barrier model for electron tunneling through the SEI layer [51]. (Copyright from Journal of the Electrochemical Society 2015)

Apart from the initial capacity loss in the first cycle, any electron leaking through SEI may continue the capacity fading in the following cycles. One degradation mechanism is the electron leaked from SEI induces more electrolyte reduction when SEI cracks. According to the analytical model by Verbrugge *et al.*, SEI was mechanically stable on graphite but could not tolerate the large volume expansion of Sn (250%) or Si (400%) due to lithiation [55][56]. Since Li-metal anode used in Li-S battery is not an intercalation anode, the stripping and plating process of the Li-metal anode will involve large deformation and induce the dendrite growth, which cannot be tolerated by naturally formed SEI [57]. Instead, SEI will form and crack repeatedly in the following cycles, leading to an irregular and thick SEI with a high irreversible capacity loss[20]. Even when SEI does not crack, elastic deformation may still lead to more electron tunneling. For example, for the graphite anode with only 10% volume expansion upon lithiation can still cause capacity fading in during the battery cycling [58], which indicated that the electrical insulating property of SEI was also subject to change due to the stress in the SEI caused by deformation of anode materials. This was reasonable since the stress causes the change in tunneling behavior for similar materials, such as InGaAs/AlInAs quantum well [59] and InGaAs quantum dot molecules [60]. Thus, how the stress influences the electrical

insulating properties of the SEI and contributes to the irreversible capacity loss in the following questions remained another question [61][62].

In this thesis, we would like to address three problems related to the electrical insulating property of SEI and the irreversible capacity loss. 1) How to quantify and rank the electrical insulating property of SEI components; 2) How to connect the electrical insulating property of SEI components with the irreversible capacity loss due to the initial SEI formation; 3) how the stress caused by the deformation of anode materials influences the electrical insulating property of SEI and the capacity fading in the following cycles.

1.3 Current understanding of solvation status of Li-PS

In section 1.3, we will review the current studies related to the solvation of Li-PS, and identify a gap: why the electrochemical performance of Li-S batteries can be influenced by the solvation status of Li-PS.

1.3.1 The influence of Li-PS solvation on the open circuit voltage (OCV)

The OCV represents the discharge curve of a battery cell under equilibrium conditions or measured under very small current. It is very important since the energy density provided by the battery is the area under the discharging OCV curve. We noticed that the solvation of the Li-PS can potentially change the OCV curves of Li-S batteries, influencing both the cycling stability and energy density. Most of OCV curves for Li-S batteries show either one plateau or two plateaus, depending on the solvation of Li-PS. The two-plateaued OCV curves are shown in Figure 1.7a. The first plateau at 2.3~2.4 V has been attributed to the lithiation reaction from elemental S to dissolved Li-polysulfide (Li-PS). The second plateau at around 2.0~2.1 V has been attributed to the continuous lithiation of the dissolved Li-PS to the precipitated crystalline Li_2S_2 and Li_2S . The two-plateaued discharging curves were typically observed in Li-S batteries with ether-based liquid electrolytes [63][64] when the solvation of Li-PSs was available. The

two-plateaued OCV provides high energy density due to the high voltage in the two flat plateaus. The fully solvated Li^+ ions transport fast in the liquid electrolyte. However, the capacity fading is generally very fast due to the Li-PS shuttle. In comparison, the single-plateaued discharging plateau is shown in Figure 1.7b. The single plateau around 2.0 V was believed to be the characteristic of a direct transformation from elemental S to solid state $\text{Li}_2\text{S}_2/\text{Li}_2\text{S}$. The one-plateaued OCV curves were believed to be accompanied by solid electrolyte when no liquid solvent was available to dissolve the Li-PS [65][66]. Because less active S was consumed due to the mitigated Li-PS shuttle problem during battery cycling, the discharging capacity can be maintained high, providing cycling stability. But the high overpotential and slow Li transport process induced by the solid electrolyte will influence the energy density.

Many experimental efforts had been made to achieve one-plateaued OCV curves in a liquid electrolyte to mitigate Li-PS shuttle problem, with or without the intention to change the Li-PS solvation status. This is beneficial since it can combine the cycling stability of one-plateaued OCV and fast Li transport property in the liquid electrolyte. For example, the pore size was designed to be very small either to inhibit the formation of long-chain Li-PS [36,67,68] or entrap Li-PSs by blocking them from the electrolyte [69][70]. With a pore size of 3~5 nm, one-plateaued OCV curves were observed [69,71–73]. Two-plateaued OCV curves were observed with ether-based electrolyte since they have large solubility of Li-PS. When electrolyte solvents with low Li-PS solubility were used, one-plateaued OCV curves were observed [74]. Furthermore, increasing the Li salt concentration in the ether-based electrolyte could also shift the two-plateaued OCV curves to one-plateaued OCV curves [75–78]. These experimental evidences collectively suggest that systematic investigations on how the OCV curves change with the electrolyte solvent status will provide valuable information to achieve one-plateaued OCV curves in a liquid electrolyte.

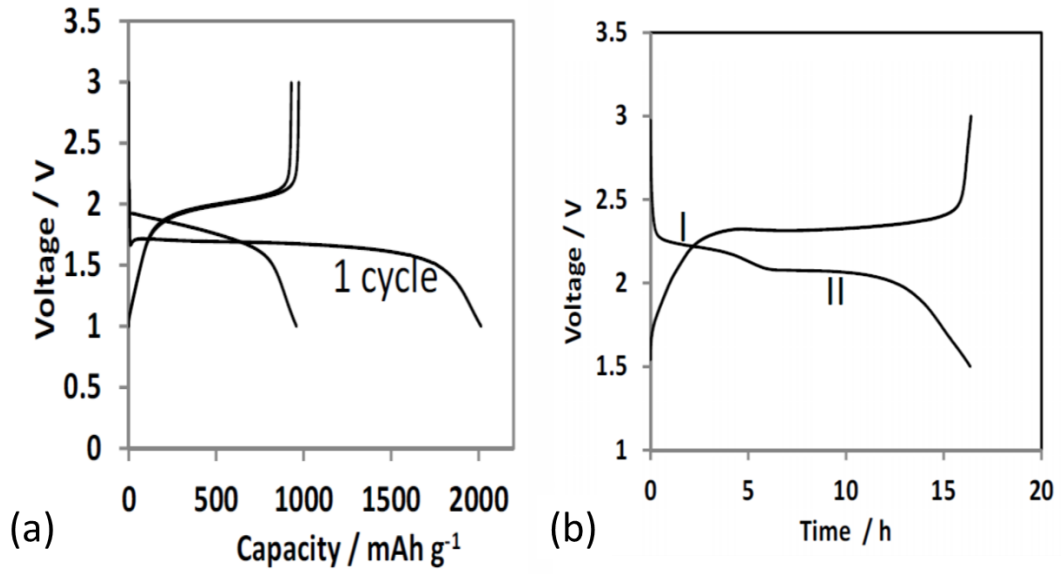
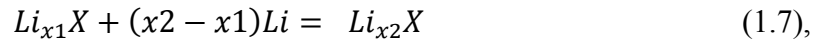


Figure 1.7 Two-plateaued (a) and one-plateaued (b) discharging OCV curves observed in Li-S batteries summarized by Markevich *et al.*[79]. (Copyright from Journal of The Electrochemical Society 2017)

On the computational front, DFT prediction of the OCV curves in a Li-S battery is not satisfied yet, despite the routine use of DFT to predict the OCV in solid electrodes. Consider a typical lithiation reaction:



The average OCV with reference to Li-metal as 0 V is defined as

$$\langle OCV \rangle = \frac{-\Delta G}{\Delta xe} = \frac{-[G(Li_{x_2}X) - G(Li_{x_1}X) - (x_2 - x_1)G(Li)]}{(x_2 - x_1)e} \quad (1.8),$$

where ΔG is the change of Gibbs free energy in reaction (1), Δx is the transferred number of electrons, and e is the charge on one electron. $G(Li_{x_2}X)$, $G(Li_{x_1}X)$ and $G(Li)$ are the Gibbs free energy of phase $Li_{x_1}X$, $Li_{x_2}X$, and Li-metal, respectively. For electrodes that store lithium via intercalation [80][81] and alloying [82][83] solid-state reactions, the OCV has long been predicted by calculating the reaction energy through DFT.

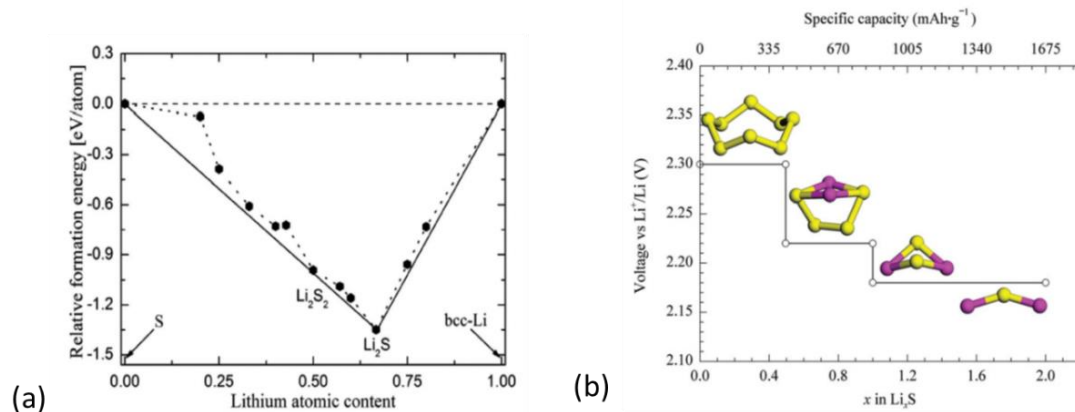


Figure 1.8 (a) Convex hull of Li-S systems from DFT calculation by Yang *et al.* [84]. (b) Predicted OCV curve from DFT calculation with solvation and temperature effect included by L. Wang *et al.* [85]. (Copyright from Journal of Materials Chemistry A 2015 and Journal of Energy Chemistry 2013.)

Predicting the solvent and temperature dependent OCV curves in Li-S battery accurately remains a problem. This is mainly due to the complicated discharging reaction involving both the solid and liquid structures. In fact, if the lithiation reaction of S was modeled as a solid-state reaction, Li_2S would be the only thermodynamically stable phase, consistent with the Li-S phase diagram [86]. This is further supported by the convex hull of Li-S systems calculated by Yang *et al.* [84]. As shown in Figure 1.8a, all long-chain crystalline Li-PS lied above the tie-line between crystalline S and Li_2S [84], suggesting that they were not a stable mid-phase during the discharging reaction. Therefore, one-plateaued OCV curves were predicted, which is not consistent with two-plateaued OCV curve observed experimentally with liquid electrolyte. This inconsistency required the inclusion of the solvation and temperature effect for the dissolved Li-PS in the calculation. Thus, one of the goals of this thesis is to develop a DFT-based computational approach to predict the influence of the solvation effects at finite temperature on the prediction of OCV in Li-S batteries.

1.3.2 Influence of micrometer level pore structure on the energy density

The practical energy density of Li-S battery is highly related to the evolution of Li-PS

solvation status with the pore structure and the amount of electrolyte. Considering a typical Li-S battery with liquid electrolyte and micrometer level pore carbon matrix, a two-plateaued discharging curve is generally observed since Li-PS are fully solvated. In the early researches, unlimited amount of electrolytes were added in Li-S batteries, making the ratio between the electrolyte and S (E/S ratio) greater than 10 ml/g [87]. Even though the addition of electrolyte will not affect the energy density of the electrode, it will decrease the energy density of the whole battery by increasing the total weight and volume of the battery. However, if there is too less electrolyte, the change of solvation status can lead to low utilization of S, directly decreasing both the cathodic energy density and the battery level energy density. It is estimated that to achieve an energy density of 300 Wh/kg comparable with commercial Li-ion battery, an E/S ratio of 3 mL/g is required in state of art Li-S pouch cell [15]. Therefore, the influence of E/S ratio on the electrochemical performance and energy density of Li-S battery was subjected to investigation.[88,89] However, a single parameter of E/S ratio is oversimplified since it cannot demonstrate how much of the electrolyte can be actually used for the dissolution of Li-PS, nor it giving any information on the design of cathode porous structures.

Researches have shown that the macropore structure in the carbon matrix will affect the solvation of Li-PS, influencing the shape of two-plateaued OCV curves. It was first reported by Zheng *et al.* [90] that the pore structure in the carbon matrix of the S-C cathode had a significant influence on the second plateau. As shown in Figure 1.7a, a flat second plateau was observed with a carbon matrix of the high surface area and pore volume, leading to high energy density. A depressed second plateau was observed with a low surface area and pore volume, leading to low energy density. However, since the comparison was made between different carbon matrixes sharing different kinds of pore structure and synthesise method, the conclusion still needed further validation to exclude the influence of undesired variables. Recently, a more systematic comparative study was done by changing the porosity of the same carbon matrix

through a calendaring process. Figure 1.9 showed the charge-discharge profile of Li-S cells with sulfur loading of 5 mg/cm^2 at a porosity of 70%, 60%, 50%, and 40% respectively. The change of the OCV curves due to porosity dramatically impact the practical energy of the cell, demanding a more sophisticated analytical model to integrate the porosity information with the discharge curves, instead of simply taking the E/S ratio.

Therefore, this thesis will develop an analytical model to quantify the influence of porosity on the discharging curve. With such a model, the optimum energy density of Li-S batteries can be achieved by the design of porosity in the cathode. This model will include the Li-PS dissolution mechanisms and the formation of insulating Li_2S on the carbon matrix surface.

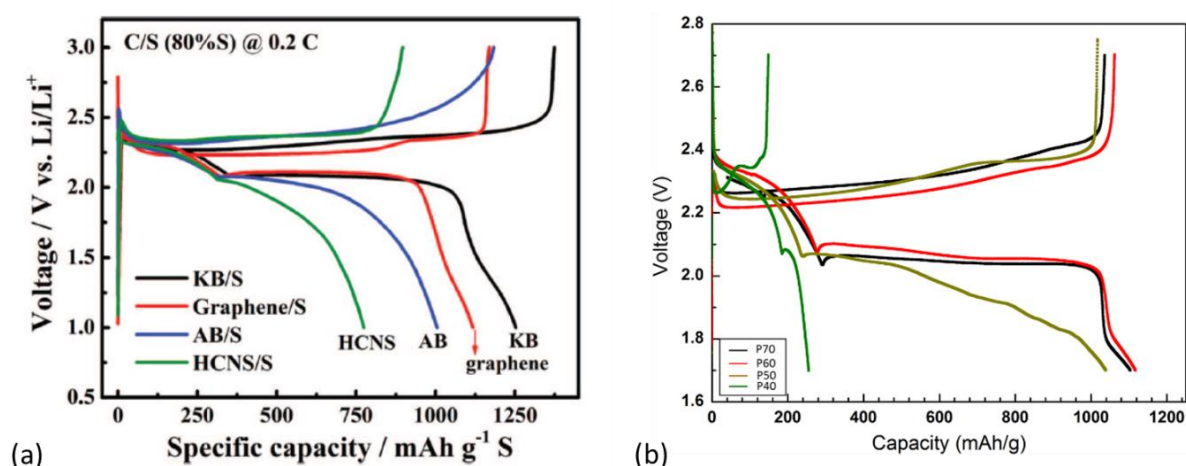


Figure 1.9 (a) Discharging curves of Li-S batteries with different carbon matrix observed by Zhang *et al.* [90] with relatively large pore volume. (Copyright from Journal of the Electrochemical Society 2013) (b) Discharging curves of Li-S batteries observed by further decreasing pore volume.

1.3.3 Influence of nanopores and sub-nanopores on the mitigation of Li-PS shuttle problem

The size of nanopore and sub-nanopore is also important as it can provide more precise control of the solvation status of Li-PS and may prevent the Li-PS shuttling. As discussed in

Section 1.3.1 various carbon materials with different pore size had been used for the carbon matrix in S-C cathodes. Typical examples with smallest pore size included 3 nm mesopore carbon [71], 0.5 nm micropore carbon [67] and 5 nm open rings in the walls of CNT [69]. The design motivation includes entrapping Li-PSs by blocking them from the electrolyte [69][70]. At the nanometer level, if the nanopore size is small enough to block the transport of Li-PS solvation shell, while still allows the transport of Li ions in the electrolyte solvents, the concentration of Li-PS inside the nanopore may change. More ideally at the sub-nano level, when only the Li ions are allowed to transport through the pore, while the solvent molecules and are kept out, there will be no solvent inside the sub-nano pore to solvate the generated Li-PS. However, what is the ideal pore size? Although some previous computational models have compared the sizes of PS, electrolyte solvent, and pore in carbon matrix [63][91], the optimum pore size has not been determined.

In this thesis, we will computationally design the ideal sized CNT. CNT has a more controlled size and morphology compared to other types of carbon matrix materials. In addition, CNTs offer many advantages as the cathode for Li-S batteries, such as high thermal and electrical conductivities [92][93], good mechanical properties [94], high surface area [95]. Their hollow space inside could also provide room for storage of sulfur. In one inspiring experiment by Fujimori [70], the 1D sulfur chain was encapsulated into CNT with 2nm diameter through the opened caps. DFT calculation supported weak interactions between S and CNT, leaving a possibility for S to react with Li. Sulfer can be evaporated into the CNT if there are opening on the CNT. These opening can then be used to selectively allow Li^+ ion diffusion but not electrolyte diffusion. The opening structures in CNT could be tuned by the oxidation process. Furthermore, the open rings in the walls of the CNTs could increase its size with the level of oxidation [96], change its size and chemistry with the oxidants [97] and temperature [98], and even destroy the CNT structure under a very strong oxidation condition [99]. These

experiments suggested the feasibility to control the size of open rings in CNTs by controlling the oxidation processing conditions.

The remaining design questions: a) what is the optimum pore size that can selectively allow Li transport and completely block the electrolyte solvent, and b) what is the relationship between the created pore size and the oxidation condition in CNT. Few similar simulations can be found in carbon systems that are related to the current work. For example, by calculating the transport energy barrier as a function of the pore size from DFT calculation, Zhang *et al.* successfully predicted that the selective transportation provided by the pore structure in graphdiyne and rhombic-graphyne enabled H₂ separation and purification from different gas mixtures [100]. With the aid of MD simulation, Jiao *et al.* [101] and Song *et al.* [102] also investigated how gas transportation will be affected by the defects in graphene oxides membranes and coal. Thus, an integrated model that can determine the optimum pore size using DFT and further predict the oxidation processing conditions to create the optimum pore size using (MD) method will be developed in this thesis.

1.4 Highly concentrated electrolytes

A new class of electrolyte, highly concentrated electrolyte, is emerging and shows many promising properties. We will further review its unique properties and how it impacts the electrode/electrolyte interface; and then identify a remaining gap: how to improve its viscosity by tuning its unique solvation structures.

1.4.1 Forming SEI in highly concentrated electrolytes

Recently, a specific kind of highly concentrated electrolyte was designed to expand the narrow electrochemical window of some electrolyte through a uniquely formed SEI. For example, the aqueous electrolyte with clean water as solvent was obviously safer and more environmental friendly than the organic electrolyte. However, as shown in Figure 1.10, the 1.23

V electrochemical window of water is too narrow [103]. One famous example in the field of the aqueous electrolyte was the “water in salt” electrolyte by Suo *et al.* [104]. By increasing the concentration of LiTFSI salt in the aqueous electrolyte, an SEI containing LiF was formed on the surface of the anode and the reduction of water was suppressed. The electrochemical operating window had been largely widened to 3.1 V, as shown in Figure 1.10. The unique formation of SEI was attributed to the change of the solvation structure in the highly concentrated electrolyte. The fully solvated Li salt decomposition window is out of the electrochemical window of water, so no SEI can be generated on the electrode surface, without water decomposition first [6]. Instead of existing as fully solvation shell and free solvent under low concentration, the dominating solvation structures under high concentration became large complex and aggregated network. This change in solvation shell raised the reduction potential of LiTFSI salt while lowered the reduction potential of water solvent, enabling the formation of SEI through the decomposition of Li salt. The “water in salt” electrolyte had been successfully coupled with lots of electrodes in Li-ion battery, including Li_2MnO_4 [104] and LiFePO_4 [105] cathode, Mo_6S_8 and TiS_2 [106] anode. Its wide application had also been extended to other energy storage devices with Li metal anode, such as Li-S battery [107], Li-air battery [108]. In a typical concentration, the “water in salt electrolyte” contained the LiTFSI or LiTFSI as the Li salt, and the water as the solvent.

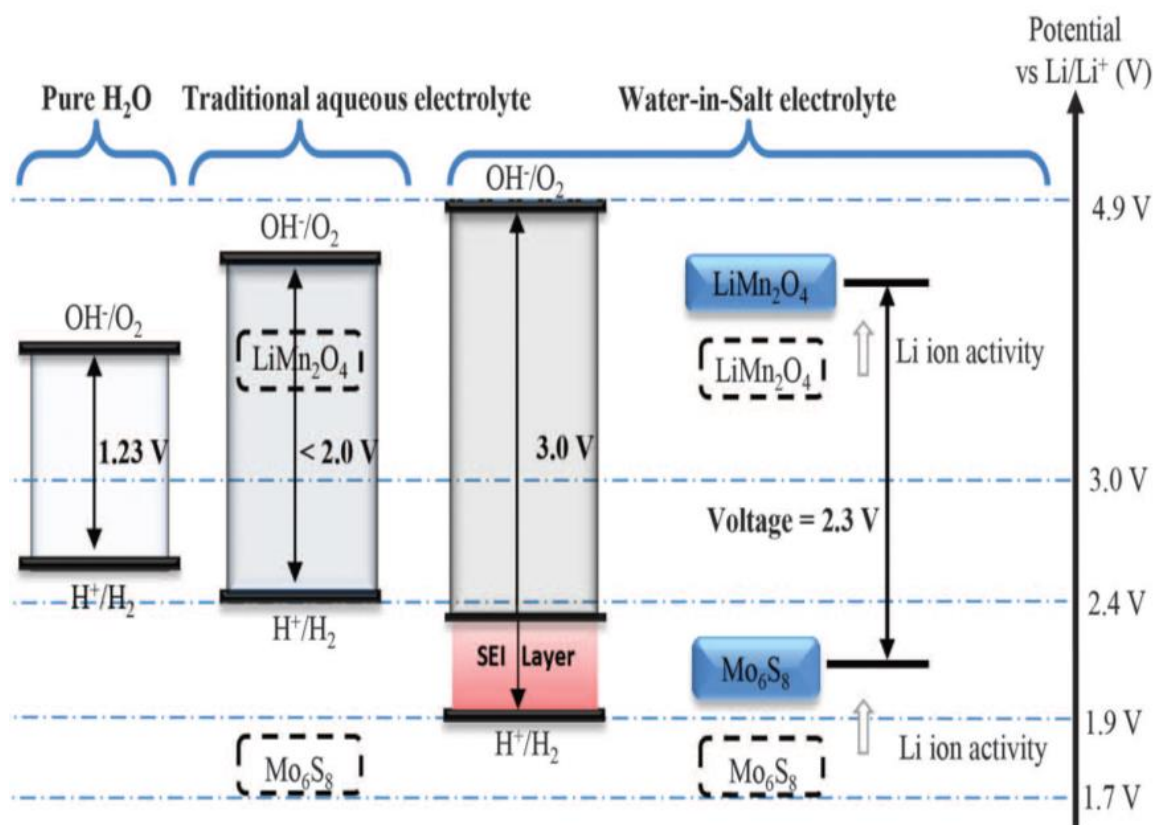


Figure 1.10 Illustration of expanded electrochemical stability window for water-in-salt electrolytes together with the modulated redox couples of LiMn_2O_4 cathode and Mo_6S_8 anode caused by high salt concentration [104]. (Copyright from Science 2015)

Coupling Li-metal with some electrolytes with narrow electrochemical windows is a long-lasting challenge. Ethyl acetate (EA) based electrolyte was reported to facilitate the operation of rechargeable Li-ion batteries at a low temperature of $-70\text{ }^\circ\text{C}$, at which most commercially used electrolytes were already frozen [109]. Again, the electrochemical window from 1.5 V to 3.8 V and unstable decomposition product of EA hindered its coupling with Li metal. Following the idea of highly-concentrated electrolyte concept, the narrow electrochemical window of EA-based electrolyte could also be expanded by increasing the concentration [110]. This enabled the coupling of Li metal anode and EA-based electrolyte at room temperature.

1.4.2 Co-solvent in the concentrated electrolyte at low temperatures

The use of concentrated electrolyte brought a new challenge: Li-ion transport property would be influenced by the solvation structure. For example, the viscosity of “water in salt”

electrolyte was 36 mPa·s, which was almost 10 times higher than that the value of 3.7 mPa·s in a 2mol/kg aqueous LiTFSI electrolyte [28]. This influence was even enlarged for the EA-based electrolytes working at low temperatures. For 1mol/kg LiTFSI in EA-based electrolyte, the viscosity was 30.5 mPa·s, at -70 °C. At 5 mol/kg, the viscosity turned to 1.06×10^5 mPa·s. The high viscosity in concentrated electrolyte was very harmful to the transport of Li ions [110].

A co-solvent approach, by adding another solvent to the concentrated electrolytes, can be used to improve the transport of Li ions in the concentrated electrolyte. As a good co-solvent, the formation of SEI, which was responsible for the expanded electrochemical window in the concentrated electrolyte should also be maintained. Ren [111] reported that the viscosity of concentrated sulfone-based electrolytes decreased from 99.5 mPa·s to 14.1 mPa·s after adding a fluorinated ether co-solvent. The Li-transport property was also improved. Zheng also showed that the hydrofluoroether co-solvent in concentrated ether electrolyte can improve its high viscosity and poor wettability [112]. In both types of research, the expanded electrochemical window in concentrated electrolytes was maintained after adding co-solvent. With the aid of MD simulation, it is demonstrated that the unchanged solvation structure after adding co-solvent is the key [112]. According to Dong *et al.* [110], dichloromethane (DCM) with a low freezing point of -95 °C, also served well as a co-solvent to improve the transport of Li in concentrated EA electrolyte when operating at -70 °C.

In this thesis, integrated DFT and MD simulations will be used to reveal the solvation structure of the DCM co-solvent in EA-based electrolyte, and its relationship with the electrochemical window. Furthermore, the influence of temperature on the Li transport property in the co-solvent electrolyte will also be focused, as creating electrolyte flowing at -70°C will dramatically broaden the range of rechargeable lithium ion battery applications, especially for space applications. With a better understanding of the co-solvent mechanism, we can establish a screening criterion for possible co-solvent for low-temperature batteries. This

can provide great help in the design of electrolytes used at low temperatures.

1.5 Integrated computational approach

In this thesis, several integrated computational models were developed to connect the electrode-electrolyte interface mechanisms with the battery discharge curves and the initial capacity loss. The new insights obtained from these models were used to design coatings on the anode, porous structures of the carbon-sulfur cathode, and the electrolyte. The chapters are outlined as follows.

2 Connecting irreversible capacity loss with electrical insulating properties of SEI components

Starting from the anode side, this chapter aimed to establish the relationship between irreversible capacity loss and the electrical insulating property of SEI components on the anode. Assuming the electron tunneling from the electrode to the electrolyte is blocked by the SEI inorganic components at a critical thickness, based on the electronic tunneling barrier calculated from DFT, an analytical model was developed to connect the initial irreversible capacity loss with the anode surface area. Good agreement between the modeling prediction and experimental measurements was achieved, confirming that the initial irreversible capacity loss was due to the self-limiting electron tunneling property of the SEI. To explain the continuous growth of SEI due to anode deformation, the influence of stress-induced-strain on the tunneling barriers were also investigated.

3 Predicting open circuit voltage curves in Li-S battery depending on the solvation of Li-polysulfide

Moving to cathode side, it was found that the solvation status of Li-PS (fully, partially, or not dissolved) had a profound impact on both the ideal open circuit voltage (OCV) curves and the practical discharge voltage curves. This chapter addressed the impact of solvation status of

Li-PS (fully, partially, or not dissolved) on the ideal OCV curve. The OCV was first predicted using DFT calculated free energies at finite temperatures along with the solvation energy, for the discharge reactions involving both insoluble crystals and dissolved Li-PS molecules. This model successfully revealed that the solvation energy stabilized the Li-PS. Thus, the formation of the fully solvated Li-PS led to the two-plateaued OCV; while the formation of non-solvated Li-PS was not favorable, so the direct transition from S to Li_2S led to a one-plateaued OCV. The agreement between modeling prediction and the experimental observation confirmed that the origin of the one-plateaued or two-plateaued discharging curves is clarified to the solvation of the Li-PS.

4 S-C cathode design with micrometer level pores: achieving high energy density by changing the porosity

Continuous investigation on the solvation status of Li-PS in this chapter focused on the its evolution with electrolyte amount, and its influence on the practical discharge voltage curves. A mechanism based analytical model was developed to evaluate the influence of micrometer level porosity on the discharging curves by connecting the amount of electrolyte, the volume of the pores, the solubility of Li-PS in the electrolyte, and the surface area of the pores. It was determined that the length of the first plateau was limited by saturation of Li-PS, and the overpotential in the second plateau would increase dramatically when the surface area of carbon matrix was not enough for the deposited $\text{Li}_2\text{S}_2/\text{Li}_2\text{S}$ layer. The predicted discharging curves agreed well with that observed in the experiment. This model was used to optimize the porosity of the carbon matrix to maximize the volumetric energy density of Li-S batteries.

5 S-C cathode design with nanopores: synergetic effect between pore size and electrolyte concentration to mitigate lithium polysulfide shuttle problem

Using nanopore and sub-nanopore could provide more precise control of the solvation status of Li-PS to prevent the Li-PS shuttling. This chapter demonstrated how to achieve

partially solvated Li-PS to mitigate the Li-PS shuttle problem with nanopores. The formation of Li-PS could be suppressed if it was only partially solvated, as suggested by the DFT calculations. Since decreasing pore size to nanometer level and increasing electrolyte concentration could both create partially solvated Li-PS, a new strategy to mitigate “Li-PS shuttle problem” based on this synergetic effect was proposed by modeling and verified by experiments.

6 S-C cathode design with sub-nanopores: optimum pore size to prevent Li-PS formation

Moving into sub-nanometer scale, this chapter focused on a more idealized case when sulfur was filled in carbon nanotubes (CNT), with the open ring size that is only permeable to Li ions. The optimum pore size was determined by calculating the Li transport barrier through open rings and comparing the molecular size of selected molecules with the open ring size from DFT. MD simulation further showed that the as-determined optimum ring size could be generated by controlling the oxidation parameter of CNT.

7 Improvement of Li transport property of concentrated low-temperature electrolyte by adding co-solvent

The highly-concentrated electrolyte can achieve the partially solvated Li-PS, and even expand the electrochemical stability window of the electrolyte if an SEI is formed. However, its high viscosity results in very slow Li transport. In this chapter, a co-solvent structure was designed by adding electrolyte low viscosity and electronically stable dichloromethane (DCM) to the highly-concentrated LiTFSI in ethyl acetate (EA) solvent. The contention of the DCM was designed to obtain a unique solvation structure, where clusters of partially solvated Li⁺, TFSI⁻, and EA network were surrounded by the DCM cosolvent so that the former inherited the expanded electrochemical window of the highly-concentrated salt and the latter accelerated the Li transport.

2 Connecting irreversible capacity loss with electrical insulating properties of SEI components

2.1 Summary

The formation and continuous growth of solid electrolyte interphase (SEI) layer are responsible for the irreversible capacity loss of batteries in the initial and subsequent cycles, respectively. In this chapter, the electron tunneling barriers from Li metal through three insulating SEI components, namely Li_2CO_3 , LiF and Li_3PO_4 , were computed using DFT calculations. Based on the electron tunneling theory, it was estimated that 2nm of LiF or 3nm of Li_2CO_3 were sufficient to block electron tunneling. It was also found that the band gap decreased under tension while the work function remained the same, and thus the tunneling barrier decreased under tension. A new parameter, η , characterizing the average distances between anions, was proposed to unify the variation of band gap with strain under different loading conditions into a single linear function of η . An analytical model based on the tunneling results was developed to connect the irreversible capacity loss, due to the Li ions consumed in forming these SEI component layers, and the surface area of negative electrodes. The agreement between the model predictions and experimental results suggested that the initial irreversible capacity loss was indeed due to the self-limiting electron tunneling property of the SEI. It suggests that LiF is a more desirable insulating coating material when the initial capacity loss is not a concern while Li_2CO_3 may be preferred in naturally formed SEI since it causes less capacity loss.

2.2 Introduction

The grand challenge for rechargeable lithium-ion batteries (LIB) in electric vehicles is to simultaneously improve the battery performance, life, cost, and abuse tolerance [113][1]. In current lithium-ion batteries, the operating voltage of anode is below the reduction voltage of

electrolytes, resulting in electrolyte decomposition into a thin layer formed on the electrode surface. This thin layer is believed to be electronically insulating, preventing further electrolyte reduction reactions. However, it is Li-ion (Li^+) conductive. So it is generally referred to as SEI [114][12][115]. The formation and continuous growth of SEI consume active lithium ions, becoming the main cause of the irreversible capacity loss in the initial and subsequent cycles, respectively. Generally, a “stable” SEI on a graphite anode surface, mainly formed during the first cycle by consuming about 10% ~ 20% of the initial capacity, should provide the excellent cycling performance of graphite anode materials [116][62]. However, no “stable” SEI had been found to form on high capacity anode materials such as Si, Sn and Li metal, due to their large deformation during cycling [117][118][119]. Given this condition, many efforts had been made to develop coating materials to protect the anode surface as an artificial SEI layer [120][121]. It was anticipated that a stable artificial SEI layer should also block the tunneling of electrons and allow the transfer of lithium ions. Ideally, when electrons were completely blocked by the SEI from the electrolyte, the SEI would stop growing and become stable. Further considering that many of these coatings materials are dense inorganic compounds, such as Al_2O_3 , TiO_2 and TiN [120][122], it was believed that the electrical insulating property of inorganic components in both naturally formed and artificial SEI was the key to the stable condition of SEI. However, open questions still remained: what is the electrical insulating mechanism and how the SEI contributes to the irreversible capacity loss at the first cycle and the capacity fading in following cycles?

Quantum tunneling was a well-understood quantum mechanical phenomenon that a subatomic, particle can pass through a potential barrier with a certain probability, instead of totally being blocked as assumed in classical mechanics. This probability was decided by the shape and the width of the potential barrier. Application of quantum tunneling in the electrical insulating mechanism was first put forward by Peled *et al.* [50]. Assuming a rectangle barrier

with a constant height, the SEI has to be thick enough to block electrons completely. In following researches, the electronic tunneling height and width in SEI were generally evaluated as an overall property of the whole SEI. Based on an analytical model by Li, the height was estimated to be 2.8~2.9eV [51]. From the *ab initio* molecular dynamics (AIMD) and constrained DFT (cDFT) calculation by Leung *et al.*, a thin SEI layer with a thickness of 0.7~1 nm can slow down the electron transfer rate because of their electron tunneling barrier [52][53]. However, a quantified comparison among electrical insulating property of different SEI components was seldom conducted, and little effort has been made to connect the electron insulating ability of different SEI components to battery capacity loss. This was of extreme importance in the screening of artificial SEI and designing electrolytes to tune the composition of SEI.

In fact, the thinness, diversity, complicate formation mechanism, along with the chemical sensitivity and high cost of *in situ* characterization methods [123][124][125], all add difficulties to a clear understanding of the basic property of SEI, such as mechanical, Li transport and electrical insulating properties. Investigations on the material properties of single SEI component either computationally or experimentally have provided important insights for understanding SEI in general. For example, the mechanical properties of bulk LiF and Al₂O₃ have both been measured and computed [126][127][128][129]. The lithium ion transport mechanisms in LiF, Li₂CO₃, Li₃PO₄, and NaF were investigated intensively by first-principles calculations [130][131][46][45]. In terms of quantification of electrical insulating property, progresses were also made in applying density function theory (DFT) to calculate electronic tunneling in different applications, such as the gold/electrolyte interface [132][133], molecular transistors [134], Schottky barriers formed by metal/CNT [135] and metal/h-BB [136]. All these researches inspired us to investigate the electrical insulating property of single SEI component.

It is well known that the deformation of the anode during cycling would influence the property of SEI. For intercalation anodes such as graphite, Si, and Se, this deformation was caused by the volume expansion upon lithiation. Verbrugge *et al.* have developed an analytical model for a core-shell structure [58][59], and found the SEI shell will be mechanically stable on graphite but will not tolerate the large deformation of Sn or Si [55][56] due to lithiation. For Li metal anode, the deformation was related to the utilization percentage of Li during cycling. However, it is not clear if the stress in SEI induced by electrode volume expansion [139] will change the electronic tunneling properties of the SEI components. This information is especially important for the understanding of how the repeated volume expansion and contraction gradually cause the increase in reversible capacity loss and electrode degradation in the following cycles [62][61].

In this chapter, we chose two inorganic components commonly found in naturally formed SEI, such as LiF and Li₂CO₃, and another possible artificial SEI Li₃PO₄ with excellent chemical stability, insulating property, ionic conductivity, and mechanical property [4][140][130]. In this chapter, we will first introduce model details about how to calculate the electronic tunneling barrier, predict capacity loss due to SEI formation and investigate the influence of stress were introduced. Then, the values of DFT predicted work function and band gap are listed and discussed. Afterward, the capacity loss due to SEI thickness and tunneling barrier is predicted and compared with experimental results. At last, a further investigation of the influence of stress on the predicted electronic tunneling barrier and capacity loss is conducted.

2.3 Model details

2.3.1 DFT computed electron tunneling barrier and its relation with capacity loss

As SEI is the interphase between anode and electrolyte, if any excess electron from the electronic conducting electrode tunnels through the electronic insulating SEI component to

reach electrolyte, it has to overcome the electronic tunneling energy barrier (ΔE_t) from the Fermi level (e_f) of lithium anode to the bottom of the conduction band of SEI component, as illustrated in Figure 2.1. Furthermore, the Fermi level of electrolyte is lower than that of the anode and the SEI [141][142]. If the electron can tunnel through the SEI, it can easily transfer to the lowest unoccupied molecular orbital (LUMO) of the electrolyte, causing reduction reaction of the electrolyte. By aligning the Fermi level (e_f), work function (Φ) and band gap (E_g) of the lithium anode and SEI to the common reference, vacuum, the electron tunneling barrier (ΔE_t) can be obtained by

$$\Delta E_t = E_g(SEI) - \Phi(SEI) + \Phi(Li_electrode) \quad (2.1),$$

in which all the parameters can be obtained through DFT calculation.

According to the 1D WKB tunneling theory in quantum mechanics [143], the electronic insulating ability of the SEI components can be evaluated by the tunneling probability (T),

$$T = \frac{16\varepsilon_f \Delta E_t}{(\varepsilon_f + \Delta E_t)^2} e^{-\frac{4\pi d}{h} \sqrt{2m \cdot \Delta E_t}} \quad (2.2),$$

where d is the thickness of SEI, m is the mass of electron and h is Planck constant. As we noted in the WKB approximation in quantum tunneling, the obtained tunneling probability in Equation (2.2) is actually determined by $\sqrt{\Delta E_t} d$. Thus, the contribution of electrostatic step at the interface is much less important than that from the bulk region. This is the reason that the bulk structures are used in the calculation.

Given this relationship, a simple predictive model can be further developed to estimate how much the irreversible capacity loss, C_{ir} , is in the first few cycles. This is the amount of Li consumed to form the SEI layer that reaches the critical thickness, d^* , to block electron tunneling on the electrode surface. Assuming that complete electron insulating is achieved when $T = e^{-40}$, the critical thickness of SEI, d^* can be obtained from Equation (2.2).

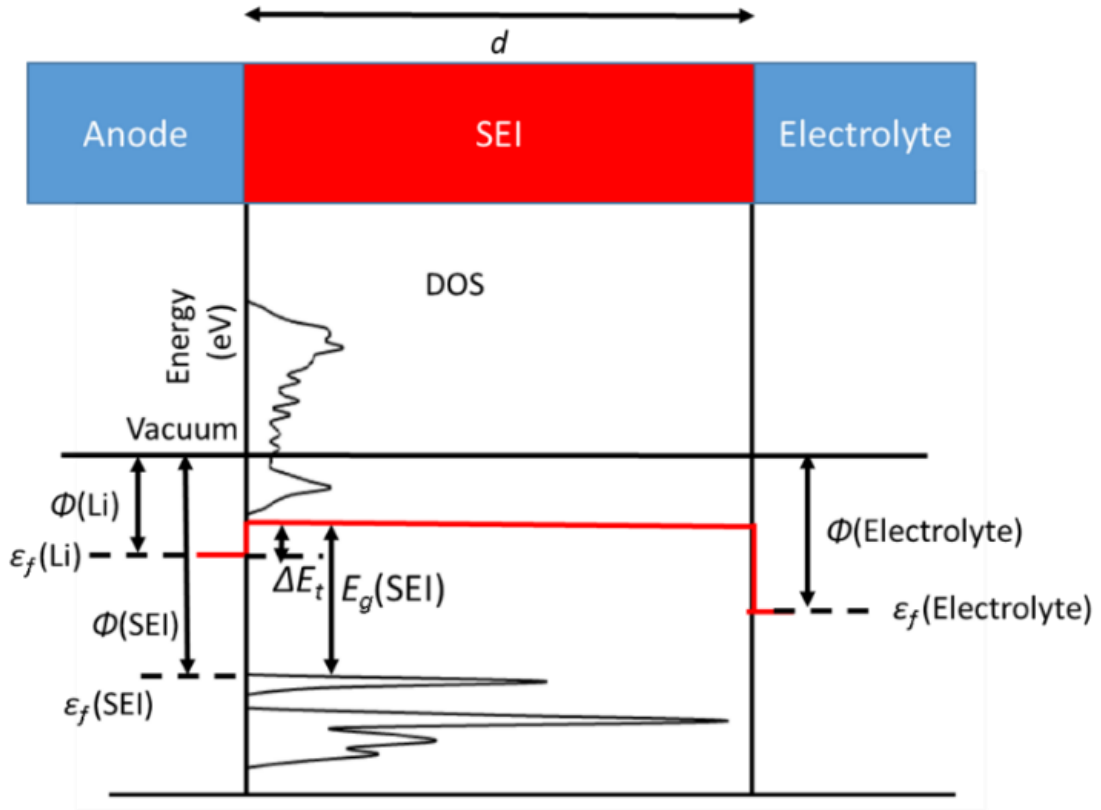


Figure 2.1 Calculation of electron tunneling barrier (ΔE_t) by aligning the Fermi level (ϵ_f), work function (Φ) and band gap (E_g) of the lithium anode and SEI.

The number of lithium ions consumed (N) in the SEI component that forms on a unit surface area of anode is

$$N = \rho d^* \quad (2.3),$$

where ρ is the number of lithium ions per unit volume in the SEI component. The irreversible capacity loss is typically defined as the ratio between the lithium ions lost in SEI formation and the cycling lithium ions stored in the host electrode. Thus, the irreversible capacity loss (C_{ir}) due to SEI formation on an anode can be represented as

$$C_{ir} = \frac{M_h A_h \rho d^*}{N_h N_a} \quad (2.4),$$

where M_h is the molar mass of the host material, N_h is the number of Li ions stored per host atom, A_h is the Brunauer–Emmett–Teller (BET) specific surface area (area/weight) of the host material, and N_a is the Avogadro constant. According to equation (2.4), there is a

linear relationship between C_{ir} and A_h . Therefore we define their ratio as the specific area irreversible capacity loss, C , as $C = \frac{C_{ir}}{A_h}$. To facilitate a comparison with the experimentally measured irreversible capacity loss on various types of graphite [54], C for graphite can be represented as $C = \frac{C_{ir}}{A_h} = \frac{6M_h\rho d^*}{N_a}$.

2.3.2 Loading conditions estimated by stress-strain relationship

In order to investigate how electronic tunneling barrier and probability will change under stress, various states of strain were imposed on LiF. Verbrugge *et al.* developed an analytical model for a core-shell structure and found the hoop stress in the SEI layer may lead to fracture and delamination [58][59]. Thus, we will mainly focus the normal stress rather than shear stress in the SEI. Various loading conditions can be imposed on an SEI and result in normal strain, according to stress-strain relations for linear elastic solid,

$$\begin{pmatrix} \varepsilon_{11} \\ \varepsilon_{22} \\ \varepsilon_{33} \end{pmatrix} = \frac{1}{E} \begin{pmatrix} 1 & -\nu & -\nu \\ -\nu & 1 & -\nu \\ -\nu & -\nu & 1 \end{pmatrix} \begin{pmatrix} \sigma_{11} \\ \sigma_{22} \\ \sigma_{33} \end{pmatrix} \quad (2.5),$$

where σ , ε , ν and E are stress, strain, Poisson ratio, and Young's modulus, respectively.

LiF was chosen as a representative SEI component for this study because its cubic symmetry allows a unified model to describe the dependence of band gaps on the strain. In this study, four different loading conditions were applied on bulk LiF, including hydrostatic stress, uniaxial strain, uniaxial stress, and biaxial stress. The lattice of LiF has deformed according to the strain tensors in each loading conditions expressed in terms of dimensionless stress, σ/E , and the Poisson ratio of 0.326 [144].

2.4 Results and discussion

2.4.1 Work function and band gap

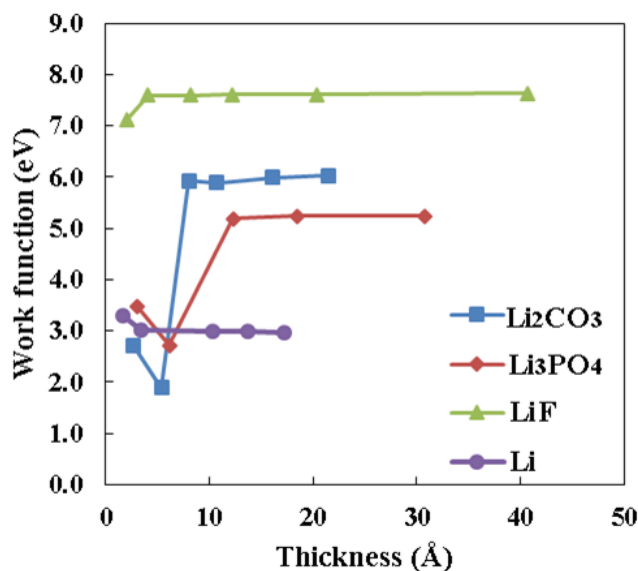


Figure 2.2 Work function of Li₂CO₃, Li₃PO₄, LiF, and Li as a function of slab thickness.

The surface relaxation, surface energy, work function, and band gap may show oscillation with slab thickness and the surface termination due to quantum size effect, an effect caused by different quantization of states of slab model compared with a semi-infinite sample due to the lowering of dimensionality[145][146][147]. Therefore, it is important to develop a slab model that mimics the bulk property (eg. layer spacing) and leads to the converged properties. The surface energy was computed for layer thickness from 1 to 10. The converged surface energies were determined to be 0.163 J/m² for Li₂CO₃(001) with 2 layers; 0.326 J/m² for LiF(100) with 2 layers; 0.925 J/m² for Li₃PO₄(010) with 3 layers, and 0.458 J/m² for Li with 2 layers. The calculated surface energies are consistent with most of the previous calculation [4][148][149].

The calculation of work function was based on these relaxed slab models, and the computed values as a function of slab thickness were shown in Figure 2.2. The work function values of all the four materials oscillate with increasing slab thickness. While the oscillations

of work function in Li and LiF are less than 1 eV, the oscillation in Li_2CO_3 can be up to 5 eV. This brought us to further investigate the relax slab structure in Li_2CO_3 . Figure 2.3 showed the relaxed structure of Li_2CO_3 slab with different atomic layers together with some values of $\angle(\text{CO}_3\text{-}010)$, which represented the angle between the CO_3 plane and $\text{Li}_2\text{CO}_3(010)$ plane. The layer number was also labeled in Figure 2.3, which indicated the position of the layer in the slab model. For example, the layers labeled with 1 indicates the surface layers exposed to vacuum in each slab model. We could see two trends in Figure 2.3. The first trend was that the top surface relaxation becomes consistent in thicker slab models. For example, the angle between the CO_3 plane and the surface plane was 0.2° in the monolayer model and 13.3° in two-layer model. But for the slabs thicker than 3 layers, it become stable at 14.2° . The second trend was that the center of the slab mimics the bulk crystal structure, where this angle was 18.6° . In the 6 layer thick slab model, the angle changed from 14.2° at the surface layer to 18.4° in the second layer and 19.2° in the third layer. These two trends were also valid for slab models of Li_3PO_4 and LiF. The surface layer showed a full relaxation but much less deviated from the bulk compared to Li_2CO_3 . When the slab thickness was more than 4 atomic layers, the oscillation caused by the quantum size effect becomes relatively small, less than 1%. The value of work function was already well converged when the thickness increased to 4 layers. Therefore, it was reasonable to choose this converged value as the work function of the bulk crystal. The calculated work functions was listed in Table 2.1. The widely measured work function of lithium was about 2.95~3.1 eV, which agreed well with our calculation [148][150]. The work function of Li_3PO_4 calculated by Santosh was also in agreement with our calculation [4].

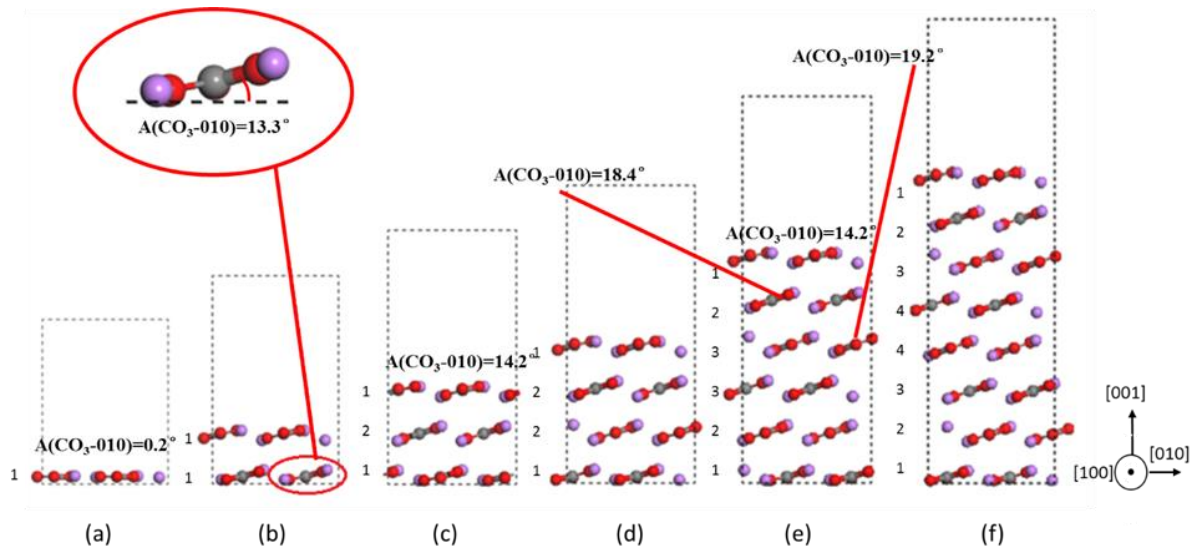


Figure 2.3 Relaxed atomic structure of $\text{Li}_2\text{CO}_3(001)$ slab model with increasing slab thickness.

The band gap calculation was based on bulk crystal structures based on the discussion in 2.1.1. The work function and band gap were all listed in Table 2.1. Our calculated band gaps using DFT/GGA were consistent with other computational data using the same method [151][152][153]. It was well known that calculation by DFT/GGA will underestimate the band gap by up to 50% [154][155][156]. For example, the band gap of LiF measured in the experiment was around 14 eV [157][158][159], which was about 80% larger than all the value obtained by DFT/GGA or DFT/LDA. New functions such as Δ (EIG) method [156], hybrid methods[160], GW methods [161] can, in general, improved bandgap calculations. HSE06 hybrid functions were applied to compute the band gaps for Li_2CO_3 , LiF, and Li_3PO_4 , as listed in Table 2.1. This calculation was done by our partner Kevin Leung from Sandia National Lab. The bandgap of Li_2CO_3 was 7.07eV, consistent with a newly reported experiment value of 7.5eV [162]. The bandgap of LiF and Li_3PO_4 were 10.8 and 8.1 eV, respectively. They were also more consistent with the experiment value of 14.1 and 8.0 eV[51][157]. Nevertheless, the consistent underestimation of band gap values from GGA calculations could still provide reasonable estimates of the electronic insulating behavior of the SEI, especially in the comparison of the three insulating SEI components. Due to this underestimation, the tunneling

barrier would be underestimated as well. Therefore, we applied a very small tunneling probability e^{-40} as limiting criteria.

2.4.2 Capacity loss

As stated in 2.1.1, the electronic tunneling barrier and probability could be further derived according to Equation (2.1) and (2.2). In our model, the electronic tunneling barrier was constant since both the work function and band gap are converged for the same SEI component. Thus, the electronic tunneling probability was a function that only depends on the thickness of SEI. Thus, the critical thickness of SEI, d^* , that blocks electron tunneling could be estimated from Equation (2.2) assuming a very small tunneling probability $T = e^{-40}$. The d^* values of each SEI component were listed in Table 2.1, and the order was $\text{LiF} > \text{Li}_3\text{PO}_4 > \text{Li}_2\text{CO}_3$ in both GGA and HSE06 methods. The d^* here ranged from 2.0~3.0 nm in GGA calculation and 1.6~2.1 in HSE06 calculation, due to the underestimation of band gaps in GGA calculation. Nevertheless, both results were still consistent with both the TEM images by Shim[163] and predicted thickness by Li[51]. In the design of coating layers for anode materials, there were always questions about what the coating materials should be and what thickness was sufficient. Based on the calculation, a ~2 nm LiF could totally block the electronic tunneling. Li_3PO_4 was also an excellent electrical insulating material, and ~2 nm Li_3PO_4 can also block electron tunneling. The thickness of Li_2CO_3 required to block electron tunneling was ~3 nm.

Based on the d^* values, the number of lithium ions consumed (N) during SEI formation per unit surface area of the anode can be further derived according to Equation (2.3). Moreover, the irreversible capacity loss (C_{ir}) due to SEI formation can be obtained through Equation (2.4). The results are also summarized in Table 2.1. What's more, the irreversible capacity loss scales linearly with the BET surface area of the electrode, at a slope indicated by the specific capacity loss C . The values of C from each SEI component are listed in Table 2.1. Interestingly, even though the critical thickness of LiF is smaller, the irreversible capacity loss due to LiF

formation is larger because the lithium-ion density in LiF is almost twice as much as that in Li_2CO_3 . It suggests that LiF is a more desirable insulating coating material when the initial capacity loss is not a concern while Li_2CO_3 may be preferred in naturally formed SEI since it causes less capacity loss. This may be difficult to achieve in batteries, since the complicated SEI compositional evolution may be closely related to the kinetics of formation of the different components during the SEI formation cycle.

Table 2.1 Calculated results of the tunneling effect in different SEI components. ρ was the number of lithium ions per unit volume in SEI component, Φ , represented the work function, E_g was the band gap (computed from GGA and HSE06), which led to different electronic tunneling barrier, ΔE_t , the critical thickness of SEI, d^* , and the specific capacity loss, C .

Component	Φ (eV)	ρ (\AA^{-3})	Based on GGA				Based on HSE06			
			E_g (eV)	ΔE_t (eV)	d^* (\AA)	C (%/(m^2/g))	E_g (eV)	ΔE_t (eV)	d^* (\AA)	C (%/(m^2/g))
Li_2CO_3	6.02	0.035	4.75	1.78	30.2	1.27	7.07	4.10	20.0	0.84
LiF	7.59	0.060	8.52	3.98	20.3	1.45	10.8	6.26	16.2	1.15
Li_3PO_4	5.24	0.037	5.68	3.49	21.6	0.96	8.1	5.91	16.6	0.74
Li	3.05	-	0	-	-	-	0	-	-	-

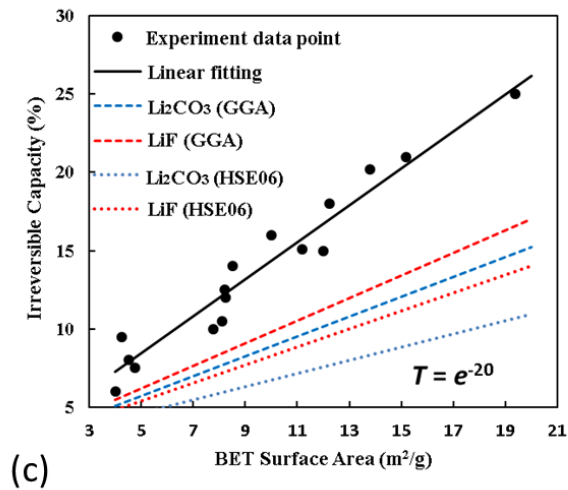
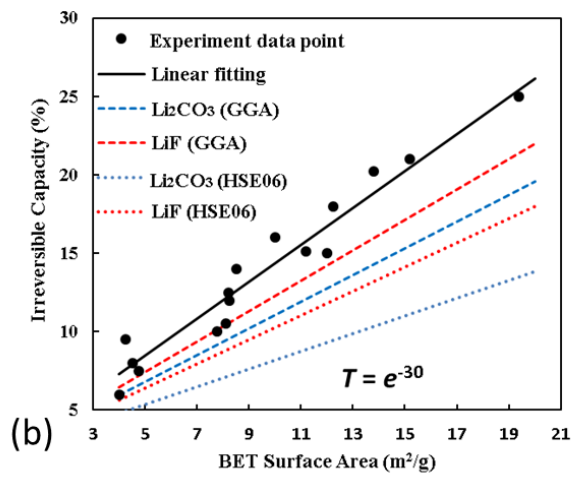
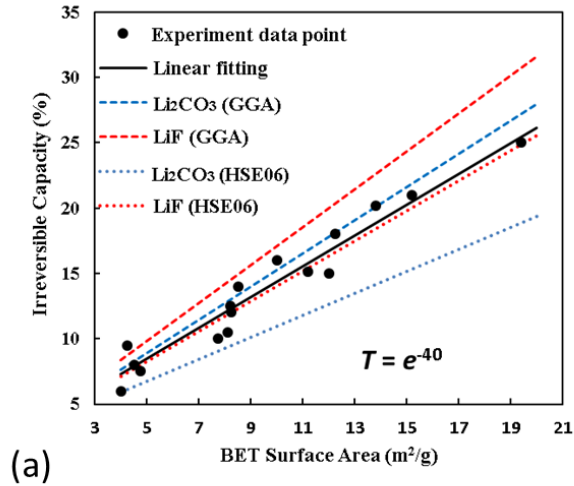


Figure 2.4 Predicted initial irreversible capacity loss due to SEI component formation assuming the electrons are completely blocked at a tunneling barrier T of e^{-40} (a), e^{-30} (b), and e^{-20} (c). The original experimental data points and linear fitting from Joho were also added for comparison [60].

A linear relationship between the first cycle irreversible capacity loss and the BET surface area was reported in Joho's experiments on various carbon electrodes [54]. As shown in Figure 2.4a, their experimental data suggested a linear relationship between the irreversible capacity loss and BET surface area, and the slope of the linear fitting is $C=1.18$. Other researches had shown that the active surface area and surface chemistry of anode also play an important role in addition to the total BET surface area in determining the irreversible capacity loss due to exfoliation of graphite during the first cycle[116][164][165]. Thus, the linear fitting of Joho's experimental data did not start from the origin and some data points deviate far from the fitting line at the small surface area. Considering this part of the irreversible capacity loss, four lines were further added to Figure 2.4a according to the predicted C values from different SEI components based on both GGA and HSE06 calculation, assuming an electrical insulating criterion of $T = e^{-40}$. To further investigate the influence of chosen T values, the same plotting process is repeated with the criterion of $T = e^{-30}$ and $T = e^{-20}$ in Figure 2.4b and 2.4c, respectively. The predicted values and the fitting trend line of the experimental data points in Figure 2.2a were in good agreement, although the simple model has only assumed one component while the naturally formed SEI is a mixture of Li_2CO_3 , LiF , Li_2O and some organic layers. However, in both Figure 2.4b and 2.4c, the predicted lines in both figures deviated from the linear fitting of experimental data points. Thus, the chosen electrical insulating criterion $T = e^{-40}$ is validated. The agreement suggests between predicted line and fitting trend line of experimental data points also suggest that the initial SEI thickness and its formation induced initial irreversible capacity loss are likely to be controlled by the self-limiting electron tunneling property of the inorganic components. This also means that the continuous growth of SEI is likely to be caused by other electron transport mechanisms, rather than tunneling.

2.4.3 Tunneling barrier change due to stress on SEI

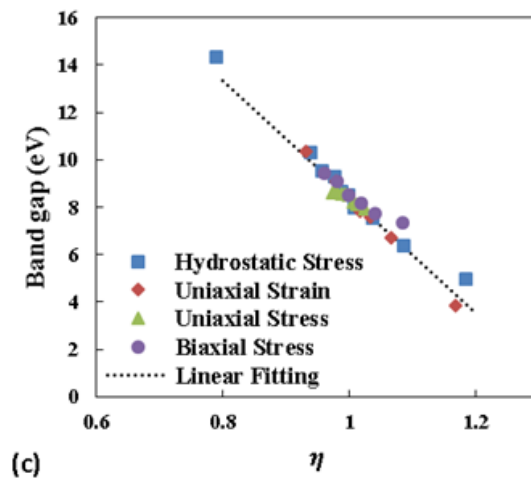
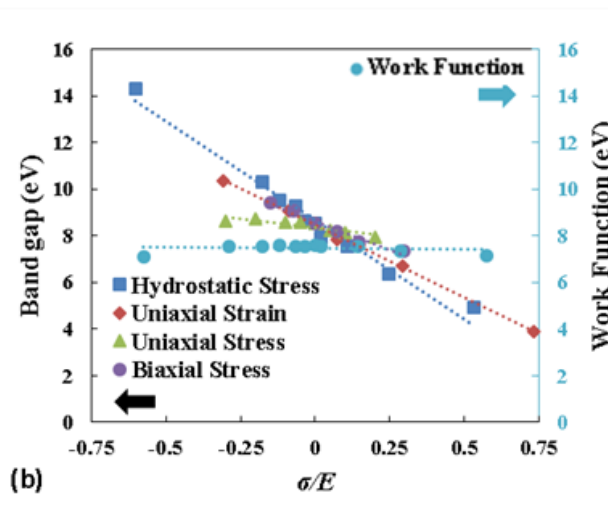
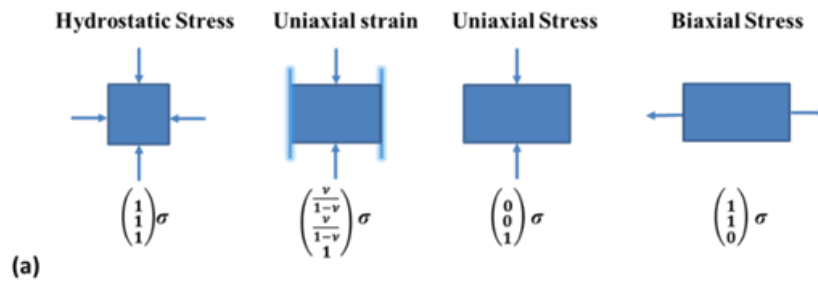


Figure 2.5 Schematic of the four loading methods (a), band gap and work function value as a function of σ/E (b) and η (c).

LiF was chosen to further investigate the influence of stress on the tunneling barrier. The calculated work function of 10 layers LiF slab model is shown in Figure 2.5a. It can be seen

that the change in work function due to stress is quite small. If we just consider the 10% volume change of graphite, the work function can be treated as a constant in this range. However, the band gap values are greatly influenced by deformation. The general trend shown in Figure 2.5a is that the band gap value (computed with GGA method) increases as the stress changes from tension side to the compression side. What is more, under each loading condition, the changes of band gap values are almost linear with respect to the strain (or the ratio between stress and Young's modulus, σ/E), as shown in the four trend lines in Figure 2.5a.

According to recent research [166], for ionic crystals where anions are localized, when lattice parameter increases, all bandwidths will shrink and energy states in both valence band and conduction band will increase. However, the shift of more localized valence band will be faster than that of the conduction band. Therefore, the band gap will shrink. This suggests that the distance between anions rather than the distance between anions and cations is the most important parameter, as the electrons are donated to anions. This motivates us to propose a new structure parameter, η , called normalized average anion distance:

$$\frac{1}{\eta} = \sum \frac{r_0}{r_i} \quad (2.6),$$

where r_0 and r are the equilibrium distance between the nearest anions in the perfect structure and deformed structure of LiF, respectively. When calculating the distance between anions, all the 12 nearest anions were included in the sum. η is computed from dimensionless stress (normalized by the Young's modulus) as $\varepsilon = \sigma/E$ for all four loading conditions. For a simpler representation, which demonstrates the connection η with strain in different direction, k and n were used to represent the ratio between the deformed lattice and the original lattice in specific directions in the strain tensor. The band gap value as a function of η is shown in Figure 2.5b, where η value higher than 1 represents tension while η less than 1 represents compression. Figure 2.5b clearly shows the band gap value decreases linearly with increasing

value of η , and all four loading conditions follow the same function. When the deformation is very large, the band gap values deviate from the linear relationship slightly. In these cases, some 2nd or 3rd nearest neighbor anions become very close to the center anion under large deformation, and should be included in the η calculation. Nevertheless, the normalized anions distance η is a newly proposed parameter to unify the lattice deformation in different loading conditions and the band gap decreases linearly with increasing η . Therefore, the electronic tunneling barrier will decrease under tension and increase under compression.

To further evaluate the effect of the stress on electron tunneling, we estimated the capacity loss of an SEI covered graphite which undergoes 10% volume expansion due to lithiation. First, the SEI formed on graphite is considered stress free. This is reasonable, as suggested by some recent research that the organic part of SEI is formed before lithiation while the inorganic part of SEI is formed simultaneously with lithiation [139][167]. It indicates an SEI film is almost stress-free perpendicular to the particle surface because the organic SEI layer is much softer compared with the inorganic layer. The inorganic layer of SEI will experience biaxial stress in the other two directions due to the volume expansion of the anode. Due to the 10% volume expansion of graphite, the overall thickness of SEI is reduced by 2.1% due to Poisson's ratio. If we only assume that the SEI should grow back to its original thickness in order to block the electrons tunneling, it will lead to 2.1% more irreversible capacity loss. However, the relationship between the band gap and η sheds new insight. According to it, the 10% volume expansion of graphite will lead to a 2.0 % increase in η . Thus, the band gap will decrease from 8.51 eV to 8.17 eV, leading to 0.34 eV reduction in the tunneling barrier. To achieve the same electronic tunneling probability, the thickness of SEI should increase by another 4.5%, leading to 11.0 % more irreversible capacity loss.

2.5 Conclusions

An electron tunneling model based on DFT calculations from a single component was made to characterize the electrical insulating mechanism of SEI. This simple model can provide a quantified prediction for the tunneling barrier, the critical thickness to block electron tunneling (2~3nm), and the irreversible capacity loss due to SEI formation. The agreement between the model and experiment suggests the initial irreversible capacity loss is likely due to the self-limiting electron tunneling property of the SEI. It suggests that LiF is a more desirable insulating coating material when the initial capacity loss is not a concern while Li₂CO₃ may be preferred in naturally formed SEI since it causes less capacity loss. Furthermore, how electronic tunneling barrier and probability change under stress under different types of loading conditions are also investigated. It was shown that the band gap decreases linearly with increasing value of η while the work function stays the same, where η is a new parameter to characterize the average distance between anions. That means the electron tunneling barrier decreases under tension and increases under compression.

3 Predicting open circuit voltage curves in Li-S battery depending on the solvation of Li-polysulfides

3.1 Summary

Most of the discharging curves for Li-S batteries showed either one plateau or two plateaus. Understanding the mechanism and conditions of the one-plateaued discharging curves can provide guidance for Li/S battery design to prevent the Li-polysulfide (Li-PS) dissolution. In this chapter, we first calculated a solvent-dependent open circuit voltage (OCV) using DFT when both crystals (S, Li_2S , Li) and dissolved Li-PS molecules (such as Li_2S_4) were involved in the discharging reactions. We successfully predicted the two-plateaued OCV with fully solvated Li-PS and the one-plateaued OCV with non-solvated Li-PS, in agreement with experimental observations.

3.2 Introduction

Li-S battery had been actively pursued as one of the next generation energy storage devices because of its higher specific capacity, specific energy density, and low cost [17][18]. The open circuit voltage (OCV) was a direct signature of the electrochemical reactions occurring inside a battery cell. Interestingly, most of the discharging curves for Li-S batteries showed either one plateau or two plateaus. The two-plateaued discharging curves were typically observed in Li-S batteries with an ether-based liquid electrolyte [63][64]. The first plateau at 2.3~2.4 V has been attributed to the lithiation reaction from elemental S to dissolved Li-polysulfide (Li-PS). The second plateau at around 2.0~2.1 V has been attributed to the continuous lithiation of the dissolved Li-PS to the precipitated crystalline Li_2S_2 and Li_2S . In comparison, the single sloped discharging plateau around 2.0 V was believed to be the characteristic for the Li-S batteries with solid electrolytes due to the direct transformation from elemental S to solid state Li_2S_2 and Li_2S , while Li-PS was not formed due to the absence of free solvent in electrolytes [65][66].

However, more interestingly, some Li-S batteries with carbonate-based liquid electrolytes also displayed one-plateaued discharging curves [79]. This unique phenomenon was generally observed when S was confined in the nanopores of a carbon matrix in the S-C cathode materials and sealed by in-situ formed solid electrolyte interphase [169–171]. So far, there is no consistent model that has clarified the difference between the two-plateaued and one-plateaued OCVs from the reaction mechanisms point of view.

It is important to understand the mechanism and the conditions for the one-plateaued discharging curve, as the two-plateaued discharging curve is the signature for the Li-PS shuttling problem. The Li-PS dissolved in the electrolyte can facilitate a shuttle reaction between anode and cathode, and precipitate as the insulating and insoluble Li_2S_2 and Li_2S on the surface of the anode, leading to severe capacity loss, due to the loss of active S and blocked electronic pathway [22]. When only one-plateau was observed in the carbonate-based liquid electrolyte with nanopore-S-C cathode materials, the battery cycling performance was greatly improved due to the absence of Li-PS [69,71,170–174]. The confinement and separation mechanism has been proposed to explain this unique phenomenon. In the confinement mechanism, it was hypothesized that the pore volume was too small to store S_8 monomer and long chain Li-PS [36,67,68]. Thus, the small S allotropes such as S_2 and S_4 were incorporated into the pores and long chain Li-PS such as Li_2S_8 , Li_2S_6 , and Li_2S_4 could not be generated in the discharging reaction due to the confinement of nanopores. In addition, the formation of SEI from the decomposition of carbonate electrolytes can seal the pore blocking the electrolytes from diffusing into the pores [69]. In ether electrolytes with less SEI formation, if the pore size was well controlled to only allow Li-ion diffusion while blocking both Li-PS and electrolyte solvent, there would be a great chance to entrap the Li-PS inside the pores [69][70]. However, the pore size of porous carbon is in 3~5 nm, which was already much larger than the solvent molecule and soluble Li-PS, a carbonate electrolyte [8], [21-22] or carbonate solvent

[20] has to be used to seal the pores through the formation of SEI. Besides the nanopore structure, the plateaus on the discharging curves were also related to the chemistry of electrolyte solvent [175]. A single plateau was observed when electrolyte solvent with low Li-PS solubility was used, while two plateaus were observed with an electrolyte that could dissolve more Li-PS [74]. Further, the concentrated electrolyte can also mitigate the Li-PS shuttle problem [75–78]. Therefore, the OCV is highly dependent on the solvation status of the Li-PS, which is subject to change with the pore size, solvent chemistry, electrolyte concentration, and temperature.

Challenges exist to calculate the temperature and solvent dependent OCV using first principle calculations. DFT has long been used to predict the OCV of electrodes that store lithium via intercalation [80][81] and alloying [82][83] solid-state reactions. In fact, if the lithiation reaction of S was modeled as a solid-state reaction, Li_2S would be the only thermodynamically stable phase, consistent with the Li-S phase diagram [86]. Using crystalline S and Li_2S , Yang *et.al* computed the convex hull of all crystalline Li-PS (without solvation due to periodic boundary conditions) with plane-wave DFT. It was found that all long-chain Li-PS were unstable as they lie above the tie-line between S and Li_2S [84]. Thus, only one plateau in the discharging curves should be expected. With the same plane-wave DFT method, B. Wang *et.al* [176] showed the discharging reaction path was altered depending on whether the structure of S (represented as S_8 monomer), Li-PS and Li_2S were modeled as monomers or clusters in a vacuum, both are different from what was calculated by treating Li-PS as crystal structures [32]. L. Wang *et.al* [85] first added the temperature effect due to vibrations and the solvation effect, modeled by polarizable continuum model (PCM), to compute the free energy with local-basis set DFT implemented in Gaussian. Their predicted OCV showed several plateaus. By changing Li, Li_2S , Li-PS from monomer to cluster structures while maintaining the monomer structure of S_8 , the predicted OCV curves showed multiple plateaus within the similar voltage

range with experimental observation. It is, therefore, reasonable to treat Li-PS as either monomers or clusters [177–179]. However, Li_2S and S should not be treated as dissolved monomer or clusters, as they have very low solubility in the electrolyte. Furthermore, according to Canepa et.al, [180] the calculated solvation energy based on different solvation models might be inconsistent. Including the solvation effect appropriately in the Li-PS system remains another computational challenge. Therefore, a systematic investigation of the influence of the solvation effects at finite temperature on the prediction of OCV is required and important.

In the present work, the temperature and solvation effects were added to DFT calculations in order to capture their influence on the OCV profile. The structures used in the model were selected to better mimic the Li-S battery system, Li, S, and Li_2S were treated as crystal structures due to their low solubility in the electrolyte and the smallest soluble Li-PS, Li_2S_4 was treated as molecules and clusters. The reason to skip other Li-PS species, such as Li_2S_8 , and Li_2S_6 , and arguably Li_2S_7 or Li_2S_5 [177][178], in our calculations, is that only one plateau at 2.3~2.4 V was seen in most experiment. That means the OCVs ascribed to the transformation from the crystal S to various Li-PS species will fall into a very narrow energy range, which can be represented by the direct transformation from S to Li_2S_4 . The S_3 radical recently observed by Q. Wang et.al [181] was not included in our calculation since it mainly serves as a reaction intermedia and will not change the reaction energies that lead to the OCV curve. Experimentally, mixed electrolyte solvent of dimethoxyethane (DME) and dioxolane (DOL) is often used in Li-S battery. B. Wang *et.al* [176] suggested that DOL provided slight larger binding energy to Li-PS than DME. Therefore, DOL was chosen as the electrolyte solvent in our model. The energies of Li_2S_4 dissolved in liquid DOL electrolyte were calculated with different solvation models and the subsequent OCVs from these solvation models were compared with the experimental observations in order to determine which model is more appropriate. This comparison also revealed that the origin of the one-plateaued or two-plateaued discharging curves is due to the

solvation of the Li-PS.

3.3 Model details

3.3.1 OCV and formation energy calculations

The average OCV for a typical lithiation reaction



with reference to Li-metal as 0 V is defined as

$$\langle OCV \rangle = \frac{-\Delta G}{\Delta x e} = \frac{-[G(Li_{x_2}X) - G(Li_{x_1}X) - (x_2 - x_1)G(Li)]}{(x_2 - x_1)e} \quad (3.2),$$

where ΔG is the change of Gibbs free energy in reaction (3.1), Δx is the transferred number of electrons, and e is the charge on one electron. $G(Li_{x_2}X)$, $G(Li_{x_1}X)$ and $G(Li)$ are the Gibbs free energy of phase $Li_{x_1}X$, $Li_{x_2}X$, and Li-metal, respectively. Here, we consider the reaction from S (crystal) $\rightarrow \frac{1}{4}Li_2S_4$ (molecule) $\rightarrow Li_2S$ (crystal). The crystal structure of Li, S, and Li_2S were obtained from Materials Project [182]. To determine whether the molecular Li_2S_4 with solvation would be thermodynamically stable, its formation energy with respect to the crystalline S and Li_2S was calculated as

$$G_{form}\left(\frac{1}{4}Li_2S_4\right) = \frac{1}{4}G(Li_2S_4) - \frac{3}{4}G(S) - \frac{1}{4}G(Li_2S) \quad (3.3).$$

A positive $G_{form}\left(\frac{1}{4}Li_2S_4\right)$ means that the formation of Li_2S_4 is not thermodynamically favorable. Thus one step discharging reaction from S crystal to Li_2S crystal, corresponding to the one-plateaued OCV, will be expected. On the other hand, if $G_{form}\left(\frac{1}{4}Li_2S_4\right)$ is negative, the formed Li_2S_4 will participate in the two-step discharging reaction and result in a two-plateaued OCV.

For crystalline phases, such as Li, S, and Li_2S , the temperature dependent terms in Gibbs

free energy include only the vibration contribution:

$$G(Li_xX_{crystal}) = E_{DFT}(crystal) + E_{vib}(T) - TS_{vib}(T) \quad (3.4).$$

For the dissolved molecular, specifically Li_2S_4 in DOL, the Gibbs free energy includes the solvation energy and the temperature dependent contributions of translation, rotation, vibration, of the molecule,

$$G(Li_xX_{solv}) = E_{DFT}(gas) + [E_{vib}(T) - TS_{vib}(T)] + [E_{rot}(T) - TS_{rot}(T)] + [E_{tra}(T) - TS_{tra}(T)] + E_{solv} \quad (3.5).$$

In equation (3.4) and (3.5), $E_{DFT}(crystal)$ and $E_{DFT}(gas)$ are the DFT minimized energy of crystals and molecules at 0K. E_{vib} , E_{rot} and E_{tra} are the vibrational, rotational and translational enthalpy corrections, while S_{vib} , S_{rot} and S_{tra} are the vibrational, rotational and translational entropy. E_{solv} is the solvation energy, calculated from different solvation models detailed in Section 3.2.2.

Because the plane-wave DFT is more efficient for crystals and the local-basis set DFT is the typical choice for molecule and cluster calculations, both were applied to the structures they are suitable for. Comparisons were made to several special cases (crystalline Li, Li_2S , S, and cluster solvation model) for validation purpose. Specifically, spin-polarized, all-electron, local basis set (Double Numerical plus polarization, DNP [183]) DFT implemented in Dmol³ [184] in Materials Studio was used. The exchange-correlation was treated with the generalized gradient approximation (GGA) Perdew-Wang-91 functional [185]. To capture the temperature effect, the contributions from vibration, rotation, and translation were calculated through vibrational analysis by finite differences of analytic gradients, based on the detailed formula from Hirano's work [186]. Only the ion positions were relaxed during an energy minimization, until one of the three convergence criteria, as 3×10^{-4} eV/system, 0.05 eV/Å, and 0.005 Å for energy change, force, and displacement, respectively, was reached. For comparison, the energy

of the Dmol³ minimized structures were recalculated with the plane-wave DFT implemented in the Vienna ab initio simulation package (VASP). Potentials constructed with the full potential projector augmented wave (PAW) method were used for the elemental constituents [187]. The exchange-correlation was treated with the GGA Perdew-Burke-Ernzerhof (PBE) functional [188]. The cutoff energies and K-points used were as follows: 700 eV and $2 \times 2 \times 2$ for S₈ crystal, 600 eV and $6 \times 6 \times 6$ for Li₂S crystal, 650 eV and $12 \times 52 \times 52$ for Li crystal, 700 eV and $1 \times 1 \times 1$ for all liquid structures.

3.3.2 Solvation energy calculations

The solvation energy is the energy associated with dissolving an isolated solute molecule (gas phase) in a solvent to form the solution, which can be calculated as

$$E_{solv} = E[solution] - E[solvent] - E[solute(iso)] \quad (3.6).$$

Different solvation models, namely explicit model[189], implicit model[190][191], cluster model[192–194], and combined model[180] are often used in computing solvation energies. In the explicit model, both the solution and the solvent are modeled with full atomistic liquid structures, at the corresponding concentration and density [195][196]. $E[solution]$ and $E[solvent]$ are the average energy obtained from MD or Monte Carlo (MC) simulations. In the implicit model, a single solute molecule embedded in a dielectric continuum media is used to represent the solution. The solute and the solvent interaction can be calculated via the conductor-like screening model (COSMO) [190] or the polarizable continuum model (PCM) [191]. The error for implicit solvation models depends on the dielectric constant, ϵ [197]. The cluster model can be considered as a simplified explicit model, by considering only the first solvation shell [193] [194], which can be extracted from liquid structure via MD simulations. Then $E[solution]$ and $E[solvent]$ are the energy of the first solvation shell and the solvent molecule in a vacuum, respectively. In the combined model, the first solvation shell is

embedded in a dielectric continuum [180], to obtain $E[\textit{solution}]$ with COSMO or PCM model. $E[\textit{solvent}]$ is the energy of a solvent molecule embedded in the dielectric continuum. Comparing these models, the explicit model represents the liquid structure and dynamics properly, but its accuracy is often sacrificed by using classic force for larger simulation cells. To be more accurate, *ab initio* MD can be used, but with a smaller structure and a shorter time. DFT method is often used for cluster model, implicit model, and the combined model with DFT method. Considering the cluster model ignores the solvation shell and solvent interaction, the combined model provides a combination of the implicit and cluster model.

In this paper, the solvation energies calculated from these models will be compared. The energetic terms in the explicit model, namely $E[\textit{solution}]$, $E[\textit{solvent}]$ and $E[\textit{solute(iso)}]$, were all calculated through VASP as stated in section 2.1. In the implicit model and combined model, the energetic terms were calculated through Dmol³ with COSMO solvation model, [190] in which the solvent was treated as a continuum with a permittivity $\epsilon=7.2$ for DOL electrolyte[198]. In the cluster model, the energetic terms were calculated in both methods for validation purpose.

To sample more configurations and save simulation time, classical MD and AIMD were used to prepare the input structures for the DFT minimizations. While the lowest optimized energies were chosen to calculate the solvation energy, while several configurations were used to indicate the fluctuation.

The first solvation shell structure is important for the cluster model and the combined model. The structure of the first solvation shell for a fully solvated Li₂S₄ was obtained from a dilute solution of randomly packed Li₂S₄ and DOL molecules at a ratio of 1:100 simulated by classical MD. The force field types within the compass force field [199] of each atom type chosen are as following: li+ (1.0) for Li, h1 (0.053) for H, o2e (-0.32) for O, s (-0.73) for S at the end, s2s (-0.27) for S in the middle, c4o (0.054) for C with two C-O bond, c4o (0.214) for

C with only one C-O bond. The optimized cell was subject to a classical MD simulation with NPT ensemble, with Nosé algorithm [200] and Berendsen algorithm [201] to control the temperature at 298K and pressure at 1 atm for 50 ps with a time step of 1 fs. The converged solution density, calculated as the average density of the last 20 ps, was $1.06 \pm 0.011 \text{ g/cm}^3$. The first solvation shell structure was determined as $\text{Li}_2\text{S}_4 \cdot 4\text{DOL}$ by analyzing the radial distribution function (RDF) and the coordination number (CN) around the Li_2S_4 in the MD trajectory. At last, the first solvation shell $\text{Li}_2\text{S}_4 \cdot 4\text{DOL}$ was extracted from the three configurations with the lowest potential energy in the MD simulation to be the initial configuration for geometry optimization in DFT calculations.

To represent the fully solvated solution structure in the explicit model, 1 Li_2S_4 molecule and 20 DOL molecules were packed into the periodic simulation cell with an initial density of 1.06 g/cm^3 . The converged density was $1.19 \pm 0.015 \text{ g/cm}^3$ based on classical NPT MD simulation. This density was 12% higher than the solution with a Li_2S_4 : DOL ratio of 1:100, indicating that this solution deviated from the ideal dilute solution. To better describe the solvent-solute interaction, *ab initio* MD (AIMD) implemented in VASP with NVT ensemble at a timestep of 1 fs was performed for 1.5 ps at 300K. The average potential energy during the last 1 ps AIMD simulation were both recorded to obtain the solvation energy and estimate its fluctuation. Three configurations with the lowest potential energy from AIMD simulations was used as the initial configuration for geometry optimization in DFT calculations.

Non-solvated Li_2S_4 was first simulated as a monomer (isolated molecule). Five different configurations of isolated Li_2S_4 were optimized in DFT calculation. The optimized structure with the lowest energy was chosen to represent the Li_2S_4 monomer. Since non-solvated Li_2S_4 can agglomerate into clusters, Li_2S_4 molecules were arranged under different configurations as $(\text{Li}_2\text{S}_4)_n$ cluster. The initial configuration of larger clusters was built based on the optimized configuration of smaller clusters.

3.4 Results

3.4.1 Temperature effect in crystalline phases

The calculated energy contributions for all species at both 0 K and 300 K are listed in Table 3.1. At 0 K and 300 K, the vibrational contributions, namely $E_{vib}(T) - TS_{vib}(T)$, for crystalline S, Li, and Li₂S, were all less than 0.05 eV. These small vibrational contributions confirmed the typical assumption that the temperature effect for crystals can be neglected in the calculation of the OCV in equation (3.2) and the relative formation energy (ΔG_{form}) in equation (3.3). The OCV of the direct reaction of $2\text{Li} + \text{S} = \text{Li}_2\text{S}$ was 2.13 V at 0 K and 2.10 V at 300 K. This confirmed that for OCV calculations in solid, the $T\Delta S$ term in equation (3.4) was often dropped, as it is relatively much smaller than ΔE at room temperatures for solids [202]. The calculated OCV at 0 K from VASP is 2.04 V. The difference between Dmol3 and VASP method was less than 0.1V, suggesting the results from the two methods can be combined and compared. All of the computed OCV values are in good agreement with most experiments in all solid-state Li-S battery[65][66].

3.4.2 Temperature effect for non-solvated Li₂S₄

However, the temperature effect became significant for molecular Li₂S₄. The optimized geometry of a non-solvated Li₂S₄ monomer is shown in Figure 3.1a. According to Table 3.1, the vibrational contribution at 0 K or the zero-point energy (ZPE) is 0.24 eV. At 300K, the free energy contributed from the vibration, rotation, and translation is up to -0.67 eV per Li₂S₄ molecule.

The relative formation energy of Li₂S₄ in the gas phase obtained through equation (3) was 0.52 eV at 0K and 0.33 eV at 300 K. It was observed in the experiment that Li₂S₄ molecules may dynamically aggregate into clusters even at a low concentration of 0.2 M [30]. Therefore, the Gibbs free energy per formula Li₂S₄, $G_{DFT}(\text{Li}_2\text{S}_4)_n/n$, was plotted as a function of cluster

size n in Figure 3.1c. For comparison, the Gibbs free energy of Li_2S_4 monomer is shifted to 0. The optimized Gibbs free energy related to different initial configurations were shown as data points. For the monomer, all different initial configuration relax into one configuration. The energy for the dimers showed large dependence on the initial configurations. The larger clusters built upon the lowest energy dimers showed less fluctuation in optimized energy. The lowest energies clearly showed that $G_{DFT}(\text{Li}_2\text{S}_4)_n/n$ decreased with increasing cluster size till it converged within 0.05 eV when n is larger than 6. Therefore, the optimized structure of $(\text{Li}_2\text{S}_4)_8$ cluster, as shown in Figure 3.1b, was chosen to represent the Li_2S_4 cluster in a vacuum. The difference between Gibbs free energy at 0K and 300K also dropped from 1eV to 0.4eV with increasing cluster size. These results suggest that the temperature effect on free energy cannot be ignored for the Li_2S_4 molecule or clusters.

Table 3.1 List of free energy terms for all species (Unit: eV). E_{DFT} is calculated with basis set DFT in Dmol3. E_{vib} , S_{vib} , E_{rot} , S_{rot} , E_{tra} , S_{tra} are obtained through vibrational analysis. For the solvation model in the method part, E, Cl, I and Cm stands for explicit model, cluster model, implicit model, and combined model, respectively. For the calculation method, D stands for calculations with Dmol3 and V stands for calculations with VASP.

Structure	T/K	E_{DFT}	E_{vib}	$-TS_{vib}$	E_{rot}	$-TS_{rot}$	E_{tra}	$-TS_{tra}$	E_{solv}	Method	G(T)		
S (crystal S_8)	0	-4.114	-	-	-	-	-	-	0	-	V	-4.114	
	0	-10835.577	0.040	0	0	0	0	0			D	-10835.538	
	300	-10835.577	0.085	-0.112	0	0	0	0			D	-10835.605	
S (monomer S_8)	0	-10835.560	0.039	0	0	0	0	0	0	-	D	-10835.521	
	300	-10835.560	0.034	-0.054	0.005	-0.052	0.005	-0.069			D	-10835.692	
Li_2S_4 (monomer)	0	-22.443	-	-	-	-	-	-	0	-	V	-22.443	
	0	-43754.542	0.244	0	0	0	0	0			D	-43754.298	
	300	-43754.542	0.375	-0.219	0.038	-0.369	0.038	-0.530				-43755.207	
Non-solvated Li_2S_4 (Li_2S_4) ₈	0	-43755.557	0.255	0	0	0	0	0	0	-	D	-43755.302	
	300	-43755.557	0.255	-0.537	0.005	-0.680	0.005	-0.076				-43755.726	
Fully-solvated Li_2S_4 $Li_2S_4 \cdot 20DOL$ $Li_2S_4 \cdot 4DOL$	0	-22.443	-	-	-	-	-	-	-1.915	E	V	-24.358	
	0	-22.443	-	-	-	-	-	-	-2.053	Cl	V	-24.496	
	0	-43754.542	0.244	0	0	0	0	0	0	-0.795	I	D	-43755.093
										-2.279	Cl		-43756.577
										-2.165	Cm		-43756.463
	300	-43754.542	0.363	-0.253	0.038	-0.370	0.038	-0.530	-0.795	I	-43756.049		
			0.375	-0.219	0.038	-0.369	0.038	-0.530	-2.279	Cl	-43757.486		
0.375			-0.219	0.038	-0.369	0.038	-0.530	-2.165	Cm	-43757.372			
Li_2S (crystal)	0	-11.996	-	-	-	-	-	-	0	-	V		11.996
	0	-11249.791	0.133	0	0	0	0	0			D	-11249.657	
	300		0.191	-0.088	0	0	0	0				-11249.688	
Li (crystal)	0	-1.901	-	-	-	-	-	-	0	-	V	-1.901	
	0	-204.964	0.032	0	0	0	0	0			D	-204.932	
	300		0.047	-0.024	0	0	0	0				-204.941	

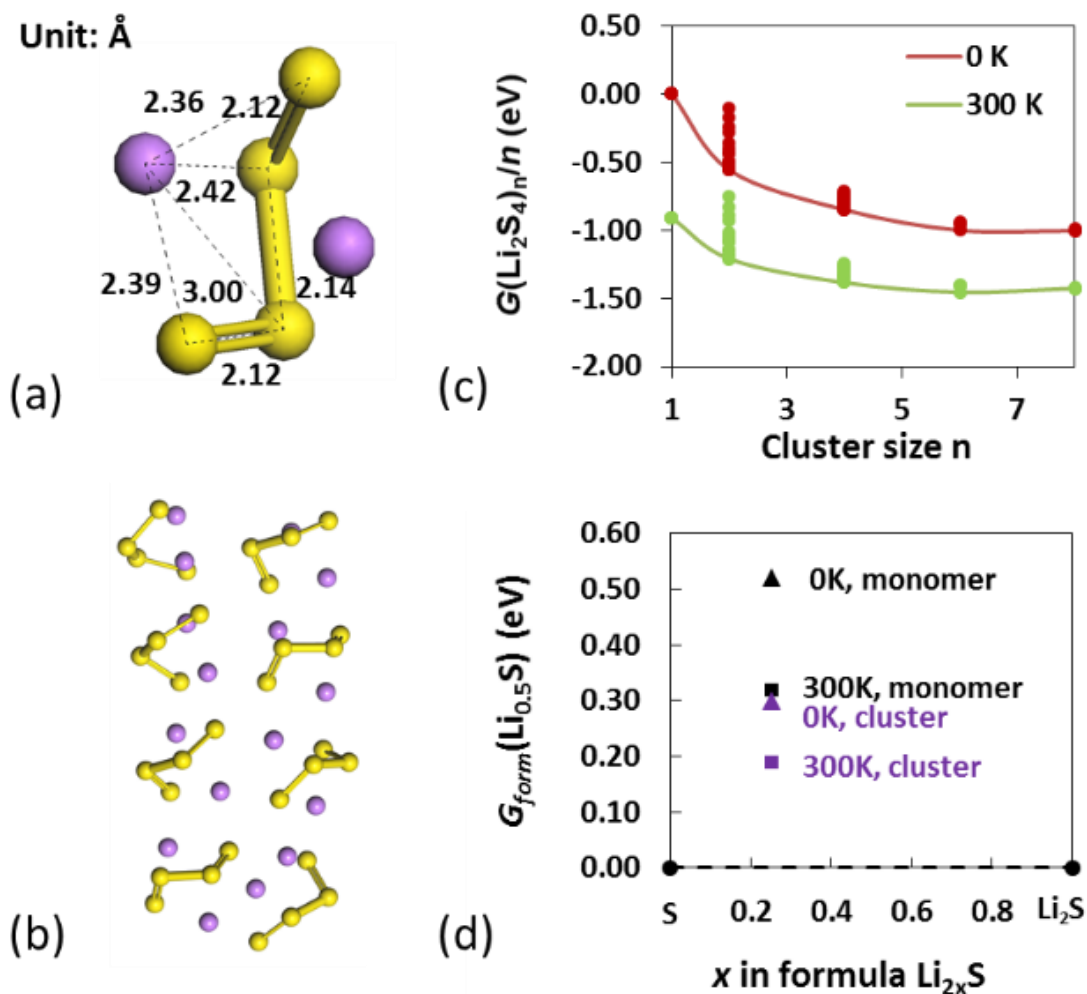


Figure 3.1 The structures and formation energies of non-solvated Li_2S_4 . The optimized structure of (a) Li_2S_4 monomer and (b) $(\text{Li}_2\text{S}_4)_8$ cluster. Li and S atom are represented by purple and yellow, respectively. The distance of S-S and S-Li bonds are labeled for Li_2S_4 . (c) The calculated Gibbs free energy of Li_2S_4 as a function of cluster size n . The data points represent different configurations. (d) The predicted relative formation energy of non-solvated Li_2S_4 with respect to the crystalline S and Li_2S .

Figure 3.1d plotted the relative formation energies of non-solvated Li_2S_4 with respect to a tie line between the crystalline S and Li_2S . As discussed, the temperature effect (from 0 K to 300 K) on the Gibbs free energy of crystal S and Li_2S was negligible and thus the position of the tie line can be treated as a constant. The relative formation energy of the non-solvated Li_2S_4 cluster was therefore 0.30 eV at 0 K and 0.19 eV at 300 K. No matter a monomer or a cluster

was used to represent non-solvated Li_2S_4 , the relative formation energy stayed positive without the solvent. Consequently, a one-plateaued discharging curve was expected without the formation of non-solvated Li_2S_4 .

3.4.3 Temperature and solvation effect for fully solvated Li_2S_4

Before the solvation energy calculation for the Li_2S_4 molecule in DOL solvent, a test calculation was first conducted for Li-ion in ethylene carbonate (EC) solvent ($\epsilon = 70$), which is more polarized than DOL solvent. With a first solvation shell of $\text{Li}\cdot 5\text{EC}$, our calculated solvation energy was 5.4 eV from the cluster model and 5.5 eV from the combined model. This value agreed well with the previous calculation with the cluster model [193,194] and explicit model [189]. However, the calculated solvation energy from the implicit model was only 4.4 eV, which was underestimated by 1.0 eV. It was also worth mentioning that the free energy contributed from the vibration, rotation, and translation change only slightly with the solvation models. As shown in table 3.1, while the sum of these contributions was -0.67 eV for non-solvated Li_2S_4 monomer and -0.71 eV for the fully solvated Li_2S_4 in the implicit model. Therefore, these contributions were taken from the isolated molecule in equation (3.5).

For the cluster model and combined model, the first solvation shell of $\text{Li}_2\text{S}_4\cdot 4\text{DOL}$ (Figure 3.2a) was extracted based on classical MD simulations of with 1 Li_2S_4 in 100 DOL by analyzing the RDF and the CN around the Li_2S_4 . Figure 3.2b shows the cumulative CN as a function of the cutoff distance for the Li-O distance. The two CN steps mean that each Li^+ in the Li_2S_4 coordinated with 2 DOL molecules via Li-O ionic bond at $\sim 2 \text{ \AA}$, and the second nearest Li-O neighbors were $\sim 4 \text{ \AA}$ away. To further differentiate the Li-S bonds, the two S atoms at the end of S_4^{2-} anion were defined as S (end) and the two S atoms in the middle were defined as S (mid). Each Li^+ in the Li_2S_4 also formed ionic bonds with the two S (end) at $\sim 2.4 \text{ \AA}$. Thus, the first solvation shell was $\text{Li}_2\text{S}_4\cdot 4\text{DOL}$, in which each Li at the end of Li_2S_4 was coordinated to 2 O atoms from two different DOL molecules at a distance around 2 \AA .

The smaller liquid solution model (shown in Fig 3.2c) used to facilitate AIMD calculations has 1 Li_2S_4 and 20 DOL molecules. The highlighted first solvation shell around the Li_2S_4 is highlighted in Figure 3.2c and its cumulative CN is shown in Figure 3.2d, which had exactly the same first nearest neighbor bonding and CN as that from the larger liquid cell shown in Figure 3.2b, except the Li-O CN kept increasing after 4 Å. This suggests that the first solvation shell was consistent with the large cells but the second solvation shell was not fully formed in the smaller liquid cell.

Table 3.2 compared the four different solvation models utilized to calculate the solvation energy for a fully solvated Li_2S_4 molecule. At 300 K, the Gibbs free energy of the fully solvated Li_2S_4 monomer, regardless the solvation model, was lower than that of the non-solvated $(\text{Li}_2\text{S}_4)_8$ cluster, suggesting that formation of clusters of Li_2S_4 in dilute solution was not energetically favorable, although it was reported that they dynamically exist [30] in the electrolyte or energetically favorable on the Li anode surface [203]. Thus, only a solvated monomer of Li_2S_4 was considered further to mimic the solvated Li-PS.

The solvation energy calculated by the implicit model was only -0.80 eV, much smaller than that calculated by the other three models, falling into the range of -2.09 ± 0.18 eV. In the cluster model, a difference of 0.22 eV in the solvation energy calculated by VASP and Dmol3 was also observed. This difference is within the same level of the deviation caused by different solvation models, except the implicit model.

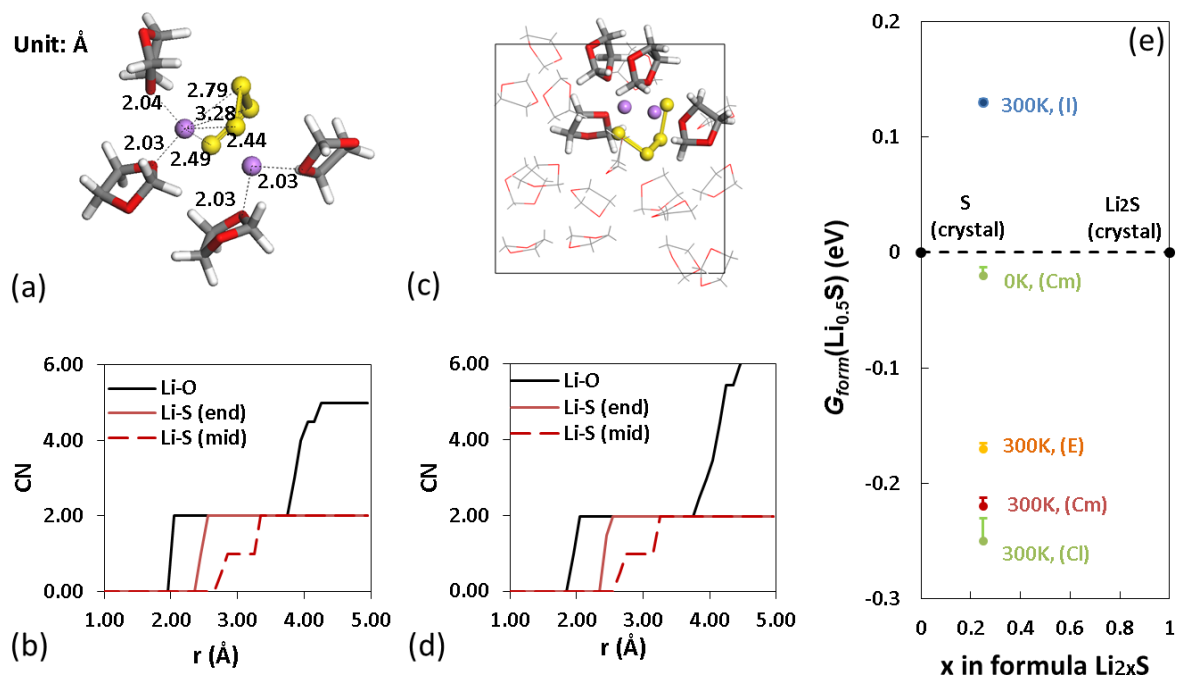


Figure 3.2 The solvation structure and energy for fully solvated Li_2S_4 monomer. Cumulative CN as a function of cutoff radius (a) and optimized geometry (b) of $\text{Li}_2\text{S}_4 \cdot 4\text{DOL}$ solvation shell with the dielectric continuum. The difference between the optimized geometry with and without dielectric continuum can be neglect. The Li, S, C, O, and H are represented as purple, yellow, grey, red and white, respectively. The distance of Li-S and Li-O are labeled. Cumulative CN as a function of cutoff radius (c) and optimized geometry (d) of $\text{Li}_2\text{S}_4 \cdot 20\text{DOL}$ after 0.5 ps ab initio NVT simulation. The relative formation energy of Li_2S_4 monomer under fully solvation status at 0 K and 300 K compared with crystalline S and Li_2S (e). The solvation energy is calculated with the implicit, cluster, combined and explicit models, which is labeled as (I), (CI), (Cm) and (E). The energy of crystalline S and Li_2S are already shifted to 0 for easy comparison. The error bar indicates the results from the different initial configuration.

Table 3.2 E_{solv} for the fully solvated Li_2S_4 in DOL solvent calculated by different solvation models (Unit: eV). The fluctuations are due to different configurations in the sampling scheme.

			Implicit Model	Explicit Model	Cluster Model	Combined Model
Fully solvated	Dmol3		-0.80 [+0.01]		-2.27 [+0.08]	-2.16 [+0.03]
	VASP	Min		-1.91 [+0.02]	-2.05	

Figure 3.2e showed the relative formation energy of the fully solvated Li_2S_4 monomer predicted by different solvation models. The cluster model, explicit model, and the combined

model all predicted negative relative formation energies for the fully solvated Li_2S_4 at 300K, within a range from -0.17 eV to -0.25 eV. This suggests that the fully solvated Li_2S_4 is a thermodynamically stable product in the discharging reaction. As a result, two-plateaued OCV is expected. This is in agreement with most experiment observation in typical Li-S batteries with liquid electrolytes [63][64]. The solvation energy deviation of ± 0.18 eV due to different solvation models and calculation methods only causes less than ± 0.1 V shift of the discharging plateaus, deemed to be acceptable. On the other hand, the positive relative formation energy predicted by the implicit model at 300 K (0.13 eV) leads to an inaccurate conclusion, that the fully solvated Li_2S_4 is not thermodynamically stable, which is against the experimental observations. Thus, the implicit solvation model is not appropriate for the solvation energy calculation of Li_2S_4 in DOL solvent.

Figure 3.2e also showed the temperature effect on the relative formation energy of the fully solvated Li_2S_4 monomer. The relative formation energy was only -0.02 eV at 0 K (considering the solvation energy with the combined model and the ZPE). The slightly negative value indicated the two discharging plateaus would be very close, almost overlapping, on the OCV. This was significantly different from that at 300K. Thus, the temperature effect could not be neglected for the OCV calculations involving dissolved molecules. It also suggested that the voltage difference on OCV decreases with temperature, which might be helpful to mitigate Li-PS desolvation problem.

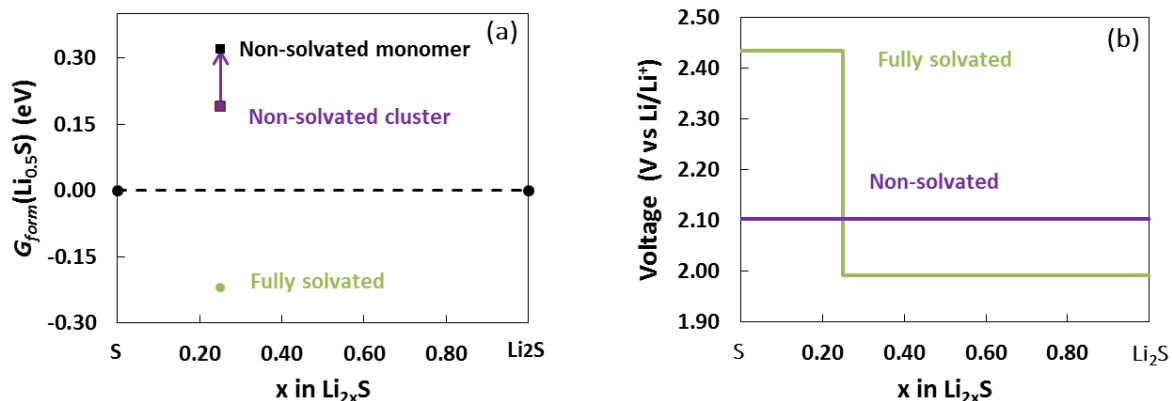


Figure 3.3 The calculated (a) relative formation energies and (b) the corresponding OCVs for non-solvated Li_2S_4 at 300K. The energy of crystalline S and Li_2S are already shifted to 0 for easy comparison in (a).

3.4.4 Predicted OCV curve

The relative formation energies at 300K for the fully solvated Li_2S_4 and non-solvated Li_2S_4 are summarized in Figure 3.3a. The solvation energy for the fully solvated Li_2S_4 was represented as the average value of -2.09 eV from the cluster model, combined model and explicit model shown in Table 3.2. The non-solvated Li_2S_4 was represented as an isolated Li_2S_4 monomer and isolated $(Li_2S_4)_8$ cluster, separately. The predicted OCVs at 300K are also shown in Figure 3.3b.

The one-plateaued OCV was predicted for non-solvated Li_2S_4 . The discharging plateau, attributed to the single step discharging reaction $2Li + S = Li_2S$, was 2.105 V. This is in good agreement with most experiment in all solid-state Li-S batteries [5][6]. The two-plateaued OCV was predicted for fully solvated Li_2S_4 . The voltages of the two plateaus predicted to be 2.43 V and 1.99, were in agreement with the experimental observation in general Li-S battery with liquid electrolyte without any special design[3][4]. As Li_2S_4 is fully solvated in the electrolyte, it is subject to severe Li-PS shuttle problem.

3.5 Conclusions

In summary, we have devised a method based on DFT calculations to predict the

temperature and solvent dependent OCV when both crystals (S, Li_2S , Li) and dissolved molecules (Li-PS, such as Li_2S_4) are involved in the discharging reaction. The energies of S, Li_2S , Li crystal, and Li_2S_4 molecule were successfully calculated and combined with consistent results from plane-wave DFT and basis set DFT. The temperature and solvation effect on the predicted free energy and the open circuit voltage (OCV) curves for Li-S batteries were systematically investigated. It was also shown that while the effect of temperature was negligible for predicting OCV curves associated only with solid-phase transformation, it played a deterministic role in the free energy of dissolved molecules, such as Li-PS. The consistency in the solvation structure and solvation energy in different models confirmed that the solvation effect is estimated appropriately. With the appropriate treatment of temperature and solvation effect, we successfully predicted two-plateaued OCV with fully solvated Li_2S_4 and one-plateaued OCV with non-solvated Li_2S_4 , in agreement with experimental observation in typical Li-S battery with liquid or solid electrolytes.

4 S-C cathode design micrometer level pores: achieving high energy density by changing the porosity

4.1 Summary

To further increase the volumetric energy density of Li-S battery, low cathode porosity and high sulfur loading are desired. However, experimental results showed that the capacity and cycle performance of Li-S battery deteriorated quickly when the cathode porosity dropped from 70% to 40%. In addition, the two discharge plateaus also showed difference shapes depending on the porosity. To further understand the design limitations, a mechanism-based analytical model was developed to quantify the experimental observations. It was demonstrated that the sulfur utilization was mainly limited by the amount of soluble polysulfide in the first plateau and the electronically-accessible surface area of the carbon matrix limited the second plateau. It was predicted that an optimal porosity of 52% will maximize the volumetric energy density without limiting the sulfur utilization, which in turn leads to the loss of electrochemical performance. The consistency of the analytical model and the experimental results validated the dominating mechanisms associated with cathode porosity reduction.

4.2 Introduction

Despite the high specific energy density of 2,500 kW/kg, which is considerably higher than traditional Li-ion battery, the practical application of the Li-S battery is still challenging. The major issues facing broader applications were the intrinsic insulating characteristics of sulfur, the shuttle phenomenon that results from the high solubility of polysulfide, and the volume expansion of sulfur during lithiation [204,205]. To address these issues, host materials had been incorporated with elemental sulfur to increase the electrical conductivity and sulfur utilization. Carbonaceous materials, such as mesoporous carbon and microporous carbon, had been demonstrated with improved sulfur utilization and cycle stability due to large pore volume

and the reduction of Li-polysulfides (Li-PS) diffusion.

The infiltration of sulfur into a porous carbon matrix as a sulfur/carbon composite for sulfur electrode was considered as an effective approach that can be easily scaled up to suppress the diffusion of polysulfide and improve transportation of electrolyte [206,207]. The pore size and structure play an important role in the electrochemical performance of Li-S batteries due to the dissolution of lithium polysulfides which cause the redox shuttle reaction. Because of the depletion of electrolyte, most cells were assembled and tested with excess electrolyte (Electrolyte/Sulfur ratio is greater than 10 mL/g) which also leads to the loss of active materials, such as Li_2S_2 and Li_2S which formed from the disproportionation of polysulfides, then precipitated out of the electrolyte solution and deposited in the dead space in the cell. Therefore, electrolyte quantity is critical for the volumetric energy density of batteries, since it accounts for a major part of the total cell weight [208]. At present, state of art designs for Li-S pouch cell require an E/S of 3 mL/g to achieve energy density of 300 Wh/kg which is comparable to commercially available Li-ion battery [209]. Besides, electrolyte quantity is strongly associated with the porosity of the electrode. The cell level volumetric energy density will be around 400 Wh/kg with 70 % porosity when the areal density of sulfur is 5 mAh/cm². If the porosity of the electrode is reduced by 10%, volumetric energy density may reach 500 Wh/kg due to the reduction of electrolyte quantity. This is the target of the DOE Battery 500 program for an advanced battery of EVs [210]. Inspired by the above insights, means for manipulating the porosity to obtain Li-S battery with stable electrochemical performance and high volumetric energy density (≥ 500 Wh/kg) is of immense importance.

In this chapter, a combined experimental/theoretical approach aimed at quantifying the effects of sulfur electrode porosity on Li-S batteries. Experimental results about the influence of the porosity in cathode materials on the electrochemical performance of Li-S batteries were first reviewed. Secondly, the diffusion distance of Li-PS during the battery cycling was then

calculated by MD simulation. By comparing with the pore size in the carbon matrix, it can determine whether the electrolyte inside and outside the pore can be fully utilized or not. Last, an analytical model was developed to quantify the unique impact of cathode porosity on battery performance.

4.3 Summary of the experimental results

Experiments in this part were done by our partner Ning Kang, Li Yang and Mei Cai from General Motors Global R&D Center, and Dongpin Lu and Jie Xiao from Pacific Northwestern National Lab. Through a calendaring process with adjustment on the gap between rollers, the S-C cathode materials with different porosities based on the same carbon matrix was synthesized. The morphology of the synthesized S-C cathode is observed with SEM, as shown in Figure 4.1. At porosity of 70%, large void space was witnessed with particles overlapped and distributed ununiformly across the surface. At porosity of 60% and 50%, the distance between particles was greatly reduced and the empty space was also less visible due to the calendaring process. Meanwhile, particles packed more condensed across the surface of the electrode, and the aggregation is also obvious.

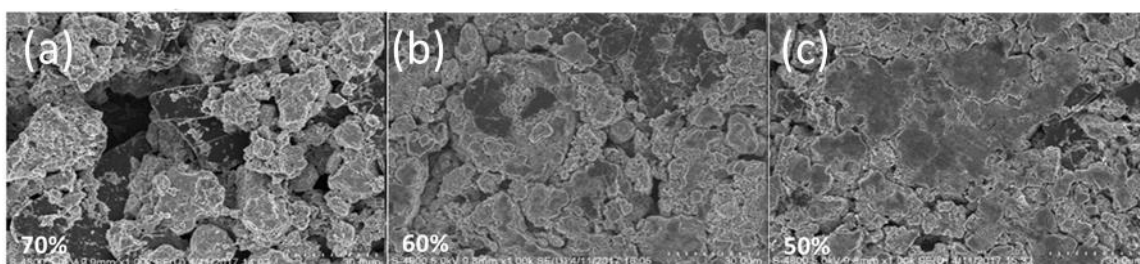


Figure 4.1 SEM images of the sulfur electrode with a porosity of 70% (a), 60% (b), and 50% (c). (In courtesy of Ning Kang, Li Yang and Mei Cai from General Motors.)

The as-prepared sulfur electrodes were used as the cathode, Li metal was used as the anode. The electrolyte was 0.4 M lithium bis(trifluoromethanesulfonyl) imide (LiTFSI, purchased from BASF) and 0.6M lithium nitrate (LiNO_3 , 99.95% purity, purchased from Sigma-Aldrich)

in 1,2-dimethoxyethane and 1,3-Dioxolane, 1:1 by volume, purchased from BASF). Figure 4.2a showed the charge-discharge profile of Li-S cells with sulfur loading of 2.5 mg/cm^2 at a porosity of 70%, 60%, 50%, and 40% respectively. A typical two-plateau discharge behavior of Li-S battery was observed for the porosity of 70% and 60%. The turning point between the two plateaus remained at capacity about 280 mAh/g and the total initial discharge capacity was above 1100 mAh/g, implying the electrochemical performance of Li-S batteries was not severely affected. As the porosity was further reduced to 50%, the turning point moved backward to 260 mAh/g. Though a high capacity around 1100 mAh/g was still observed, the 2nd discharge plateau suffered from depression, decreasing the output energy. When the porosity was reduced to 40%, the initial discharge capacity was only 255 mAh/g, and the 2nd discharge plateau was compressed severely.

Cycle performance of Li-S batteries under different porosities was presented in Figure 4.2b. The capacity of the cell with a porosity of 70% decreased at the beginning and increases gradually after the 12th cycle then maintains relatively stable. Cell with a porosity of 60% showed slightly higher capacity for the first 10 cycles compared with the former, but the capacity decay was more significant in the following cycles. Cell with a porosity of 50% presented more stable cycle performance compared with cells of higher porosity, but the capacity dropped suddenly after 34 cycles. As for cell with a porosity of 40%, it failed quickly after 2 cycles with an initial capacity of 255 mAh/g. Though small pores of the carbon matrix are beneficial for the utilization of active materials [208], an electrode with a porosity of 70% still presented better performance compared with the ones with low porosity.

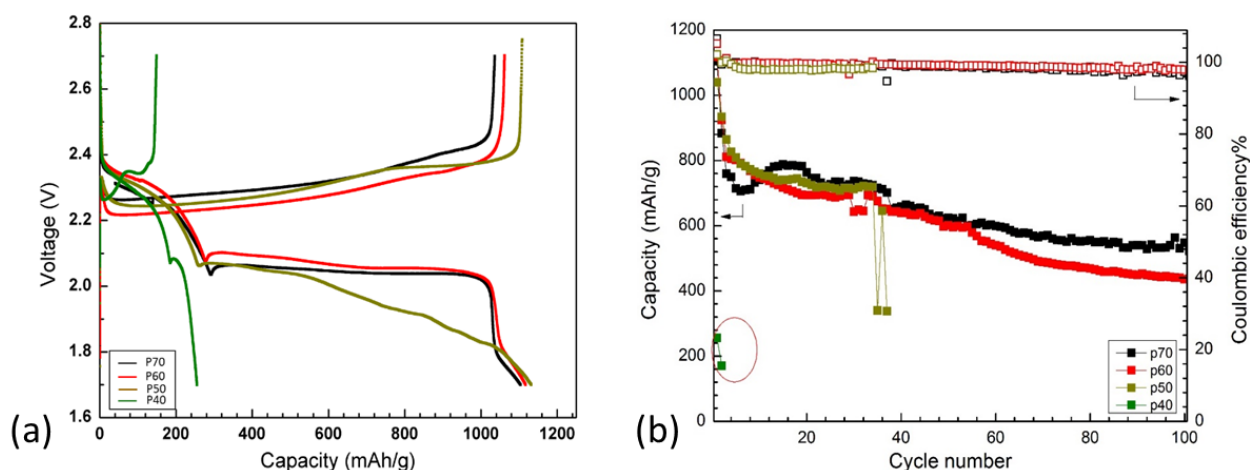


Figure 4.2 Charge-discharge profile (a) and cycling performance (b) of Li-S cells with sulfur loading of 5 mg/cm² under different porosity. (In courtesy of Ning Kang, Li Yang and Mei Cai from General Motors.)

4.4 Calculation of diffusion distance of Li-PS

4.4.1 Calculation details

Classical MD was used to investigate the diffusion coefficient of Li₂S₄ in DME solvents. First, amorphous cells were constructed with randomly packed Li₂S₄ and DME molecules with different ratios. The exact composition in each solution and the corresponding Li₂S₄ concentration in terms of S are listed in Table 4.1. The original density was set to be the same as the solvent (0.90 g/cm³). The solution structure was then optimized with the compass2 forcefield [199]. The force field types were as follows: c4o (0.054) for C in CH₂, c4o (0.001) for C in CH₃, o2e (-0.32) for O, h1 (-0.053) for H, li+ (1.00) for Li, s2s (-0.27) for mid S, s (-0.73) for end S. The optimized cell was subject to a classical MD simulation with NPT ensemble at 298K and 1 atm for 100 ps to determine the density. The converged densities, calculated as the average density of the last 50 ps, were also listed in Table 4.1. After that, an NVT simulation at 298 K was conducted for 100 ps to track the mean squared displacement (MSD) of both Li₂S₄ and DME. The self-diffusion coefficient D was calculated with classical molecular dynamics simulation based on the following equation:

$$D = \frac{1}{6N_a} \lim_{\tau \rightarrow \infty} \frac{d}{d\tau} \sum_{t=0}^{t-\tau} \sum_i^{N_a} [r_i(t+\tau) - r_i(t)]^2 = \frac{1}{6} \lim_{t \rightarrow \infty} \frac{d}{dt} MSD(\tau) \quad (4.1)$$

Here t is the simulation time, τ is the time interval. N_a is the total number of atoms in given species. $r_i(t+\tau)$ and $r_i(t)$ is the position of atom i at time $t+\tau$ and time t .

Given the diffusion coefficient, the self-diffusion distance x of Li_2S_4 in the first plateau can be further estimated as

$$x = \sqrt{Dt} \quad (4.2),$$

where t is the diffusion time. Considering that the first discharging plateau generally contributes 25% of the total theoretical capacity, the diffusion time t can be estimated at 25% of the total discharging time.

All the classical MD simulations were done through forcite modulus in Materials Studio. The timestep was set to be 1 fs. The temperature was controlled by Nosé algorithm [200] and the pressure was controlled by Berendsen algorithm [201]. An Ewald summation was used for the electrostatic interaction, and the van der Waals interaction was truncated at 15.5 Å.

4.4.2 Calculated diffusion distance

To answer the question: how much electrolyte inside and outside the pore can be used to dissolve the Li-PSs, the diffusion of Li-PSs was first determined and compared with the pore size of the carbon matrix. The MSD of Li_2S_4 and DME solvent were plotted as a function of time interval τ in Figure 4.3a and 4.3b. The calculated self-diffusion coefficients D of Li_2S_4 and DME, as well as the composition, PS concentration in terms of S and simulated density of each solution, were summarized in Table 4.1. A typical snapshot of the 1.9 m and saturated 8.7 m solution were shown in Figure 4.3c and 4.3d. The diffusion coefficient of DME in pure DME solvent and 1.9 m solution were 23.1 and 19.1, respectively. These values were consistent with the calculated value from Park [211] and experimental value from Hayamizu [212], confirming

the validity of the force field and the simulation method. In the 1.9 m solution, the self-diffusion coefficient of Li_2S_4 was $5.6 \times 10^{-10} \text{ m}^2/\text{s}$. With an increase in PS concentration, $D(\text{DME})$ and $D(\text{Li}_2\text{S}_4)$ both drop dramatically. For the saturated 8.7 m solution and over saturated 15.4 m solution, the self-diffusion coefficient of Li_2S_4 is only 2.7×10^{-10} and $0.6 \times 10^{-10} \text{ m}^2/\text{s}$, respectively.

Table 4.1 List of composition, density, PS concentration and diffusion coefficient of DME and Li_2S_4 in each solution.

Solution	N(Li_2S_4) : N(DME)	Density (g/cm^3)	c_s (mol/L)	$D(\text{DME})$ ($10^{-10} \text{ m}^2/\text{s}$)	$D(\text{Li}_2\text{S}_4)$ ($10^{-10} \text{ m}^2/\text{s}$)
Pure DME	0:300	0.88	0	23.1	-
1.9 m	14:280	0.94	1.9	19.1	5.6
4.9 m	39:299	1.01	4.9	13.0	5.0
8.7 m	60:240	1.10	8.7	6.9	2.7
15.4 m	100:200	1.24	15.4	2.5	0.6

The estimated self-diffusion distance x was plotted as a function of C-rate in Figure 4.3e. As we can see, either a higher concentration or a lower C-rate could result in smaller diffusion distance x . For the saturated 8.7 m solution, the estimated distance at a typical 0.1 C rate is 1.55 mm. Even for the oversaturated 15.4 m solution at a C rate as high as 2.5, the diffusion distance was still 0.13 mm. Overall, the diffusion distance of Li_2S_4 during the discharging process was estimated to fall in the 1~3 mm at a discharge rate of 0.1 C, which was far beyond the pore size in the S-C composite cathode, but comparable to the dimension of the coin cell. This meant that the Li_2S_4 diffusion in the cathode region is still fast enough in the cathode region. Thus, all electrolyte inside the pore can be utilized to dissolve the Li-PS, but only part of the electrolyte outside the pore can be utilized.

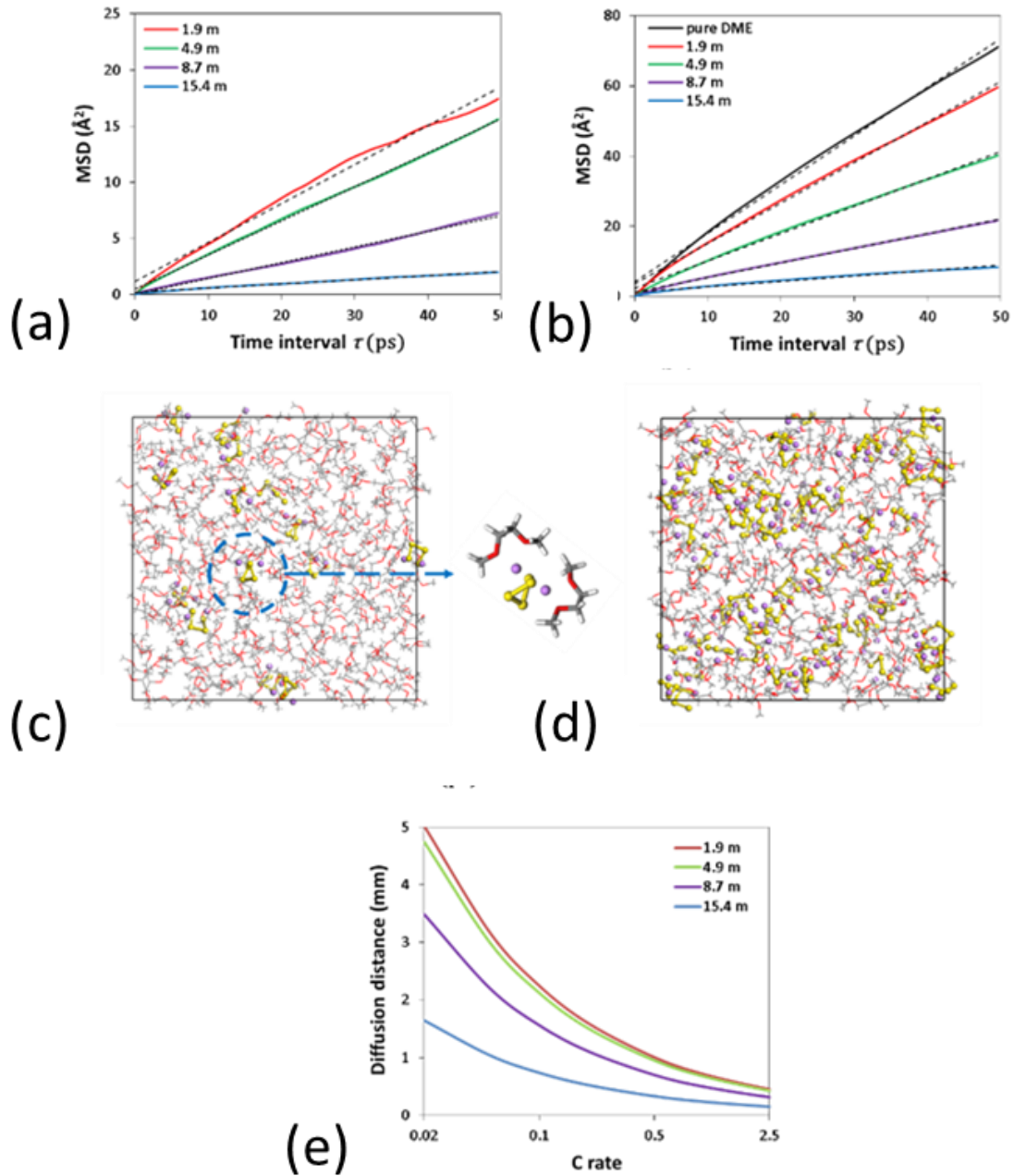


Figure 4.3 Simulated average mean squared displacement (MSD) of Li_2S_4 (a) and DME (b) as a function of simulation time in each solution. A typical snapshot of solution 2.1m (c) and saturated 8.7 m (d) solution. Estimated self-diffusion distance of Li_2S_4 as a function of C-rate in each solution (e).

4.5 Analytical model

According to the experimental observation, the overall performance of the Li-S battery was highly impacted by the porosity of the S/C composite cathode. It was first reported by Zheng [90] that the carbon matrix of the S-C cathode had a significant influence on the second

plateau. A flat second plateau was observed with a carbon matrix of the high surface area, and a depressed second plateau was observed with a low surface area [90]. Our experimental data showed the decrease of the porosity not only caused a depressed second plateau, but also a shortened first plateau as shown in Figure 4.2a. Thus, an analytical model was constructed to quantify the unique impact of cathode porosity, p , on the battery performance.

4.5.1 Determination of the limiting factor for the capacity in the first plateau

The pores shown in Fig 4.1 will be filled with electrolyte. Thus, the amount of electrolyte in the cathode will scale with the porosity, p . Considering that the separator is connected to the porous cathode and should provide extra space to store electrolyte, the total pore volume, V_{pore} , consists of two contributions, the pore volume in the separator, $V_{pore}(sep)$, and the pore volume in the cathode, $V_{pore}(cat)$.

$$V_{pore} = V_{pore}(sep) + V_{pore}(cat) \quad (4.3).$$

$V_{pore}(sep)$ was calculated to be 2.5 mm³ based on the total volume (6.3 mm³) and the porosity (40%) in the Celgard 2500 separator used in the experiment. $V_{pore}(cat)$ includes the micro pores inside the carbon particles and the void space between carbon particles. It scales with the porosity, p as

$$V_{pore}(cat) = p * V(cat) = p(V_{dense}(cat) + V_{pore}(cat)) \quad (4.4).$$

Based on the experimentally measured total volume of the cathode, $V(cat)$, and p , it can be extrapolated that the volume of dense S/C composite cathode material without any porosity $V_{dense}(cat)$ is about 5.3 mm³.

Based on the sulfur loading of 5.0 mg/cm², the total mass of S in the cathode, $m_s(total)$ was 6.5 mg for a cathode area of 1.3 cm², corresponding to a volume of 3.25mm³.

First, we can assume all the electrolyte will be utilized. The diffusion coefficients of Li₂S₄ in a typical solvent, DME, were calculated as a function of Li₂S₄ concentrations by classical

MD simulation, as shown in Appendix 4.1A. Although the Li_2S_4 diffusion coefficient decreases with increasing concentration, the diffusion distance of Li_2S_4 during the discharging process was estimated to fall in the 1~3 mm at a discharge rate of 0.1 C, which was far beyond the pore size in the S-C composite cathode. Thus, the diffusion of PS was not the limiting factor for sulfur utilization.

In fact, if we assume all the sulfur be converted to Li_2S_4 , its concentration will exceed the saturation limit even at a high porosity of 70 %. Therefore, we consider the first plateau would be terminated once the Li_2S_4 concentration reaches the saturation limit, thus the S utilization will be limited by the maximum amount of soluble Li_2S_4 . To quantify this mechanism, we define the mass of utilized S (those converted to Li_2S_4) as $m_s(uti)$, and the corresponding S utilization percentage $P_s(uti)$ as:

$$P_s(uti) = \frac{m_s(uti)}{m_s(total)} = \frac{Q_{pr}}{Q_{th}} \quad (4.5).$$

Q_{pr} and Q_{th} were practical capacity and the theoretical capacity in the first plateau, respectively. A Q_{th} value of 420 mAh/g can be obtained from the conversion of S to Li_2S_4 , and the Q_{pr} values can be read from the discharging curves in Figure 4.2b with different porosities. These four experimental data points of $P_s(uti)$ were plotted as blue points in Figure 4.3a. The $P_s(uti)$ was maintained at ~70% for porosity higher than 60%. Thus, 30% of S was considered inactive in the first plateau and the first plateau will be terminated when all active S is converted to Li_2S_4 . Further decrease in porosity led to a decrease in the $P_s(uti)$, since the amount of electrolyte in V_{pore} can no longer fully dissolve the produced Li_2S_4 , thus limits the utilization of active S. The Li_2S_4 solubility in the electrolyte solvent in terms of S is $C_{max} = 8 \text{ mol/L}$ [213]. Thus, the sulfur utilization limit is determined by the volume of the electrolyte, as

$$P_s(uti) = \frac{gV_{pore}M_s \cdot C_{max}}{m_s(total)} \quad (4.6),$$

where V_{pore} is the total pore volume defined in Eqn (4.3), $M_s = 32g/mol$ is the molar mass of S, and g is introduced to account for the excess electrolyte that was not filled in the pores, as coin cells often have excess electrolyte. Thus $P_s(uti)$ is the minimum value calculated from Eqn. (4.6) or 70%. To match the modeling results to the four experimental data points, a g value of 1.8 was used. Based on the amount of utilized sulfur, the dissolved Li_2S_4 concentration was also calculated in terms of mole of S.

$$c_s(uti) = \frac{m_s(uti)}{gV_{pore}M_s} \quad (4.7).$$

In Figure 4.3a, the experimental values of $c_s(uti)$ are plotted as black dots while the modeled $c_s(uti)$ are plotted as black line, both as a function of porosity. Thus, $c_s(uti)$ increased with reduced porosity and converged at the saturated concentration of 8 mol/L [213] when the porosity was below 60 %. This confirmed the saturation of PS in the electrolyte solvent was the limiting factor for the capacity in the first plateau.

4.5.2 Depression of the second plateau

The electrochemical reaction corresponding to the second plateau will proceed on the carbon surface, where the dissolved Li_2S_4 takes electrons from the surface and Li^+ -ion from the electrolyte and deposit as insulating Li_2S_2 and Li_2S on the surface.

The depression of the second plateau is related to losing the pore surface area, A , which also scales with cathode porosity, p , according to different pore structure models . In general, the total surface area, $A \propto V(cat)^\alpha$, where α is an empirical constant depending on the pore structure, usually in the range from -1 to 1 [214]. Given the fact that the porosity was changed by the calendaring process in the thickness direction, the α value of 1 was chosen. Further relating $V(cat)$ with the porosity p , the total surface area A decreases with p

$$A(p) = \frac{A_0}{1-p} \quad (4.8),$$

As we know the measured BET surface area, A , is about 1000~1100 m²/g at $p = 70\%$, the rest of A can be obtained as a function of p .

Assume if all the sulfur can be converted to Li₂S₄ dissolved in the electrolyte, the carbon surface originally covered by the insulating sulfur will become carbon surface and be able to facilitate the charge transfer reaction. However, if there is unutilized S left after the first plateau reaction, the S covered surface is still insulating. Thus, an effective surface area, A_{eff} , is defined to account for the unutilized sulfur, $m_s(total)-m_s(uti)$, with a parameter of k ,

$$A_{eff} = A - k[m_s(total)-m_s(uti)] \quad (4.9).$$

In Figure 4.6b, A and A_{eff} with different k values were plotted as a function of p . Both A_0 and A_{eff} would decrease with decreasing porosity, but the decrease in A_{eff} was much faster compared with A_0 . This was due to the increase of unutilized sulfur covering carbon surface area. The exact value of k will be determined later.

Assume the deposited insulating Li₂S₂/Li₂S products are evenly distributed on the carbon surface, the layer thickness d is proportional to the capacity in the second plateau $Q - Q_{pr}$, and inversely proportional to the effective surface area A_{eff} . The Q here was the total capacity. Thus, using a constant b , a relationship between thickness d and total capacity Q can be derived as

$$d = b \frac{(Q-Q_{pr})}{A_{eff}m_c} \quad (4.10),$$

$m_c = 3.3$ mg is the mass of the carbon matrix used in the experiment.

The insulating Li₂S₂/Li₂S layer will create resistance and the electrons must tunnel through its thickness to continue the electrochemical reactions. The tunneling resistance R would increase exponentially with the thickness d of the insulating layer [37], as the following

$$R = C(e^{Bd} - 1) \quad (4.11),$$

where C and B are two fitting parameters, which would be discussed later. According to Eqn. (9), R is 0 when the thickness d was negligible. The insulating layer induced IR drop, with I representing the discharging current, in the discharge curve for the second plateau.

Taking the equilibrium open circuit voltage of 2.4 and 2.1 V for the first and second plateau, the discharge curve will show two stages for voltage V and capacity Q :

$$V = \begin{cases} 2.4 & (0 < Q < \frac{m_s(uti)}{m_s(total)} \times Q_{th}) \\ 2.1 - C' \left(e^{\frac{B'(Q-Q_{pr})}{A_{eff} m C}} - 1 \right) & (Q > \frac{m_s(uti)}{m_s(total)} \times Q_{th}) \end{cases} \quad (4.12).$$

$B' = Bb$ and $C' = CI$ were two combined parameters. By fitting the discharge curves with 40% and 50% porosity in Figure 4.2a, the fitted value of B' , C' and k were determined as 1.9×10^{-3} ($m^2 \cdot g$)/mAh, 0.050 V and 1.27×10^5 m^2/g^2 , respectively. The predicted discharging curves at other porosities were shown in Figure 4.4c. It was successfully predicted that the discharging curves showed negligible change when the porosity was higher than 60%. Further decrease in porosity shortened the first plateau and depressed the second plateau. Thus, the capacity dropped rapidly when the porosity decreases in the range of 40% ~ 50%. This was also consistent with experimental observation.

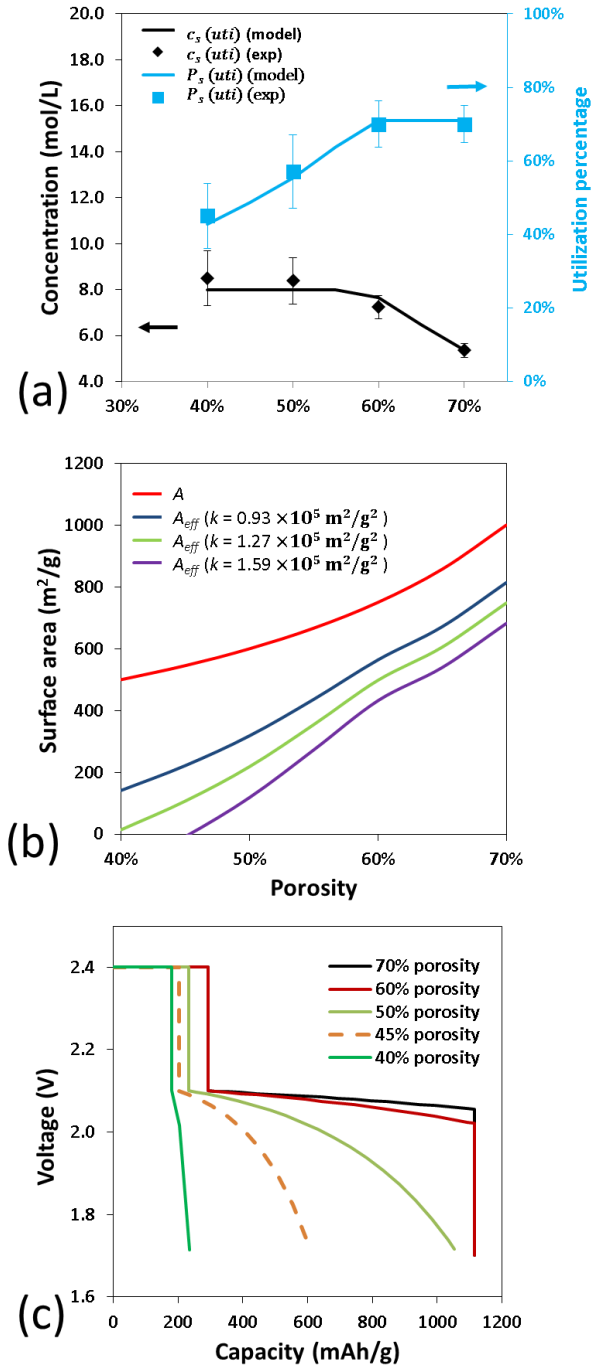


Figure 4.4 Predicted PS concentration and S utilization as a function of porosity (a). Predicted total surface area and effective surface area as a function of porosity (b). Predicted discharging curves at different porosity (c).

4.5.3 The volumetric and gravimetric energy density

Based on the above discussion, the impact of porosity on the electrochemical performance can be summarized in the inserted schematics in Figure 4.5. When the porosity is high ($> 55\%$),

$P_s(uti)$ maintained at 70%, contributing to a long first plateau. Besides, A_{eff} was at least 500 m²/g, which is high enough to keep the deposited Li₂S₂ and Li₂S layer thin until all generated PS is converted to Li₂S₂ and Li₂S, as shown in the right schematics in Figure 4.5. The resistance caused by this thin layer formed on the carbon surface is less than 0.1 V and the second plateau will remain flat. With a medium porosity (~ 50 %), $P_s(uti)$ dropped to 55 %, leading to a shortened first plateau. What's more, due to a decrease in porosity and an increase in the unutilized S, A_{eff} is only ~200 m²/g. The deposited layer of Li₂S₂ and Li₂S will grow thicker and thicker as the second discharging reaction continues, causing the increase in the resistance. As shown by the analytical model, the IR drop is ~0.2 V at a total capacity of 800 mAh/g and ~0.4 V at a total capacity of 1100 mAh/g, demonstrating an obvious depression in the second plateau. At low porosity (< 45 %), $P_s(uti)$ of ~ 42 % leads to an even shorter first plateau. A_{eff} will also drop sharply to ~ 15 m²/g. As a result, the thickness of the Li₂S₂ and Li₂S layer and the caused resistance grew very quickly, as shown in the left inserted schematics in Figure 4.5. The total capacity is less than 250 mAh/g when the IR drop of 0.4 eV and the voltage limit of 1.7 V are reached. This is the reason for the severe depression of the second plateau accompanied by low porosity.

In Figure 4.5, the predicted gravimetric energy density based on the mass of S and volumetric energy density based on the volume of cathode materials were plotted as a function of porosity, with experiment data points also included. The gravimetric energy density remains almost constant for any porosity higher than 55% before it experiences a significant drop when the porosity becomes lower than 50%. The volumetric energy density increases with a decreasing porosity when the porosity is higher than 55%. However, once the porosity reaches below 50%, the volumetric energy density also drops dramatically. Therefore, an optimal porosity of around 52 % is predicted to achieve the best gravimetric energy density and volumetric energy density for the electrode materials used in this study.

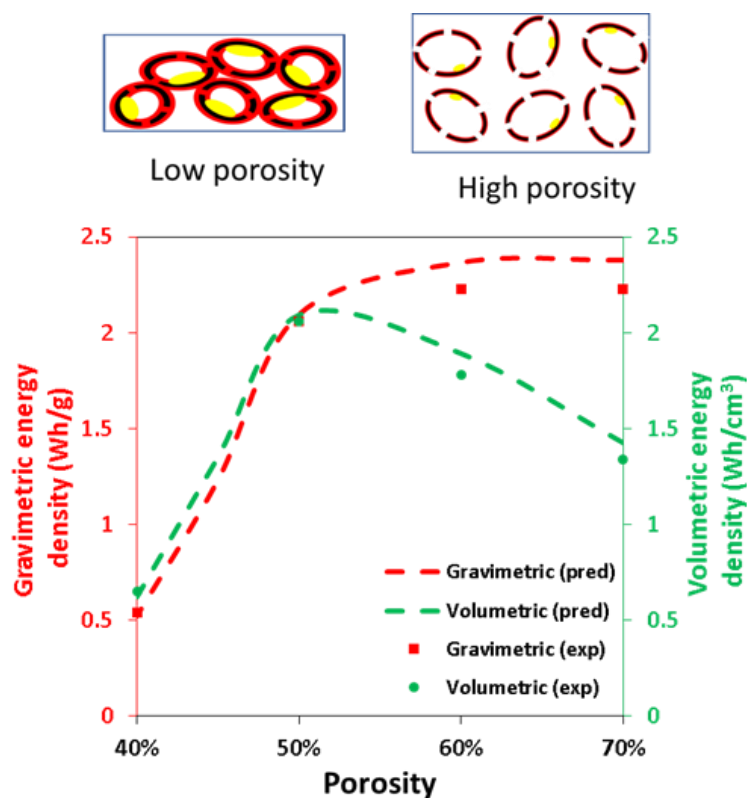


Figure 4.5 The predicted gravimetric energy density based on the mass of S and volumetric energy density based on the volume of cathode materials. The schematics showing the difference between low porosity and high porosity were also inserted. The unutilized S, carbon matrix and deposited $\text{Li}_2\text{S}_2/\text{Li}_2\text{S}$ layer were represented as yellow, black and red, respectively.

4.6 Conclusion

An analytical model was proposed to investigate the influence of porosity. A saturation limiting mechanism was suggested based on the increased concentration of PSs due to the decrease of porosity. When the porosity was reduced, it was found that the total sulfur concentration increased while the sulfur utilization decreased which is ascribed to the reduction of the effective surface area resulting from the deposition of Li_2S . The galvanic charge-discharge curve from simulation corresponded well with the experimental result for the electrodes at different porosity. The energy density reached a maximum value at a porosity of 52% based on the analytical modeling, while the overall trend was consistent with the experimental results, indicating the electrode with the porosity of 50-60% is an optimized parameter for a practical high energy Li-S cell design.

APPENDIX

Table 4.1A List of all parameters used for the analytical model.

Symbol	Description	Category	Value
V_{pore}	Total pore volume in the cathode region	Function of p	-
$V_{pore}(sep)$	Pore volume in separator	Measured constant	2.5 mm ³
$V_{pore}(cat)$	Pore volume in the cathode	Function of p	-
$V_{dense}(cat)$	The volume of dense cathode materials without any porosity	Measured constant	5.3 mm ³
p	Porosity	Variable	-
$P_s(uti)$	Utilization percentage of S in the first plateau	Function of p	-
$m_s(uti)$	Mass of utilized S in the first plateau	Function of p	-
$m_s(total)$	The total mass of S in the cathode	Measured constant	6.5 mg
Q_{pr}	Practical capacity in the first plateau	Function of p	-
Q_{th}	Theoretical capacity in the first plateau	Calculated constant	420 mAh/g
g	The parameter to include extra PS into the bulk electrolyte	Matching constant	1.8
S_{max}	The saturated concentration of PS in the electrolyte solvent in terms of S	Measured constant	8 mol/L
M_s	The molar mass of S	Constant	32 g/mol
$c_s(uti)$	The practical concentration of PS due to the saturation limit	Function of p	-
A_0	The surface area of carbon matrix per gram	Function of p	-
α	Empirical constant to describe the relationship between A_0 and V_0	Empirical constant	1
A_0	Constant to match the BET measured surface area of carbon matrix with 70 % porosity	Matching constant	300 m ² /g
A_{eff}	Effective surface area	Function of p	-
k	The ratio between the mass of non-utilized S and its covering surface area	Fitting parameter	1.27×10^5 m ² /g ²
R	Tunneling resistance caused by the deposited Li ₂ S ₂ /Li ₂ S layer	Function of p	-
C	The parameter to describe the relationship between tunneling resistance and layer thickness. Later combined to C'		-
B	The parameter to describe the relationship between tunneling resistance and layer thickness. Later combined to B'		-
d	The thickness of Li ₂ S ₂ /Li ₂ S layer	Function of p	-
Q	Total capacity in the discharging curve	Variable	-
b	The parameter to describe the relationship between thickens and total capacity. Later combined to B'		-
m_c	Mass of carbon matrix in the cathode	Measured constant	3.3 mg
I	Discharging current, later combined to C'	Measured constant	-
$B'=Bb$	Parameters to describe the relationship between discharging voltage and capacity	Fitting parameter	1.9×10^{-3} (m ² ·g)/mAh
$C'=CI$	Parameters to describe the relationship between discharging voltage and capacity	Fitting parameter	0.050 V

5 S-C cathode design with nanopores: synergetic effect between pore size and electrolyte concentration

5.1 Summary

The partially solvated Li_2S_4 may exist in high concentration solutes, which is different from both the fully solvated Li_2S_4 and non-solvated Li_2S_4 . In this chapter, the energy of partially solvated Li-PS and its corresponding OCV were calculated from DFT with appropriate solvation models determined in Chapter 3. It was revealed that if Li-PS changes from partial or no-solvated state to fully solvation, its formation energy increases, leading to a transition from the one-plateaued to the two-plateaued OCV. Based on this, the method to create partially solvated Li-PS were discussed. As the partially solvated Li-PS can be realized either by a highly-concentrated electrolyte or by minimizing the pore size in the carbon/sulfur composites to limit the number of solvents transported into the pores, a new Li-PS dissolution mitigation strategy based on this synergetic effect is proposed by modeling and verified by experiments.

5.2 Introduction

As stated in Chapter 3, the difference between one-plateaued and two-plateaued discharging curves were clarified to the solvation status of Li-PS. However, the wide gap between fully solvation status and non-solvation status was still unknown.

One approach to achieve non-solvation status for Li-PS was to control the pore size in the carbon matrix to block the solvent outside [69][70]. Considering the molecular size of the solvent molecule, the pore size falls into sub-nanometer (sub-nm) level. In the experiment, accurate controlling of the pore size ~ 0.5 nm in microporous carbon matrix enabled one-plateaued discharging curves [67,68,207]. However, a complicated and costly synthesize method usually involved. For example, the synthesized from the raw material CNT to the final carbon matrix by Sen [67] involved ultrasonic suspension, heating in a vacuum, hydrothermal

reaction, centrifugation, and calcination. Thus, it was highly desired to achieve one-plateaued OCV curve with a carbon matrix with large pore size and simple synthesis method. Actually, one plateaued OCV curves were still observed with a pore size of 3~5 nm[69,71–73]. Obviously, the solvation status of Li-PS was different from the fully solvation since they could not block the solvent completely. Another approach was to use change the type or concentration of electrolyte. According to Zheng *et al.*, a complete transition from two-plateaued OCV curves to one-plateaued OCV curves was only observed when the LiTFSI concentration was 12 M in ether-based electrolyte [181]. This indicated the rigorous demand to achieved the non-solvated status of Li-PS. Furthermore, the too high concentration would result in a very high viscosity, which resulted in slow Li-transport in the electrolyte. However, in lots of researches, ether-based electrolyte with concentration 3~5 M shifted the two-plateaued OCV curves to one-plateaued OCV curves [75–78]. Obviously, the solvation status of Li-PS was neither fully solvated nor non-solvated.

The solvation status of Li-PS in both 3~5 nm pore and the concentrated electrolyte can also help to shift the two-plateaued OCV curve to one-plateaued OCV curve. Therefore, the solvation status of Li-PS in such these two cases are worth investigating. Furthermore, the influences of the pore size and electrolyte concentration on the OCV curves were seldom combined.

In this chapter, the energy of partially solvated Li-PS and its corresponding OCV were calculated from DFT with appropriate solvation models determined. Based on this, the method to create partially solvated Li-PS were discussed. As the partially solvated Li-PS can be realized either by a highly-concentrated electrolyte or by minimizing the pore size in the carbon/sulfur composites to limit the number of solvents transported into the pores, a new Li-PS dissolution mitigation strategy based on this synergetic effect is proposed by modeling and verified by experiments.

5.3 Model details

The OCV and formation energy calculation introduced in section 3.3.1 was followed. For the solvation energy calculation, the increase in the concentration of Li_2S_4 would change the dielectric constant of the solution. In Gavish's analytical model based on the aqueous electrolyte [215], the dielectric constant was decided by the concentration, the dielectric constant of solvent and salt, and the excess polarization of the ions. However, the specific relationship regarding Li_2S_4 in the ether-based electrolyte was still missing. In such a condition, the cluster model and explicit model, both excluded the explicit dielectric continuum, were used to calculate the solvation energy of partially solvated Li_2S_4 . The detailed review of the solvation was shown in Section 3.3.2.

In the explicit model, a solution of 10 Li_2S_4 molecules and 20 DOL molecules were used to simulate a highly-concentrated solution. The converged density averaged from NPT MD simulation was $1.41 \pm 0.014 \text{ g/cm}^3$. After that, *ab initio* MD (AIMD) implemented in VASP with NVT ensemble at a timestep of 1 fs was performed for 1.5 ps at 300K. The average potential energy during the last 1 ps AIMD simulation were both recorded to obtain the solvation energy and estimate its fluctuation. Three configurations with the lowest potential energy from AIMD simulations was used as the initial configuration for geometry optimization in DFT calculations. The same procedure was also conducted for a pure DOL solvent with 20 molecules as a reference in an explicit model.

In the cluster model, a $\text{Li}_2\text{S}_4 \cdot 2\text{DOL}$ cluster was created for the first solvation shell of a partially solvated Li_2S_4 by removing 2 DOL molecules from the optimized full solvation shell $\text{Li}_2\text{S}_4 \cdot 4\text{DOL}$, then relaxing with a classical NVT MD simulation at 298K for 50 ps. The configuration with the lowest potential energy was used as the initial configuration for DFT minimization. The energy of optimized DOL was used to represent the energy of the solvent in

the cluster model.

Both plane-wave DFT implemented in VASP and the local-basis set DFT implemented in DMol3 were applied to the partially solvated Li_2S_4 for comparison. Specifically, spin-polarized, all-electron, local basis set (Double Numerical plus polarization, DNP [183]) DFT implemented in Dmol³ [184] in Materials Studio was used. The exchange-correlation was treated with the generalized gradient approximation (GGA) Perdew-Wang-91 functional [185]. To capture the temperature effect, the contributions from vibration, rotation, and translation were calculated through vibrational analysis by finite differences of analytic gradients, based on the detailed formula from Hirano's work [186]. Only the ion positions were relaxed during an energy minimization, until one of the three convergence criteria, as 3×10^{-4} eV/system, $0.05 \text{ eV}/\text{\AA}$, and 0.005\AA for energy change, force, and displacement, respectively, was reached. For comparison, the energy of the Dmol³ minimized structures were recalculated with the plane-wave DFT implemented in the Vienna ab initio simulation package (VASP). Potentials constructed with the full potential projector augmented wave (PAW) method were used for the elemental constituents [187]. The exchange-correlation was treated with the GGA Perdew-Burke-Ernzerhof (PBE) functional [188]. The cutoff energies and K-points used were 700 eV and $1 \times 1 \times 1$.

5.4 Computational results

5.4.1 Partially solvated Li_2S_4 and the transition from the two-plateaued OCV to the one-plateaued OCV

The partially solvated Li_2S_4 may exist in high concentration solutes. A liquid cell of 10 Li_2S_4 and 20 DOL was used for explicit solvation model. The solution structure after 2 ps AIMD simulations and its corresponding CN plots are shown in Figure 5.1a and 5.1b.

Comparing Figure 5.1b with the fully solvated Li_2S_4 in Figure 3.1c, the first nearest neighbor Li-O and Li-S (end) bonds almost maintained the same distance. However, the coordination number changed. In the partially solvated Li_2S , each Li^+ was coordinated with 1 O in DOL but coordinated with more S (end) with $\text{CN}=2.7$. The continuous climbing of all bonds beyond the distance of 3.5 Å, indicating the second solvation shell is not fully formed. The change of CN in the highly-concentrated solution strongly suggested that the interaction between DOL and Li^+ was weakened due to the limited amount of DOL, while the interaction between S_4^{2-} and Li^+ was enhanced by the formation of a Li-PS network as shown from the snapshot in Figure 5.1b. A cluster of $\text{Li}_2\text{S}_4 \cdot 2\text{DOL}$ was used to represent the partial solvation shell in the cluster model. The optimized structure and its corresponding CN plot are shown in Figure 5.1c and Figure 5.1d, which showed the CN of the Li-O, Li-S (end) and Li-S (mid) bonds are 1, 2 and 1, respectively, similar to that in Figure 5.1b.

The calculated energy contributions for partially solvated Li_2S_4 at both 0 K and 300 K are listed in Table 5.1. Same as the fully solvated and non-solvated Li_2S_4 , the temperature effect caused a free energy change of -0.67 eV per Li_2S_4 molecule when the temperature increased from 0 K to 300 K. Thus, all the following discussion would be made based on the results at 300K. Table 5.1 also listed the solvation energy of partially solvated Li_2S_4 in DOL. The calculated partial solvation energies from VASP were -1.44 eV from the explicit model and -1.30 eV from the cluster model. For comparison, the calculated solvation energy from Dmol3 was -1.43 eV with the cluster model. These consistent solvation energies for the partially solvated Li_2S_4 were smaller (in the absolute value) than the -2.09 eV solvation energy of a fully solvated Li_2S_4 . The corresponding formation energy of the partially solvated Li_2S_4 is -0.01 to -0.04 eV, recommending two-plateaued OCVs. But since these values are close to zero, these voltages of the two plateaus will fall into a very narrow range.

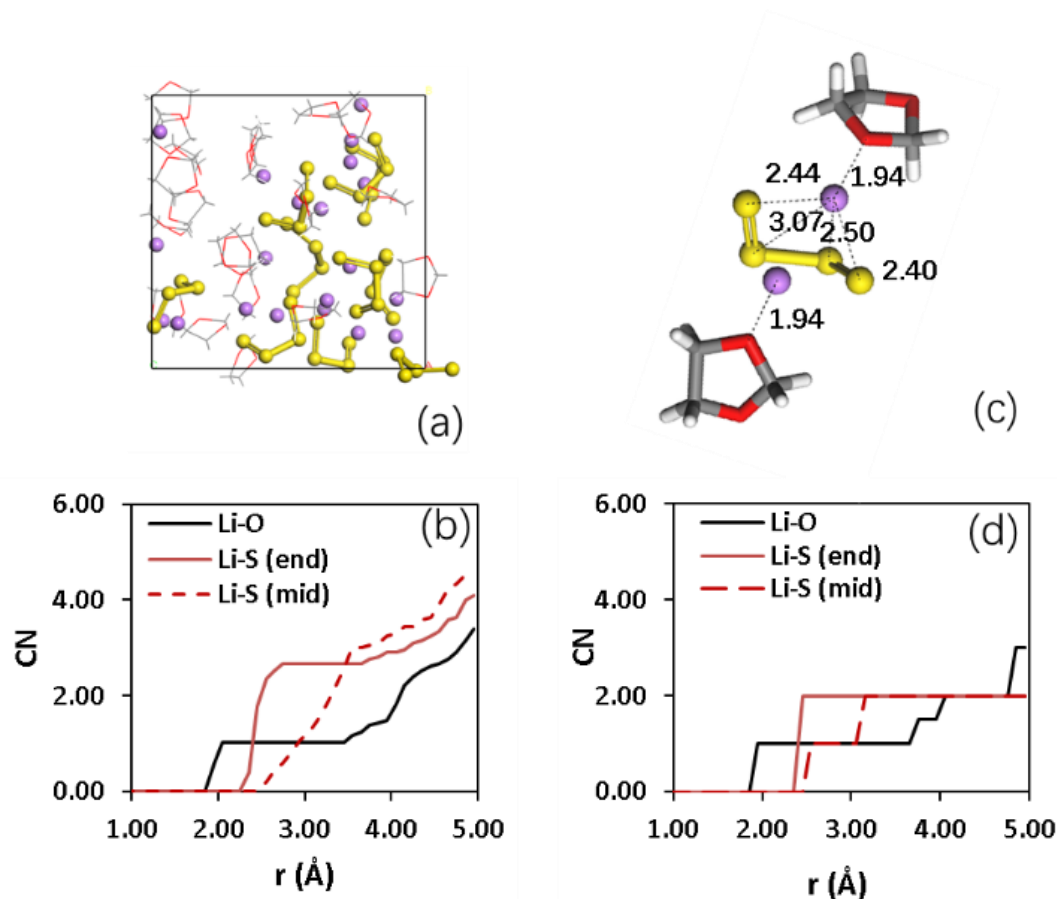


Figure 5.1 Structures of the partially solvated Li₂S₄. (a) The liquid structure of 10Li₂S₄·20DOL and (b) its cumulative CN as a function of cutoff radius. (c) The optimized Li₂S₄·2DOL partial solvation shell and (d) its cumulative CN as a function of cutoff radius. Li, C, S, H and O atoms were represented as purple, grey, yellow, white and red, respectively.

The relative formation energies at 300K of partially solvated Li₂S₄ were compared with that of fully solvated Li₂S₄, and non-solvated Li₂S₄ in Figure 5.2a. Partial solvation energy of -1.39 eV was obtained by averaging the values of the cluster and explicit model for the partially solvated Li₂S₄, resulting in formation energy of -0.03 eV. The predicted OCVs for partially solvated Li₂S₄ was also compared with that for fully solvated Li₂S₄ and non-solvated Li₂S₄ in Figure 5.2b.

For partially solvated Li₂S₄, the increase of partial solvation energy made the two plateaus on the OCV much closer, as the first plateau dropped to 2.15 V while the second plateau increased to 2.09 V. Further increase in the Li₂S₄ concentration in DOL will eventually create a single plateaued OCV. This is consistent with experimental observations in concentrated

electrolyte [25]–[27]. Especially, Zhang *et al.* [25] have also shown that while the second discharging plateau almost maintains the same position, the first discharging plateau gradually dropped when the concentration of the electrolyte increased. This would be an efficient method to avoid Li-PS dissolution. When the Li-salt concentration in the electrolyte increases, the amount of free solvent molecules drops dramatically as more solvent molecules are needed in forming the Li-ion solvation shell. Thus, there will be less free solvent molecules available to form full solvation shells around the newly generated Li-PS. The partially solvated Li-PS can continue to be lithiated while reducing the amount of Li-PS that can shuttle through the electrolyte. In the experiment, the cycling performance is generally improved with the use of highly concentrated electrolyte [26].

5.4.2 Design of S-C cathode through the synergetic effect of pore size and salt concentration on the OCVs

The structure of S-C cathode with S filled nano-pores will impact the local solvation structure of Li-PS. If the pore size is large enough for the first solvation shell $\text{Li}_2\text{S}_4 \cdot 4\text{DOL}$ to pass, the pores will not impose any constraints on the electrolyte concentration or diffusion, leading to severe PS shuttle problem. The size of $\text{Li}_2\text{S}_4 \cdot 4\text{DOL}$ is ~ 1 nm as shown in Fig 2a. Thus, extremely small pores on the order of ~ 1 nm will allow Li^+ diffusion while limiting the diffusion of DOL molecules and blocking the diffusion of $\text{Li}_2\text{S}_4 \cdot 4\text{DOL}$ solvation shell. If any Li_2S_4 could be formed inside these pores, it would likely exist as a non-solvated monomer or cluster, leading to a one-plateaued OCV. Several experiments indeed have created nanopore size on the order ~ 1 nm and reported one-plateaued discharging curves in the liquid electrolyte [171,216]. We hypothesized that partial solvation can be achieved inside the pores within the size range of 1–5 nm, where both Li-ion and solvent molecules can diffuse in, but the diffusion of the newly formed $\text{Li}_2\text{S}_4 \cdot 4\text{DOL}$ solvation shell out of the pore will be limited, due to the comparable size of solvation shell and pore size. This is similar to the reverse osmosis

phenomena in graphene membrane with similar pore size for water desalination [217]. This can create a local higher Li-PS concentration and result in a partially solvated form inside the pore. The formation of Li_2S_4 will become less energetically favorable with increasing Li_2S_4 concentration. This explains why some so-called “quasi one-plateaued” discharging curves were still displayed when the pore size was much larger than the size of the solvent [71–73,218]. Also, due to the limited amount of solvent, the diffusion of Li_2S_4 into electrolyte will also be hindered. As a result, fewer Li-PS will be involved in the PS shuttle, mitigating PS shuttle problem.

However, for practical consideration, the diffusion of Li ions may be hindered in a highly-concentrated electrolyte and 1nm sized pores in the carbon matrix may also add difficulties in the synthesis and limit the sulfur loading. Thus, we propose that the most efficient method to limit the PS dissolution problem is to take advantage of the synergetic effect between pore size and electrolyte concentration since the increase in salt concentration in the electrolyte and the decrease of pore size in carbon matrix can both help to create a partially solvated Li-PS in a liquid electrolyte. This synergetic effect can provide a new strategy to convert the two plateaued discharging curves to one plateaued discharging curves and mitigate the PS dissolution.

Table 5.1 List of free energy terms for partially solvated Li₂S₄ (Unit: eV). EDFT is calculated with basis set DFT in Dmol3. Evib, Svib, Erot, Srot, Etra, Stra are obtained through vibrational analysis. For the solvation model in the method part, E and Cl, stand for explicit model and cluster model, respectively. For the calculation method, D stands for calculations with Dmol3 and V stands for calculations with VASP.

Structure	T/K	E_{DFT}	E_{vib}	$-TS_{vib}$	E_{rot}	$-TS_{rot}$	E_{tra}	$-TS_{tra}$	E_{solv}	Method		G(T)
Partially-solvated Li ₂ S ₄ Li ₂ S ₄ ·2DOL 10Li ₂ S ₄ ·20DOL	0	-22.443	-	-	-	-	-	-	-1.44 [+0.03]	E	V	-23.883
	0	-22.443	-	-	-	-	-	-	-1.30	Cl	V	-23.743
	0	-43754.542	0.244	0	0	0	0	0	-1.43 [+0.081]	Cl	D	-43755.726
	300	-43754.542	0.375	-0.219	0.038	-0.369	0.038	-0.530	-1.43 [+0.08]	Cl	D	-43756.635

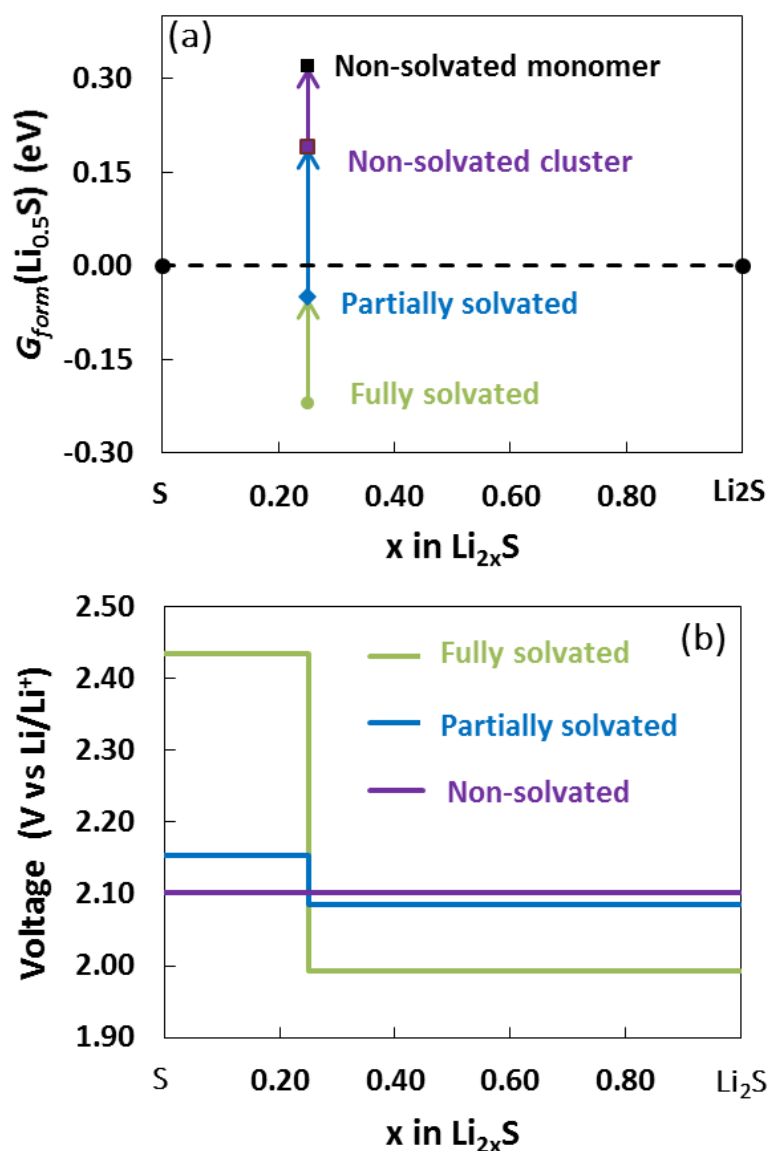


Figure 5.2 The calculated (a) relative formation energies and (b) the corresponding OCVs for Li_2S_4 in different solvation status at 300K. The energy of crystalline S and Li_2S are already shifted to 0 for easy comparison in (a).

Figure 5.3a showed the galvanostatic discharging curves at the 10th cycle in 1M LiTFSI/(DME+DOL) electrolyte with S@CMK3 (5nm) S@CMK8 (3nm) and S@CMS (1nm) cathode, respectively. The corresponding cyclic voltammograms (CV) at the 5th cycle were shown with the same color in Figure 5.3b. For S@CMK3 and S@CMK8, the two reduction peaks were distinctly observed in Figure 5.3a. This was consistent with the typical two-plateaued discharging curves shown in green and red in Figure 5.3b. Furthermore, the two

reduction peaks for S@CMK8 with the average pore size of 3 nm were closer than that for S@CMK3 with 5 nm pores. For the S@CMS with 1 nm pore, the two peaks became broader. The corresponding black discharging curve in Figure 5.1a also showed two much closer discharging plateaus. Thus, the experimental results confirmed the prediction that the two reduction plateaus will move closer with decreasing pore sizes of the carbon matrix.

The galvanostatic discharging curves of S@CMK3 and S@CMS cathode at the 10th cycle in LiTFSI/(DME+DOL) electrolyte with different concentrations are shown in Figure 5.3c and 5.3e. The corresponding CVs in the 5th cycle are shown with the same color in Figure 5.3d and 5.3f. For S@CMK3 with 5 nm pore, when the electrolyte concentration increased from the 1M to 3M, the two plateaus in Figure 5.3c and the two peaks in Figure 5.3d became closer. This confirmed our prediction that increase of salt concentration in electrolyte can also make the two reduction plateaus closer. In even highly concentrated 6M and 9M electrolyte, the discharging curves shown as dark blue and grey in Figure 5.3c gradually showed a gradual transition to the one-plateaued type. This was also consistent with the broad CV peaks in Figure 5.1b. For S@CMS with 1 nm pores, complete one plateaued discharging curves were displayed for 3M and 6M electrolyte, shown as yellow and light blue in Figure 5.3e. One broad CV peak in the entire range of reduction can be seen in Figure 5.3f. The use of CMS with 1nm pores reduced the critical electrolyte concentration to 3M, above which a one-plateaued OCV was observed, confirming the synergetic effect of pore size and electrolyte concentration. It was also worth noting that the second plateau of all galvanostatic discharging curves in Figure 5.3c, 5.3e and 5.1a became quite sloped when the state of discharge is higher than 70%. This was due to the increasing overpotential due to the continuous deposition of insulating Li₂S₂/Li₂S layer [90], as discussed in Chapter 4.

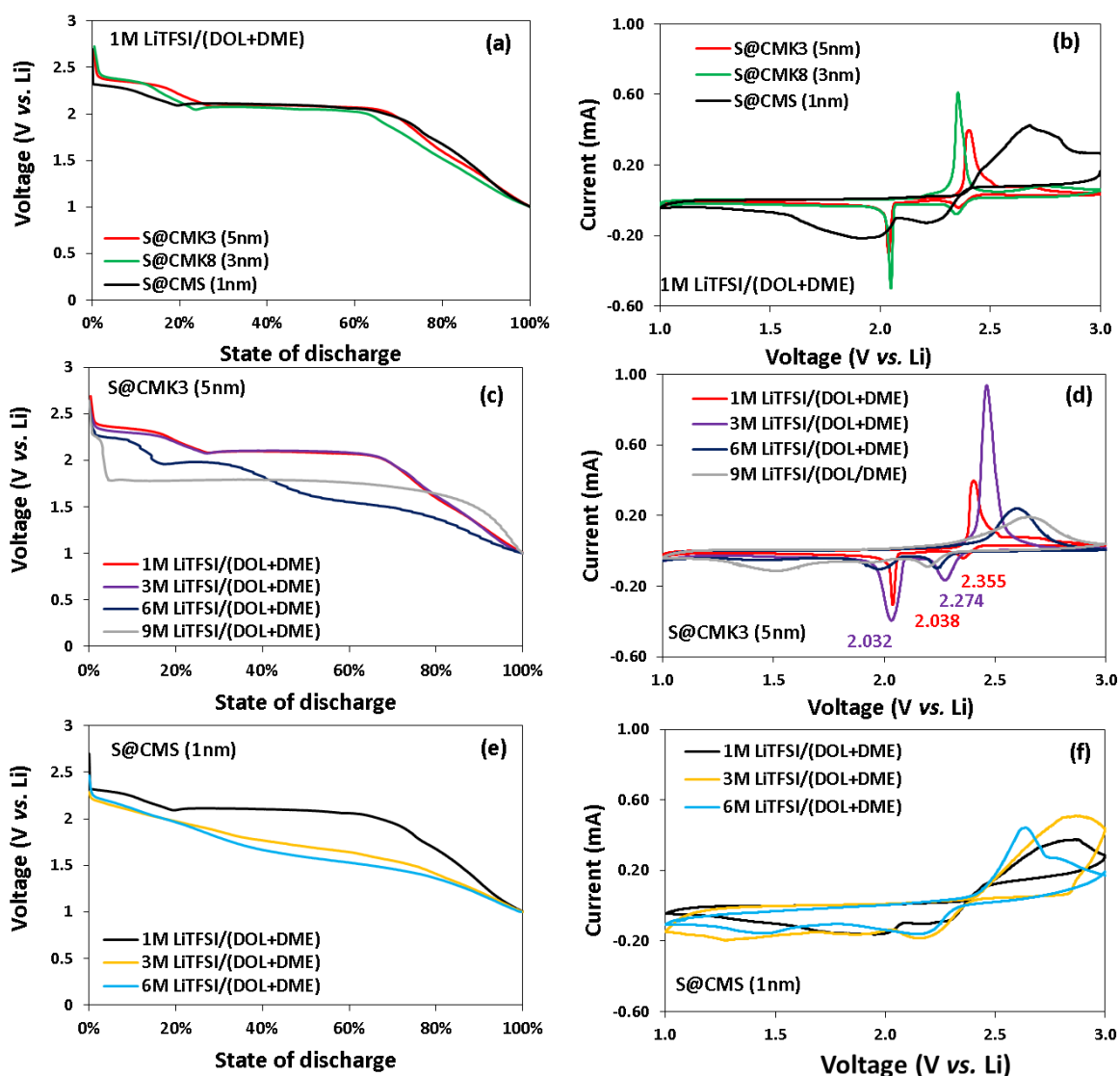


Figure 5.3 Cyclic voltammograms and galvanostatic discharging curve of Li-S batteries: galvanostatic discharging curves (a) and CV (b) in 1M LiTFSI/(DME+DOL) electrolyte paired with cathodes with different carbon matrix pore sizes (labeled in parenthesis), S@CMK3, S@CMK8, and S@CMS, respectively. (b) Galvanostatic discharging curves (c) and CV (d) of S@CMK3 cathode in LiTFSI/(DME+DOL) electrolyte at concentrations of 1M, 3M, 6M and 9M. (c) galvanostatic discharging curves (e) and CV (f) of S@CMS cathode in LiTFSI/(DME+DOL) electrolyte at concentrations of 1M, 3M and 6M. The cyclic voltammograms were tested with a sweep rate of 0.1 mV/s at the 5th cycle. The galvanostatic discharging curves were tested at a 0.1 C rate at the 10th cycle. (In courtesy of Jing Zheng and Chunsheng Wang from University of Maryland.)

5.5 Conclusion

Driven by the modeling, it was predicted that the relative formation energy of Li_2S_4 increases in the order of fully solvated Li_2S_4 , partially solvated Li_2S_4 and non-solvated Li_2S_4 . Thus, the transition from two-plateaued to one-plateaued discharging curves is clarified to change of the solvation state of the Li-PS. At last, the fully solvated, partially solvated, and non-solvated Li_2S_4 were correlated with the design of S-C cathode by the varying pore size of the carbon matrix in the experiment. A new mechanism that nanopores from carbon matrix can create concentrated and partially solvated Li_2S_4 inside was proposed. A synergetic effect of pore size in carbon matrix and salt concentration in the electrolyte in the conversion from two-plateaued and one-plateaued discharging curves was predicted and also confirmed through experiment.

APPENDIX

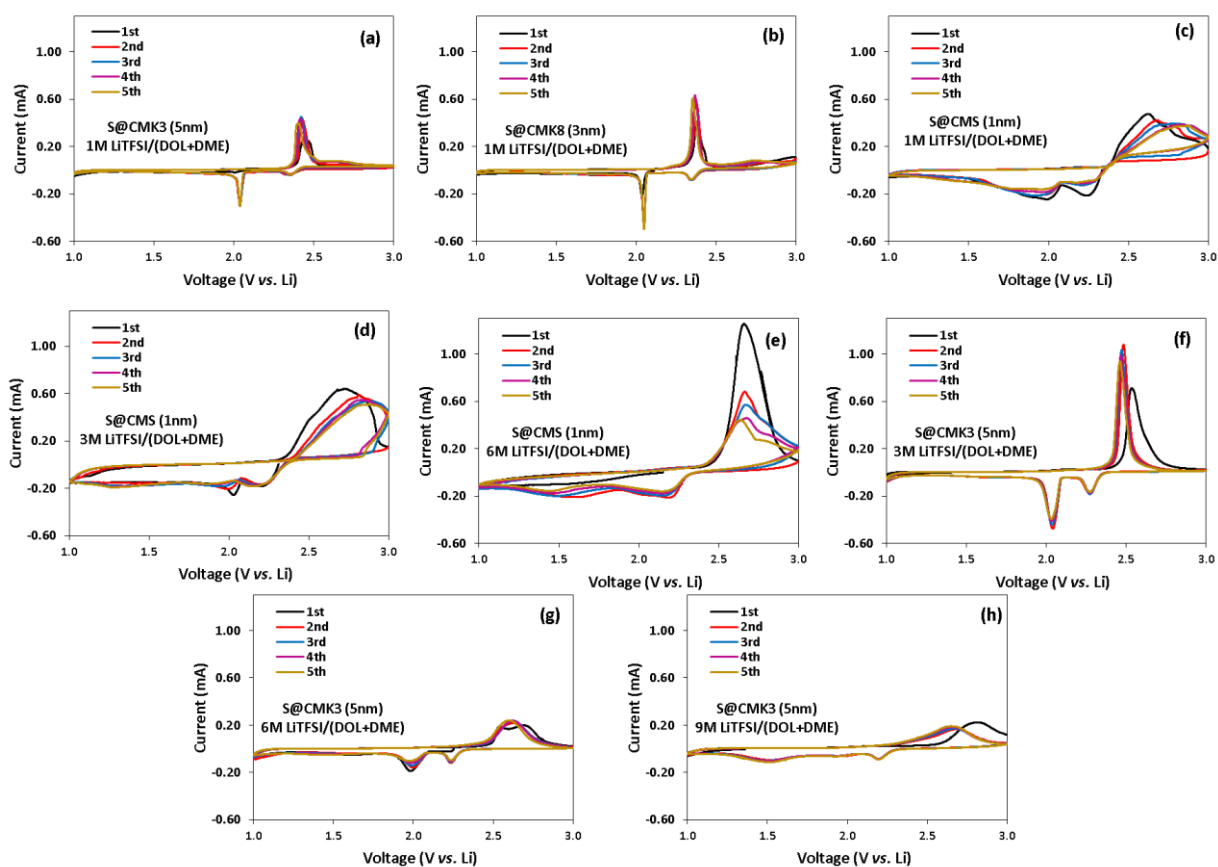


Figure 5.1A Cyclic voltammograms of Li-S batteries at a sweep rate of 0.1 mV/s from 1st to 5th cycle: CV in 1M LiTFSI/(DME+DOL) electrolyte of S@CMK3 (a), S@CMK8 (b) and S@CMS (c) cathode, CV of S@CMS cathode in 3m (d) and 6m (e) LiTFSI/(DME+DOL) electrolyte, and CV of S@CMK3 cathode in 3m (f) and 6m (g) and 9m (h) LiTFSI/(DME+DOL) electrolyte. The pore size of the carbon matrix is also labeled in the parenthesis. (In courtesy of Jing Zheng and Chunsheng Wang from University of Maryland.)

6 S-C cathode design with sub-nanopores: optimum pore size to prevent Li-PS formation

6.1 Summary

Using an integrated DFT-based computational approach followed by experimental validation, carbon nanotube (CNT)/sulfur cathode composites with optimum open ring sizes were designed. By calculating the transport barrier of lithium through open rings in CNTs and comparing the molecular size of selected molecules with the ring size, optimum rings within the range of 16r to 30r were predicted to selectively allow transportation of lithium and sulfur while blocking both polysulfides and electrolyte molecules. The generation of open rings of CNT during the oxidation process was also simulated and analyzed. The results indicated that the optimal open ring size can be achieved by controlling oxidation parameters within a narrow window. Based on the computational prediction, the CNT/S cathode with open rings was synthesized in the experiment by filling sulfur into oxidized CNTs. It was confirmed that optimum open rings were generated in the CNT/S composites oxidized at 750 °C. Through this unique design based on both computational prediction and experimental confirmation, the shuttle of soluble polysulfides was mitigated and an excellent cycling performance could be achieved.

6.2 Introduction

Comparing with Li-ion battery, the two electrons transfer process in Li-S batteries enables a much higher theoretical specific capacity (1675 mAh/g) and energy density (2800 Wh/L) [17][18]. Also, Li-S batteries are considered as green and cheap energy devices due to the abundance of elemental sulfur. Unfortunately, in most liquid electrolytes, the discharging reaction between Li and a-S₈ generates dissolvable long-chain lithium Li-polysulfides (Li-PS), including Li₂S₈, Li₂S₆, Li₂S₄, before the final products, insoluble Li₂S₂ and Li₂S crystals[22][219]. These dissolved long-chain Li-PSs can diffuse between the cathode and the anode and precipitate as the insulating and insoluble Li₂S₂ and Li₂S layer on electrode surfaces, causing severe degradations of the battery, such as loss of active sulfur, low Coulombic efficiency, and capacity decay upon cycling. This so-called “PS shuttle” process, along with insulating nature and large volumetric expansion of sulfur upon lithiation, highly limits the application of Li-S batteries with liquid electrolyte [21].

Carbon-sulfur (S-C) composites as cathode materials are widely used to mitigate these problems. The carbon matrix can improve the conductivity of sulfur and buffer its volume expansion upon lithiation [63]. Furthermore, when sulfur is filled in the porous structure of the carbon matrix and blocked away from the electrolyte solvent, PS shuttle problem can be mitigated [73,220]. Some smallest nano-porous carbon matrixes include 3 nm mesopore carbons [71], 0.5 nm micropore carbons [67] and 5 nm open rings in the walls of CNT [69]. According to our recent prediction, non-solvated Li-PSa were not stable phases comparing to the formation of crystalline Li₂S and S₈ [221]. The generation of Li-PSs was mainly attributed

to the solvation of Li-PSs, as the solvation energy stabilized the Li-PS molecules. Therefore, a critical question remained is what is the optimum pore size in the carbon matrix to block the electrolyte solvent from the discharging reaction. Ideally, during the battery cycling, only lithium Li^+ ions are allowed to transport through the open rings, while the solvent molecules and solvation shells of Li^+ ions are kept out. Therefore, the pore size should be well controlled [70]. Although some previous models have compared the sizes of PS, electrolyte solvent, and pore in carbon matrix [63][91], there was still no clear definition for the optimum pore size, nor the method to control the pore size in the carbon materials.

Among all the carbon matrixes, CNTs offer many advantages as the cathode for Li-S batteries, such as high thermal and electrical conductivities [92,93], good mechanical properties [94], high surface area [95]. In addition, their hollow space inside can also provide good storage of sulfur. In one inspiring experiment by Fujimori [70], the 1D sulfur chain was encapsulated into CNT with 2 nm diameter through the opened caps. DFT calculation supported weak interactions between a- S_8 and CNT, leaving a possibility for sulfur to react with lithium. The opening structures in CNT can be tuned by the oxidation process. Furthermore, the open rings in the walls of the CNTs can increase its size with the level of oxidation [96], change its size and chemistry with the oxidants [97] and temperature [98], and even destroy the CNT structure under a very strong oxidation condition [99]. These experiments suggest that it is feasible to control the size of open rings in CNTs by controlling the oxidation processing conditions.

Therefore, the goal of this paper is to first computationally design the optimum open ring

size in a single wall CNT and then to use the oxidation method to achieve the optimized structure. Both DFT calculations and reactive MD simulations will be performed to simulate the transport and oxidation processes. Only a few similar simulations can be found in carbon systems that are related to the current work. For example, by calculating the transport energy barrier as a function of the pore size from DFT calculation, Zhang *et al.* successfully predicted that the selective transportation provided by the pore structure in graphdiyne and rhombic-graphyne was good for H₂ separation and purification from different gas mixtures [100]. With the aid of MD simulation, Jiao and Xu [101] and Song *et al.* [102] also investigated how gas transportation will be affected by the defects in graphene oxides membranes and coal. MD simulation from Mann *et al.* indicated that the oxidation in CNT proceeded as O₂ adsorption and then O₂ induced degradation, and the nanotube cap is much more susceptible to oxidation [222]. Starting from graphene oxides, Research by Bagri *et al.* on the evolution of open ring structure upon thermal treatment also provide valuable information on the synthesise of porous carbon materials [223]. Inspired by these simulations, this work presents an integrated computational design approach to design CNT-encapsulate-S cathode, which is permeable to Li⁺ ions but not to electrolyte molecules, in order to mitigate polysulfide shuttle problems in Li-S batteries. The evolution of the defect structures and the open ring size will be tracked by reactive MD simulations in order to guide the material synthesis process. Then, experiments were performed to demonstrate the feasibility of synthesizing CNT-encapsulated-S cathodes and their superior cyclability for Li-S batteries.

6.3 Model details

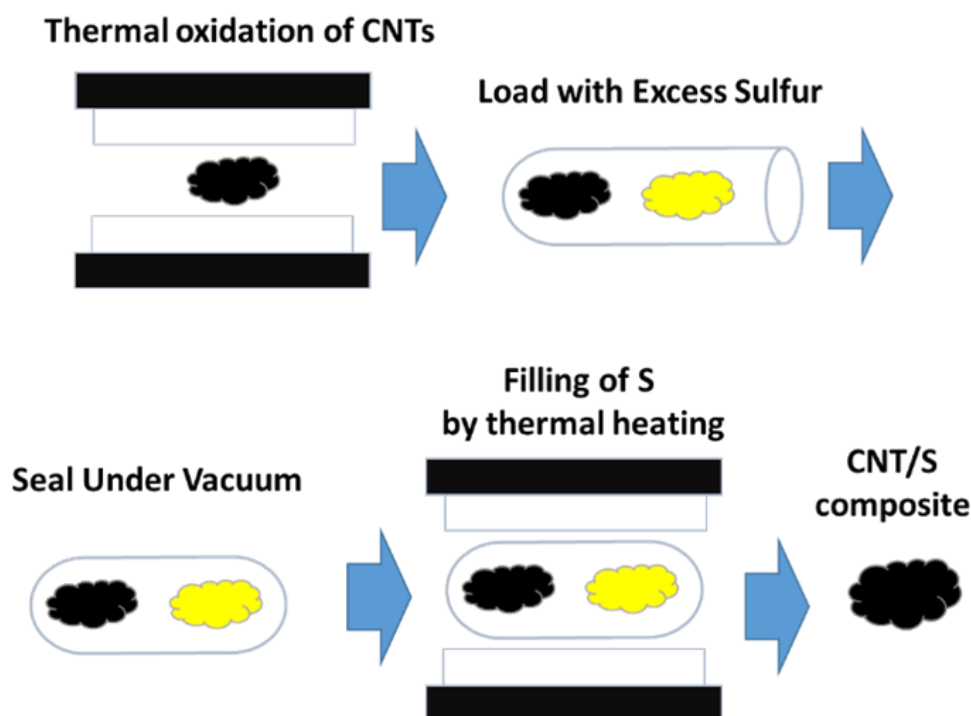


Figure 6.1 Schematic of the synthesis process of CNT-encapsulate-S Cathode.

To achieve the design of synthesizing the CNT-encapsulate-S cathode, we mimic a rather idealized experimental procedure, as shown in Fig 5.1. First, CNT will be oxidized in air to form open rings on the surface, then sulfur will be evaporated into the CNT and be encapsulated. The S-filled-CNT can be washed by solvent then assembled into Li-S batteries for electrochemical measurements. The integrated calculations will design a CNT-encapsulated-S cathode will follow the criteria and corresponding models. a) The optimum open-ring size on CNT should be permeable to Li^+ and evaporated S, but not to solvents, such as DOL and DME. Therefore, the energy barrier (E_b) of Li to transport through the open rings were calculated with DFT. Then, the size of open rings that allow Li^+ transport will be compared with the molecular

size of S₂, DME and DOL solvent, molecular PS to find the optimized range of open-ring size. To determine if the oxidation process will open the rings on CNT to the appropriate size, the reactive force field (ReaxFF) MD was used to simulate the CNT oxidation process in the air at a function of temperature and time. The evolution of the open-ring size will be tracked as a function of oxidation processing parameters.

All DFT calculations were conducted by plane-wave DFT implemented in VASP. Potentials constructed with the full potential projector augmented wave (PAW) method were used for the elemental constituents [187]. The exchange-correlation was treated with the GGA Perdew-Burke-Ernzerhof (PBE) functional [188]. Spin polarization was also included. In each calculation, 700 eV cutoff energy and 1x1x1 Kmesh were chosen to achieve a convergence of 1 meV/atom. The convergence criteria were set to be the energy of 10⁻⁶ eV and the force of 0.02 eV/Å for the electronic and ionic steps in relaxation, respectively.

The CNT oxidation process was simulated by molecular dynamics with the ReaxFF [224] implemented in Lammmps with NVT ensemble. The temperature was controlled by Nosé algorithm [200]. Each calculation was run for 100ps at a time step of 1fs after an initial optimization. A series of NVT ReaxFF MD calculation was conducted to investigate the influence of different parameters on ring size, including oxidation temperature, oxidation time, oxygen/carbon ratio and CNT unit length. To accelerate the oxidation, the MD simulations are run at a higher temperature than that in the experiments.

6.4 Computational results

6.4.1 DFT calculation of Li transport barrier and the minimum open-ring size

To calculate E_b for Li to transport through open rings, one-quarter of a CNT with a diameter of 20 Å was put into a large 30x30x25 Å simulation cell, as shown in Figure 6.2a. To exclude the influence of the CNT caps, an infinite long CNT was realized by a periodic boundary along the CNT axial direction. Open rings of different sizes were first created by deleting the carbon atoms, as shown in Figure 6.2b. Two diameters with a cross angle about 30 degrees were used to characterize the size of the open-rings with an irregular shape. The open-ring size was also characterized by the number of C atoms around the ring. It was also worth note that there may be a different configuration for the number of C atoms when the ring size is large (eg. 18r or above). After the creation of open rings, the edge C atoms shown as blue in Figure 6.2a were fixed, while both Li and other C atoms were allowed to relax.

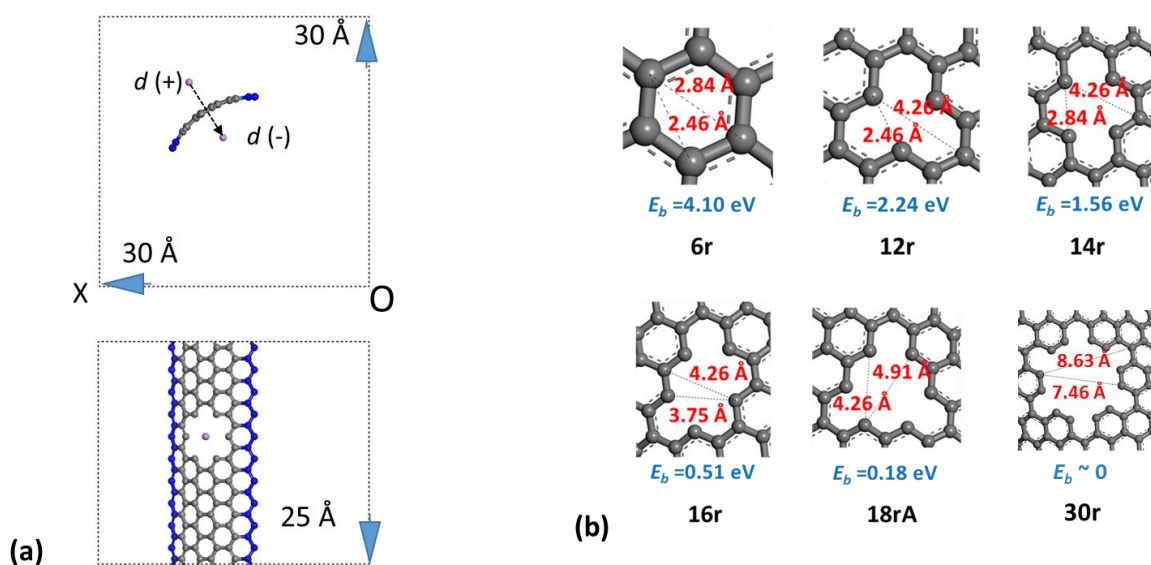


Figure 6.2 (a) Simulation cell used for the DFT calculation of E_b . (b) The configuration of rings with different size. The E_b , the ring size, and the two diameters were also labeled. Li, edge C

atoms with fixed coordination, and other C atoms allowed to relax were represented as purple, blue and grey.

To calculate E_b , the Li atom moves from outside of the CNT through the center of the opening toward the center of CNT, as shown in Figure 2a. The distance between the Li atom and the center of the ring was represented as d . A positive value of d indicated the Li was at the outside of the CNT while the negative value indicated that the Li was inside. The total energy with a d value of -5 \AA was set as a reference state of 0 eV .

To better understand the transport mechanism of Li, two specific cases through the 14r ring and 18rA ring were tracked. The total energy of the configuration and the Bader charge on Li were both plotted as a function of d , as shown in Figure 6.3a and 6.3b. For the 14r ring, the total energy was close to 0 when $d > 1 \text{ \AA}$ or $d < 2 \text{ \AA}$. A peak value of 1.56 eV in the total energy curve was observed with at $d = -0.3 \text{ \AA}$. This high E_b value suggested that the transport of Li through 14r or smaller ring was very difficult. Furthermore, the data points on both sides of the peak agreed well with the binominal fitting trendlines. However, the curvature of the fitting trendlines on the left side was different from that on the right side due to the unsymmetrical configuration of the CNT. This phenomenon could also be seen in the total energy curve for 18rA ring in Figure 6.3a and both curves in Figure 6.3b. For 18rA ring, the total energy curve became much flatter, and the peak observed at $d = -0.5 \text{ \AA}$ dropped significantly to only 0.18 eV . Therefore, it is much likely that Li can transport through the open rings of 18rA.

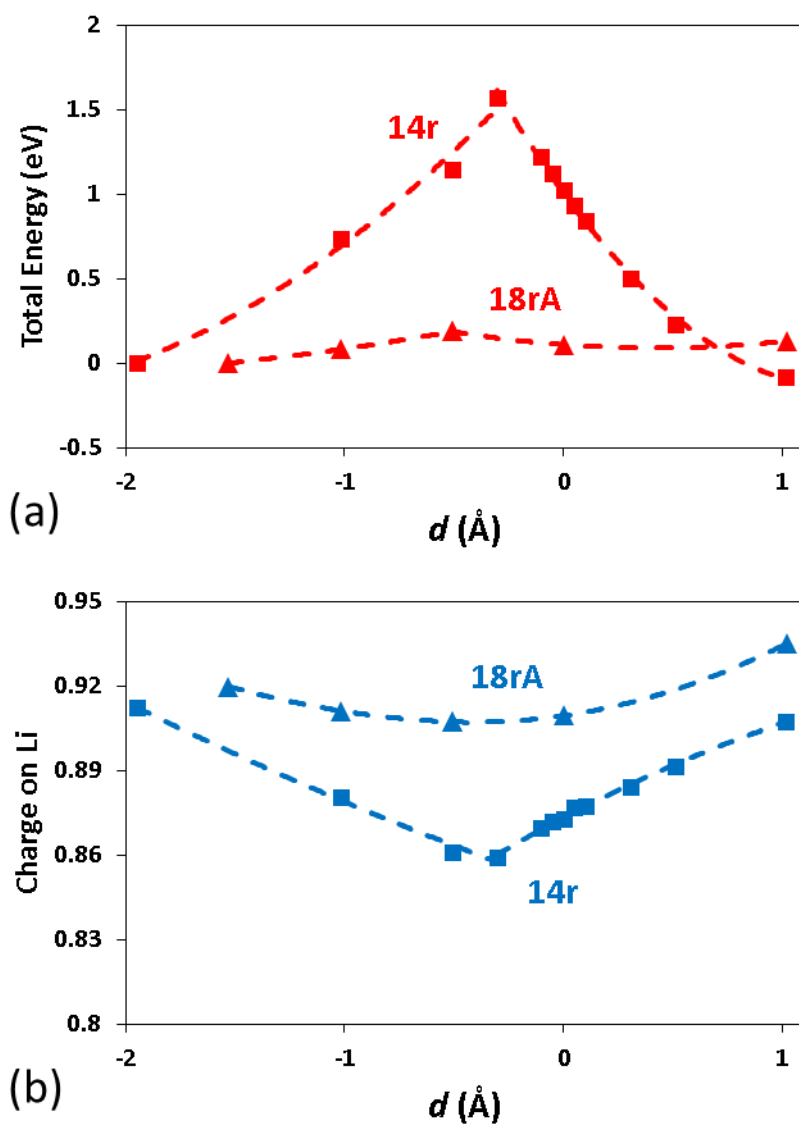


Figure 6.3 The calculated total energy of the configuration and the Bader charge on Li as a function of d for the 14r ring (a) and 18rA ring (b). Binomial trendlines were used to fit the data points.

A more detailed mechanism can be revealed by analyzing the Bader charge on the Li. As shown in Figure 6.3b, the charge on Li was above 0.9 for both 14r and 18rA ring, when $d > 1$ Å or $d < -2$ Å. This was consistent with our common understanding that lithium atom tended to lose its only valance electron easily and became Li⁺ ion. For the 14r ring, the Bader charge on lithium-ion dropped dramatically by 0.05 when d approached 0. This indicated a strong

electrostatic interaction between Li^+ and the negatively charged ring. These configurations were highly unstable, leading to a large E_b for the 14r ring. As a comparison, for the 18rA ring, the charge on Li decreased only by 0.01 when d approached 0. This indicated the interaction between Li^+ and the ring was very small even when d approached 0 since the distance between Li and C was far enough. Thus, a lower E_b was expected.

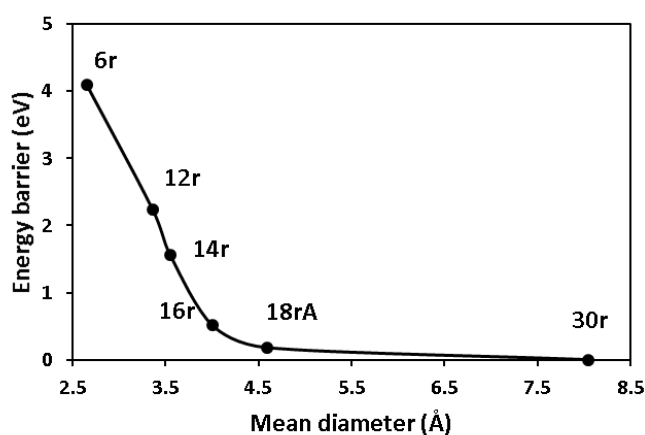


Figure 6.4 E_b summarized as a function of the mean diameter of the open ring.

The calculated E_b for each ring size was labeled in Figure 6.2b and summarized as a function of the mean diameter in Figure 6.2d, with ring size labeled. Very large E_b was observed for small rings. For a 6r ring in pristine CNT with a mean diameter of 1.4 Å, E_b was as high as 4.1 eV. Even for a 12r or 14r ring in a defected CNT with a mean diameter around 3.5 Å, E_b was still larger than 1.5 eV, which were too high for Li transportation. Fortunately, E_b decreased with the increasing mean diameter and ring size. When the mean diameter was larger than 4 Å, the E_b was only 0.51 eV for the 16r ring and 0.18 eV for 18rA ring. Assuming 0.6 eV energy barrier was set as the criterion for Li transportation through open rings, it can be concluded that Li can transport through rings larger than 16r, but cannot transport through rings smaller than

14r. Therefore, 16r or larger rings on CNT was required for Li to transport into CNT.

6.4.2 Comparison of molecular sizes and the maximum open-ring sizes

The molecular size of Li atom, Li-ion, electrolyte solvent (DOL and DME) and the smallest polysulfides Li_2S_4 were calculated and compared with the diameter of the 18rA ring, as shown in Figure 6.3a. All the molecules were also minimized by DFT calculations. An isosurface with an electron density of 0.017 and 0.2 electrons/ \AA^3 for molecules and crystals, respectively [184] was plotted along with the relaxed molecules. The molecular size was determined as the longest dimension within the isosurface. The electron density of the 18rA ring in the infinite long CNT was also plotted. The as-determined molecular sizes were compared with the size of open rings to determine the maximum open-ring size.

Considering the volume of the electron cloud, the size of the Li atom was $\sim 3 \text{ \AA}$. The size decreased to $\sim 2 \text{ \AA}$ when it lost the valence electron and became Li-ion. Considering the electron cloud of carbon atom in CNT would contribute another 1 \AA inside the ring, as shown in Figure 6.3a, it required an open ring with a diameter of $\sim 4 \text{ \AA}$ for Li atom to transport. This was in good agreement with the predicted open ring size through the calculation of E_b .

The open rings should also be large enough for the S_2 gas to fill the CNT. According to the S phase diagram [63], the cyclo- S_8 crystal was dissociated into short chains allotropes in highly mobile vapor state starting at 720 K. Thus, the smallest S allotrope S_2 was also included in Figure 6.3a. It can be seen that the size of the S_2 molecule was less than 4 \AA , which was close to that of the Li atom. Therefore, the diameter of the open rings must be larger than $\sim 4 \text{ \AA}$.

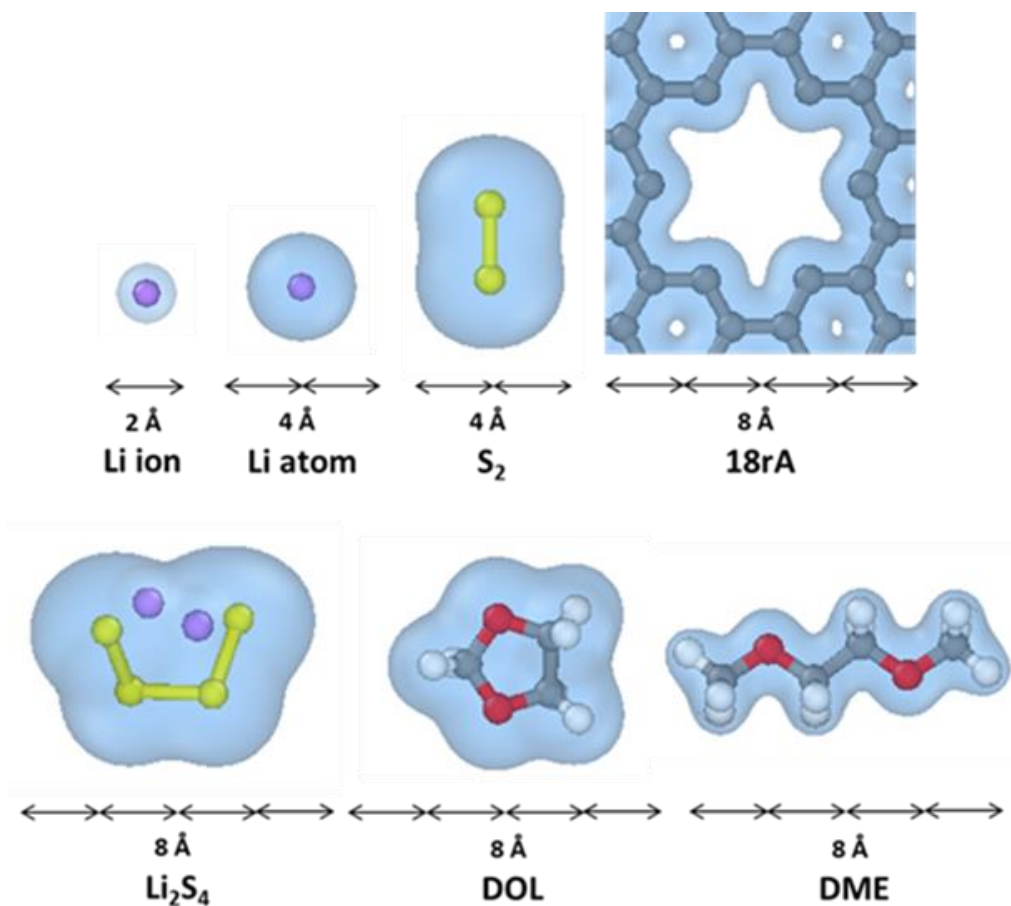


Figure 6.5 Comparison of molecular size of Li-ion, Li atom, S₂, Li₂S₄, DME and DOL with 18rA ring. The Li, S, C, H, and O are represented as purple, yellow, grey, white and red, respectively.

6.4.3 Stable ring size achieved by oxidation of CNT simulated by ReaxFF MD

Open rings can be generated by oxidation induced degradation [222] of CNT, in the assistance of H₂ or H₂O. Therefore, epoxy and hydroxyl groups were added to the infinitely long CNT used in MD calculation. The CNT diameter for computational work is X, comparable with the experimental dimension of 1.0-1.4 nm. The ratio between epoxy and hydroxyl groups

were fixed at 2:3, the same as the initial configuration of graphene oxide used by Bagri [223]. The configuration that a hydroxyl group bonded to a carbon atom was accompanied by an epoxy group bonded to a neighboring carbon atom was also kept. The open-ring structure on CNT was tracked during each MD simulations. To determine the ring size, default bond length was set to be 1.7 Å (a little larger than the 1.7 Å C-C bond in CNT). The open-ring sizes were also determined by counting the number of connected atoms (both O and C) surrounding the ring. Discontinuous atoms in branches or without connections to other atoms were not included.

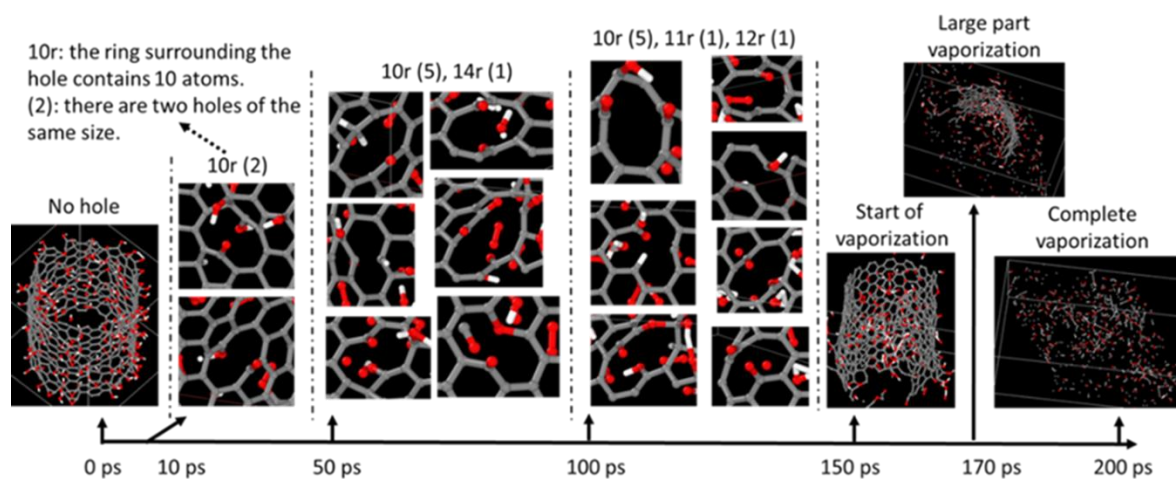


Figure 6.6 The oxidation process of CNT with O:C ratio 1:3 at 1000K. The C, O, and H were represented as grey, red and white, respectively.

Figure 6.6 shows the snapshots at different time step during a representative NVT simulation to represent the evolution of the open-ring structure in the oxidation process. The O/C ratio was set to be 1:3 and the simulation temperature was 1000K. The original configuration after optimization was shown at 0 ps in the time scale. All rings were still 6r, same as the pristine CNT. As the oxidation process proceeds, both the number and the size of open rings (rings larger than 6r) increased. For example, there were only 2 open rings with size

10r at 10 ps. But at 100ps, there were 6 rings in total and the largest ring size increased to 14r. After 150 ps, large parts of carbon atoms were already destructed by open-ring coalescence, causing huge rings in CNT. Shortly after that, all the CNT became vaporized at 200ps, indicating that the structure with huge rings was highly unstable. This was consistent with the observation that the destruction of CNTs started from the generated open rings under a strong oxidation condition [99]. Most atoms in the open-rings were still pure carbon and only less than 30% of them were attached to oxygen or hydrogen. This validated the choice of the pure CNT for E_b calculations in 3.1, which had shown that the E_b for Li transport through the open-ring decreased with increasing size. This indicated that it is reasonable to just count the largest open-ring to judge if the open-ring is permeable to the electrolyte and if the CNT is structurally stable.

To further determine the influence of different oxidation parameters on the size of rings generated in the oxidation process, a series of NVT MD simulation with various oxidation temperature, oxidation time, oxygen/carbon ratio, and the periodic CNT length were conducted.

By investigating the structure evolution in MD trajectories (like the one shown in Fig 6), the largest ring sizes at a specific time under different oxidation conditions were tracked and summarized in Table 1. It is found that all four conditions influence ring size evolution. Apparently, higher temperature and more oxygen will accelerate the ring opening process. When the CNT oxidized at 1000 K and an O:C ratio of 1:3, the CNT with a periodic length of 24.6 Å was destructed at 150 ps with the largest open ring size of 14r. The destruction of this CNT would be delayed to 220 ps when it was oxidized at 800 K, and the largest open ring size

before destruction was 12r. When it was oxidized at 1300 K, the destruction of the CNT structure was accelerated to 50 ps, and the largest open ring size before destruction was 10r.

Table 6.1 Largest ring size created in each simulation case

O:C ratio	T (K)	Periodic CNT length (Å)	10ps	50ps	100ps	200ps	500ps	1000ps
1:6	800	24.6	12	12	12	12	11	11
1:6	800	49.2	12	12	15	15	15	Destruct at 670 ps
1:6	800	73.8	14	14	18	14	Destruct at 390 ps	
1:6	1000	24.6	12	14	14	14	14	14
1:3	800	24.6	11	11	11	Destruct at 220ps		
1:3	1000	24.6	10	14	12	Destruct at 150ps		
1:3	1000	49.2	17	18	Destruct at 55 ps			
1:3	1000	73.8	14	14	14	20	Destruct at 250 ps	
1:3	1300	24.6	10	Destruct at 50ps				

When the O:C ratio decreased to 1:6, the CNT (with a periodic length of 24.6 Å) structure was maintained without collapsing after 1ns simulation time at both 800 K and 1000 K, and the largest open-ring size was 12r at 800 K and 14r at 1000 K. This suggested that a mild oxidation environment was more preferred. Therefore, to obtain an optimum open-ring size distribution without destroying the CNT structures, a temperature, oxygen pressure, and time window need to be controlled carefully.

As the CNT is destroyed by open-ring coalescence, the randomly distributed open-rings in the simulation cell would interact with their periodic images in the simulation. Therefore the periodic length of CNTs also played a role in the oxidation process. Generally, increasing the periodic length, will accelerate the process of destroying the CNT, expect in the case with the CNT at the periodic length of 73.8 Å at 1000 K and an O:C ratio of 1:3. This may be related to

the rapid desorption of oxygen groups under high temperatures, in which the amount of O absorbed to CNT decreased. Although the periodic length study is mainly an artifact of the atomistic model, it does shine some light on the general trend observed in the MD simulation.

These simulations confirmed that the oxidation process of CNT can generate open rings on the walls of CNT. But after a long oxidation time, the CNT structure will be destructed. It was also found that the largest open-ring size before CNT destruction was 10~20r, in a broad range of oxidation conditions. This means the optimum ring size predicted in DFT calculation can be generated by oxidizing long CNTs in a mild oxidation environment with an optimum temperature range. According to our simulation, Jeremy Ticey and John Cumings from University of Maryland further synthesized the CNT/S cathode with optimum ring size by controlling the oxidation parameters of CNT, and tested the electrochemical performance.

6.5 Conclusion

With an integrated computational approach, the CNT/S-based cathode with optimum open ring size was designed. By calculating the transport barrier of Li through open rings in CNT, and comparing the molecular size of selected molecules with the ring size, optimum rings within the range of 16r to 30r were predicted to selectively allow transportation of Li and S while blocking both polysulfide and electrolyte. The generation of open rings of CNT during the oxidation process was also simulated and analyzed. The results indicated that the optimal open ring size can be achieved by controlling oxidation parameters within a narrow window. Through this unique design, the dissolution problem of polysulfide was mitigated and an excellent cycling performance was achieved.

7 Improvement of Li transport property of concentrated low-temperature electrolyte by adding co-solvent

7.1 Summary

The highly concentrated electrolyte can achieve the partially solvated Li-PS, and even expand the electrochemical stability window of the electrolyte if an SEI is formed. However, its high viscosity results in very slow Li transport, which became more severe at low temperature. Recently, a co-solvent electrolyte was designed by adding electrochemically stable dichloromethane (DCM) to highly-concentrated ethyl acetate(EA)-based electrolyte. In this chapter, the solvation structure in the co-solvent electrolyte was determined as clusters of partially solvated Li^+ , TSFI, and EA network surrounded by the DCM from MD simulation. DFT calculation showed that former inherited the expanded electrochemical window of the highly-concentrated salt, and the MD simulation confirmed that the latter accelerated the Li transport at both room temperature and low temperature.

7.2 Introduction

Commonly used lithium-ion batteries (LIBs) lost most of the capacities at the temperature of $-40\text{ }^\circ\text{C}$, hindering a broad range of applications at low temperatures [225,226]. One of the main reasons was the increased viscosity and decreased ionic conductivity of the liquid electrolyte at lower temperatures.

Solvents with high freezing points, such as ethylene carbonate (EC, $35\sim 38\text{ }^\circ\text{C}$) were often

used in the commercial electrolytes, resulting in the poor low-temperature performance of rechargeable LIBs [227]. Although new solvents of liquefied gas electrolytes enabled electrochemical energy storage devices to operate at $-60\text{ }^{\circ}\text{C}$, high-pressure stainless-steel cells were required to condense the typical gaseous state under standard conditions into liquid [227]. An alternative solvent, ethyl acetate (EA), with a much lower freezing point of $-84\text{ }^{\circ}\text{C}$ than the commonly used carbonate solvents enabled LIBs performance improvements at a low temperature of $-70\text{ }^{\circ}\text{C}$ [109]. Unfortunately, the full cell delivers low specific energy of 33 Wh/kg due to the limited electrochemical stable window from 1.5 V to 4.7 V (vs. Li^+/Li) at a concentration of 2 mol/kg. Thus, the EA-based electrolyte is far from being compatible with lithium metal anode, although it is desired to further increase the energy density of LIBs, owing to its high gravimetric capacity (3863 mAh/g) and high reduction potential (-3.04 V vs. standard hydrogen electrode). Therefore, developing a novel electrolyte composition with enhanced stability with Li metal anode was an efficient approach to achieving an improved energy density of rechargeable battery at low temperature.

Highly concentrated electrolytes exhibited unique characteristics, such as enhanced oxidative/reductive stability, unique solvation structures, and functionalities [104–106]. However, concentrated electrolyte also faced challenges of narrower liquid range, lower ion conductivity, and higher viscosity, all of which became more severe at low temperatures. Therefore, introducing an “inert” diluent solvent to lower the viscosity of concentrated electrolyte would be an effective approach to overcome these shortcomings. A proper diluent can certainly lower the viscosity. The challenging requirement is that it should have little or no

impact on the solvation structure of cation-anion aggregates (AGGs), which are responsible for the expanded stability window in the concentrated electrolyte [228]. Meanwhile, it is more desirable if the diluent can also increase the conductivity and improve the wettability of the electrolyte.

Dichloromethane (DCM, CH_2Cl_2), an electrochemically “inert” and poorly solvating solvent, has a low viscosity of 0.44 mPa/s, which can well meet these requirements [229]. In addition, the freezing point of DCM is as low as $-97\text{ }^\circ\text{C}$, which facilitates the operation of rechargeable batteries at a low temperature. Recently, a new co-solvent electrolyte was synthesized by adding DCM to concentrated EA-based electrolyte. The co-solvent electrolyte can maintain the expanded stable potential window of the concentrated EA-based electrolyte and circumvented its shortcoming of high viscosity. Based on this electrolyte, a rechargeable battery using organic polymer materials polyimide cathode and metallic lithium anode delivered a high specific energy of 178 Wh/kg and high specific power of 2877 W/kg (based on the total mass of active materials in cathode and anode) displayed excellent performance at the ultra-low temperature of $-70\text{ }^\circ\text{C}$. However, the working mechanism of the co-solvent electrolyte was still not well understood.

In this chapter, experimental results on the co-solvent electrolyte were first summarized. The solvation structures in both EA-based electrolyte and co-solvent electrolyte were then determined with MD simulation. The influence of the solvation shell on the Li-transport property was investigated by calculating the Li diffusion coefficient from the MD simulation. Through density functional theory (DFT) calculation, the influence of the solvation structure

on the electrochemical window was also investigated.

7.3 Summary of experimental results

Experiments in this part were done by Xiaoli Dong and Yongyao Xia from Dudan University. EA-based electrolytes were prepared with Li salt (LiTFSI, lithium bis(trifluoromethanesulfonyl) imide) in solvent EA. Their name 1m, 2m, and 5m stood for their concentration of 1 mol/kg, 2 mol/kg, and 5 mol/kg, respectively. The co-solvent electrolytes were prepared by adding DCM to concentrated 5m EA-based electrolyte. Their name 5m-1-1, 5m-1-4 and 5m-1-8 indicated the volume ratio of 5m EA-based electrolyte and the DCM were 1:1, 1:4 and 1:8, respectively.

The experimentally measured viscosity and ionic conductivity at both 25 °C and -70 °C were listed in Table 7.1. For EA-based electrolyte 1m and 5m, the viscosity increased with increasing concentration at both temperatures. Fortunately, the viscosity decreased when more DCM was added to the electrolyte in 5m-1-1, 5m-1-4, and 5m-1-8. Furthermore, while the viscosity of both EA-based electrolyte and co-solvent electrolyte increased when temperature decreased from 25 °C to -70 °C, the increase in co-solvent electrolytes was less than that in 5m EA-based electrolyte. The less increase of viscosity at a lower temperature demonstrates the benefit from the introduction of DCM diluent. The ionic conductivity of 5m EA-based electrolyte was 3 mS cm⁻¹ at room temperature, but only 0.01 mS cm⁻¹ can be obtained at -70 °C. The addition of DCM can effectively accelerate the ionic movement and improves the ionic conductivity at -70 °C. The 5m-1-4 electrolyte displayed the best conductivity among all these electrolytes at -70 °C. The freezing points were also listed in the last column in Table 7.1. The

addition of DCM can further decrease the freezing point of 5m EA-based electrolyte. Thus, co-solvent electrolyte was suitable for use in low temperature of -70 °C .

Table 7.1 Physical properties of various electrolytes with different compositions. (Copy right from Angewandte Chemie International Edition 2019.)

Electrolyte composition	Density (Experimental) (g/cm ³)	Viscosity (mPa/s)		Ionic Conductivity (mS/cm)		Freezing point (°C)
		+25 °C	-70 °C	+25 °C	-70 °C	
1m	1.03	0.22	30.57	8.93	1.37	-88
2m	1.20	2.66	614.38	2.20	0.19	-91
5m	1.39	14.99	106680	3.02	0.01	-102
5m-1-1	1.32	3.88	768.70	2.71	0.36	-103
5m-1-4	1.33	1.24	351.43	1.48	0.60	-104
5m-1-8	1.33	0.03	5.35	0.53	0.25	-107

The Raman spectra in all electrolytes, pure EA and DCM solvents and LiTFSI crystal were shown in Figure 7.1a. Pure EA solvents exhibited an absorption peak at 848 cm⁻¹. For EA-based electrolyte, this peak gradually shifted to 854 cm⁻¹ with increasing concentration. After adding DCM, the peak at 854 cm⁻¹ was also maintained. These indicated that more EA interacted with Li-ions with in concentrated EA-based electrolyte and co-solvent electrolytes. Furthermore, another peak at 749 cm⁻¹ was observed for both the 5m EA-based electrolyte and co-solvent electrolytes, which were identical to that from LiTFSI crystal. This suggested that the solvation structure is close to the crystal structure of LiTFSI. Meanwhile, the signal at ~283 cm⁻¹ and 703 cm⁻¹ of C-Cl in DCM appeared no obvious change, proving the inert properties of diluent DCM.

The linear scan voltammetry (LSV) of 1m and 5m EA-based electrolyte were shown in Figure 7.1b. It can be detected that the 5m electrolyte effectively decreased the reduction

potential and increased the oxidation potential, leading to an extended stable electrochemical window at both sides. The extended window of 0~4.85V can also be maintained for 5m-1-4 co-solvent electrolyte, as shown in Figure 7.1c.

Polytriphenylamine (PTPAn, a p-type polymer that depends on doping/de-doping mechanism), were chosen as cathode owing to the fast kinetics of charge stored on the surface groups or in the large interstitial space [12]. As displayed in Figure 7.1d, Li//PTPAn battery can exhibit a discharge capacity of 88 mAh/g with the rate of 0.2C at -70 °C. The corresponding capacity retention is as high as 82% compared with the performance at room temperature of +25 °C. Rate and cycle performance of Li//PTPAn battery was presented in Figure 7.1e. According to the Ragone plot in Figure 7.1f, even at -70 °C, the battery can obtain specific energy of 30 Wh/kg at the specific power of 7 W/kg, and still keeps 5 Wh/kg at the highest power density of 150 W/kg.

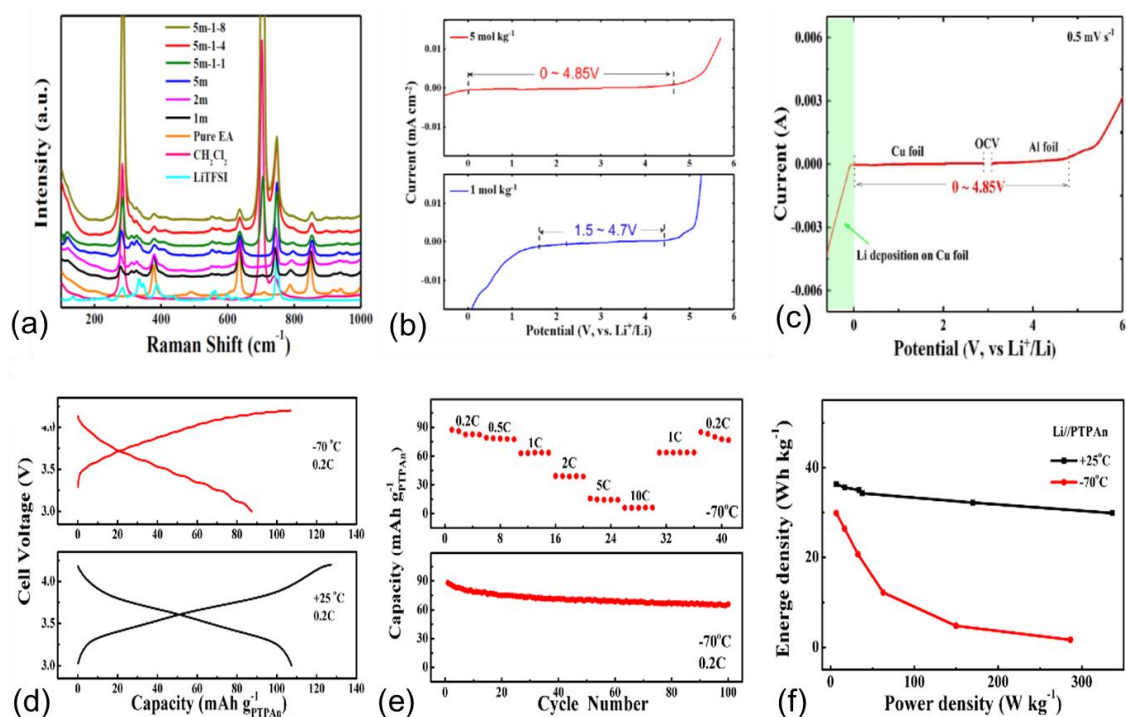


Figure 7.1 Raman spectra (a) in all electrolytes, pure EA and DCM solvents and LiTFSI crystal. Linear scan voltammetry (LSV) of 1m and 5m EA-based electrolytes (b), 5m-1-4 cosolvent electrolytes (c). The LSVs were measured with a three-electrode system in which Pt plate, Pt plate and Li metal were used as working, counter and reference electrodes, respectively. The scan rate was set as 0.5 mV/s. Charge-discharge at +25 °C and -70 °C (d), Rate and cycle performance at the ultra-low temperature of -70 °C (e), Ragone plots at +25 °C and -70 °C (f), of the Li-PTPAn battery. ((Copy right from Angewandte Chemie International Edition 2019.)

7.4 Model details

7.4.1 DFT calculation

Density function theory (DFT) calculation was performed to obtain the binding energy, highest occupied molecular orbital (HOMO) and lowest unoccupied molecular orbital (LUMO). A spin-polarized, all-electron, local (Double Numerical plus polarization, DNP) basis set DFT [183] implemented in Dmol³ [184] module in Materials Studio was used. The exchange-correlation was treated with the generalized gradient approximation (GGA) Perdew-Wang-91

functional [185]. Only the ion positions were relaxed during an energy minimization, until one of the three convergence criteria, as 3×10^{-4} eV/system, $0.05 \text{ eV}/\text{\AA}$, and 0.005\AA for energy change, force, and displacement, respectively, was reached. To ensure the configuration of lowest energy, geometry optimization was conducted with several different initial configurations and the optimized configuration with the lowest energy was selected.

7.4.2 MD simulation

Classical MD simulation was used to investigate the solvation structure of electrolyte with various concentrations. First, an amorphous cell was constructed with randomly packed LiTFSI, EA and DCM with a certain ratio. The solution structure was then optimized with the compass force field [199]. The force field types and the atomic charges are as follows: c112 (-0.16) for Cl, h1 (0.053) for H, f13 (0.615) for F, li+ (1.00) for Li, n2- (-0.77) for N, s4= (1.12) for S, c4 (0.615) for C in LiTFSI, c4x (0.214) for C in DCM, c3' (-0.562) for C in C=O bond in EA, c4o (-0.054) for C in CH₂ group in EA, c4 (-0.562) for C in CH₃ group in EA.

The optimized cell was first subjected to a classical MD simulation with NPT (constant temperature and constant pressure) ensemble at 298K. The converged density, calculated as the average density of the last 50 ps, was listed in Table 7.2. The solvation shell structure of Li was determined by analyzing the radial distribution function (RDF) and the coordination number (CN) in the MD trajectory of the last 50 ps. After determining the density of each electrolyte solution with the NPT ensemble, another classical MD simulation with NVT (constant volume and constant temperature) ensemble at 298K was run for to investigate the diffusion of Li in each electrolyte. For EA based electrolyte, the NVT simulation time was set to be 100 ps with

the mean-squared displacement (MSD) tracked. For co-solvent electrolytes, the NVT simulation time was set to be 200 ps due to more complicated diffusion, and the MSDs are tracked during the last 100 ps to avoid short time regions when molecules are confined. By tracking the mean squared displacement (MSD) as a function of time interval τ , the diffusion coefficient can be represented as:

$$D = \frac{1}{6N_a} \lim_{\tau \rightarrow \infty} \frac{d}{d\tau} \sum_{t=0}^{t-\tau} \sum_i^{N_a} [r_i(t+\tau) - r_i(t)]^2 = \frac{1}{6} \lim_{t \rightarrow \infty} \frac{d}{dt} MSD(\tau) \quad (7.1)$$

in which t is the simulation time, $r_i(t+\tau)$ and $r_i(t)$ is the position of atom i at time $t+\tau$ and time t .

Table 7.2 Calculated properties and Li⁺ diffusion coefficient in the electrolytes, compared with commonly used ethylene carbonate (EC) solvent. A cutoff distance of 2.5 Å was used for CN of Li-O, and a cutoff distance of 4.5 Å was used for CN of Li-N.

Electrolyte composition	N(Li): N(EA): N(DCM)	CN			N(free EA): N(Li)	Calculated Density (g/cm ³)	D (Li ⁺)	
		Li-O (EA)	Li-O(TFSI)	Li-N(TFSI)			+ 25 °C	- 70 °C
0m (pure EA)	0:100:0	/	/	/	/	0.89	/	/
0.15m	6:100:0	4.5	1.1	0.7	62	0.9	/	/
1m	30:360:0	3.5	1.9	1.4	8.5	1.03	3.0	0.3
2m	60:330:0	2.9	2.4	1.7	2.6	1.20	0.9	0.1
5m	120:270:0	1.7	2.9	2.2	0.6	1.45	0.4	~0.03
5m-1-1	40:90:220	1.6	2.9	2.1	0.7	1.39	3.0	0.3
5m-1-4	8:18:176	1.7	3.2	2.4	0.6	1.37	6.8	2.0
5m-1-8	8:18:352	1	2.8	1.7	1.3	1.27	8.3	3.1
Comparison	N(Li): N(EC): N(DCM)	CN			N(free EA): N(Li)	Calculated Density (g/cm ³)	D (Li ⁺)	
		Li-O (EA)	Li-O(TFSI)	Li-N(TFSI)			+ 25 °C	- 70 °C
LiTFSI	/	/	4	2		1.25	/	/
0.15m (EC)	6:100:0	5.3	0.1	0.1	62	1.30	/	/

All the classical MD simulations were done through forcite modulus in Materials Studio.

The timestep was set to be 1 fs. The temperature was controlled by Nosé algorithm [200] and the pressure was controlled by Berendsen algorithm [201]. An Ewald summation was used for the electrostatic interaction, and the Van der Waals interaction was truncated at 18.5 Å.

7.5 Results

7.5.1 Li binding energy

To investigate the interaction between Li⁺-ion and TFSI⁻ anion, EA, DCM, the binding energies calculated from both DFT and MD were listed in Table 7.2. The binding energy in Li⁺·(DCM) was only -1.23 eV, which is much smaller than other solvent species. This indicated weak interaction between DCM co-solvent and Li-ion. The solvent and anion interaction with Li⁺ cation can be ranked in the following order: TFSI⁻ > EA > DCM. It corresponds well with the binding energies from MD calculation, verifying the validity of the force field.

Table 7.3 Summary of binding energy for Li⁺ with different species.

	LUMO (eV)	HOMO (eV)
LiTFSI	-5.87	-5.26
Li ⁺ ·(DCM)	-1.23	-1.08
Li ⁺ ·(EA)	-2.07	-1.78
Li ⁺ ·(2EA)	-3.77	-2.84
Li ⁺ ·(3EA)	-4.78	-3.84
Li ⁺ ·(4EA)	-5.57	-4.76

7.5.2 Solvation structure

The solvation structure of four EA-based electrolytes (0.15m, 1m, 2m, and 5m) and three co-solvent electrolytes (5m-1-1, 5m-1-4 and 5m-1-8) were investigated using classical MD

simulations. As a comparison, pure EA solvent and 0.15m commonly used LiTFSI/EC electrolyte³⁰ were also simulated. The composition of each electrolyte, together with the coordination number (CN) was listed in Table 7.2. The calculated density of the electrolytes accorded well with experimental values in Table 7.1, which further validated the accuracy of the MD method.

The snapshot of the MD simulated electrolyte structure of 0.15m EA-based electrolyte was shown in Figure 7.3a. Li-ions were solvated by both the TFSI⁻ and EA. More details can be found in the corresponding plot of coordination number (CN) as a function of the cutoff distance, which was shown in Figure 7.3b. The CN of both Li-O (EA) and Li-O (TFSI) shared the first step at around 2 Å, indicating that Li-ions interacted with both EA and TFSI⁻ anions in the first solvation shell. Within a cutoff distance of 2.5 Å, each Li is solvated by 4.5 O(EA) and 1.1 O(TFSI). The total CN of Li-O is similar to the commonly used organic EC-based solvents³⁰. Since the N atom was the center atom in TFSI⁻, CN of Li-N (TFSI) was also plotted to account the number of TFSI⁻ around Li. The step around 3.5 Å suggests that O atoms served as bridges connecting Li-ions and N (TFSI). Within a cutoff distance of 4 Å, the CN of Li-N(TFSI) is 0.7. This is quite different from that in 0.15m EC electrolyte, in which Li⁺ is mostly solvated by O(EC) with almost no coordination with TFSI⁻. This difference can be attributed to the less polarized property of EA (permittivity 6) comparing with EC (permittivity 90).

When the concentration of EA-based electrolyte to 5m, an aggregated network was formed involving Li-ions, EA and TFSI⁻, as shown in the snapshot in Figure 7.3c. Even though the steps of the Li-O (EA), Li-O (TFSI) and Li-N (TFSI) in the CN plot of Figure 7.3d still

remained the same position compared with that in Figure 7.3b, the CN value showed dramatical change. The CN of Li-O (TFSI) and Li-N (TFSI) increased to 2.9 and 2.2, while the CN of Li-O (EA) dropped to 1.7. That indicated more TFSI⁻ appeared in the first solvation shell of Li-ions. The snapshot of 1m-1-4 co-solvent electrolyte was shown in Figure 7.3e. Comparing with the aggregated network in Figure 7.3c, clusters formed by Li-ions, EA and TFSI⁻ were now surrounded by the co-solvent DCM. This can be further supported by the CN in Figure 7.3f. First, there were no steps for the CN of Li-Cl with in 3 Å. Thus, DCM did not participate in the first solvation shell of Li-ion. The CN of Li-O (EA), Li-O (TFSI), and Li-N (TFSI) were 1.7, 3.2, 2.4, respectively. These values were very close to that in 5m EA-based electrolyte, indicating the first solvation shell of Li-ions did not change after addition of DCM.

As a summary, the calculated CN of Li-O (EA), Li-O (TFSI), and Li-N (TFSI) in different electrolytes were listed in Table 7.2 and also plotted in Figure 7.4a. To better understand the solvation status of EA molecules, the ratio between the amount of free EA molecules and Li-ions were also included. The increase in the concentration of EA-based electrolyte increases the CN of Li-O (TFSI), and Li-N (TFSI) and decrease the CN of Li-O (EA). The ratio between free EA molecules and the Li ions, $N(\text{free EA}):N(\text{Li})$ also decreased rapidly with increasing concentration. After adding DCM, only small fluctuation can be observed for the CN of Li-O (EA), Li-O (TFSI), and Li-N (TFSI), and a low value of $N(\text{free EA}):N(\text{Li})$ was kept in 5m-1-1, 5m-1-4, and 5m-1-8.

7.5.3 Diffusion coefficient

The diffusion coefficient of Li⁺ ions was calculated by tracking the mean-squared

displacements (MSD) of Li^+ in the various electrolytes as a function of time interval τ in the NVT (constant volume and constant temperature) simulation. The linear fitting to a time interval of 50 ps (was chosen to calculate the diffusion coefficient, as shown in Figure 7.4b for +25 °C and Figure 7.4c for -70 °C, respectively). The calculated Li^+ diffusion coefficients in the electrolytes were summarized in Table 7.2. It can be found that the diffusion coefficient of Li^+ in the 5m electrolyte is only 10% compared to that of the 1m electrolyte at +25 °C, owing to the formation of AGGs and lack of free EA. Fortunately, the diffusion coefficient has been dramatically increased by about 7.5 times in 5m-1-1 with the introduction of diluent DCM. More diluent led to faster ion transport for 5m-1-4 ($6.8 \times 10^{-6} \text{ cm}^2/\text{s}$) and 5m-1-8 ($8.3 \times 10^{-6} \text{ cm}^2/\text{s}$) co-solvent electrolytes. At -70 °C, for 5m-1-1, only 10% of the diffusion coefficient at +25 °C is maintained. This low-temperature diffusion coefficient retention increased to 29% for 5m-1-4 and 37% for 5m-1-8 co-solvent electrolytes. The diffusion coefficient of Li^+ in 5m-1-4 still kept at high value of $0.8 \times 10^{-6} \text{ cm}^2/\text{s}$ (Figure 3d). The structure and transport mechanisms indicated that 5m-1-4 co-solvent electrolyte inherited the solvation structure from high concentration electrolyte and fast ion transport resulting from the diluent DCM, which enabled its unique characteristic for the application in rechargeable Li-metal battery at low temperatures.

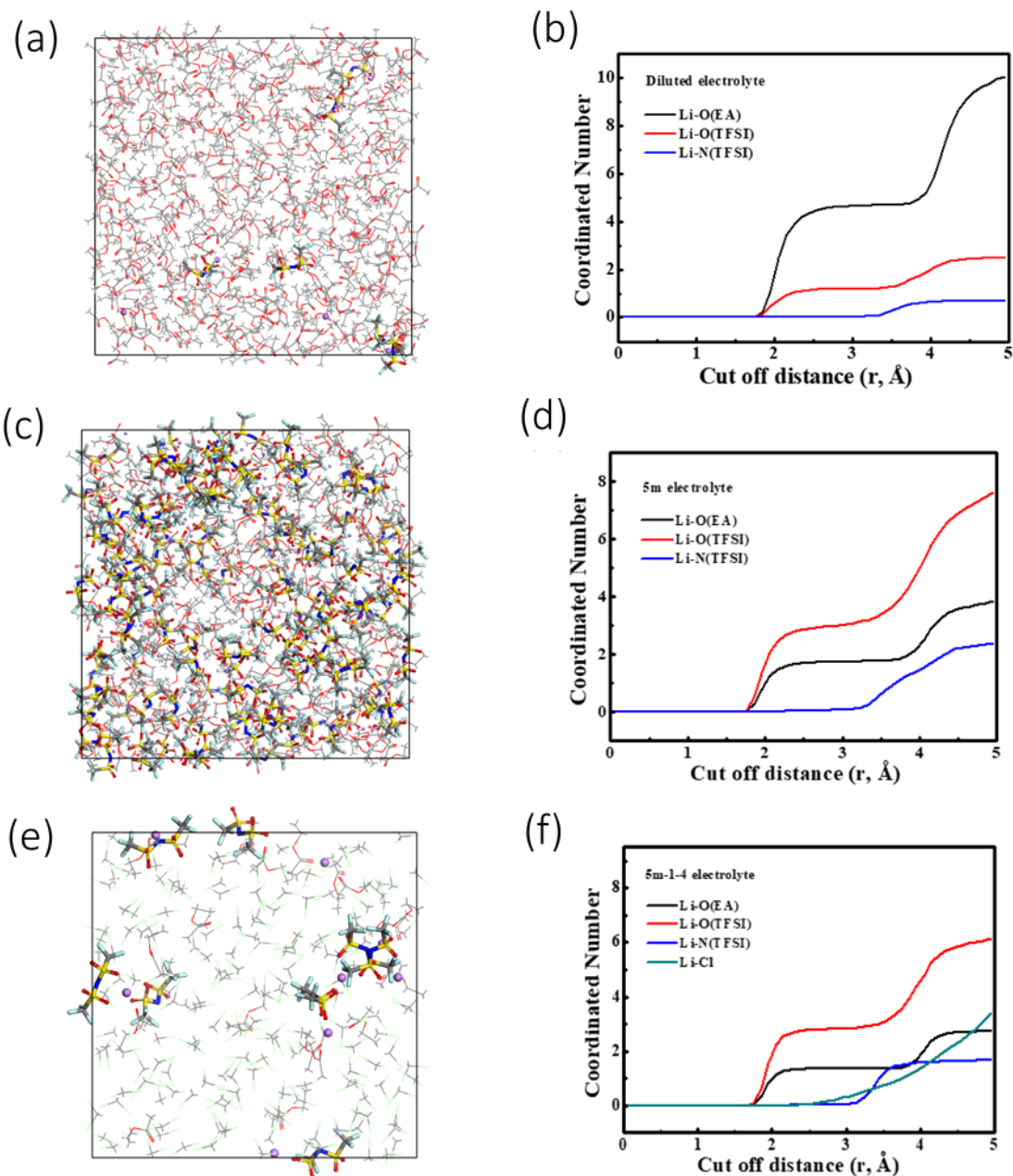


Figure 7.2 The snapshot (a) of MD simulation, and coordination number (CN) (b) as a function of cutoff distance for 0.15m EA-based electrolyte. The snapshot (c) of MD simulation, and CN (d) as a function of cutoff distance for 5m EA-based electrolyte. The snapshot (e) of MD simulation, and CN (f) as a function of cutoff distance for the 5m-1-4 co-solvent electrolyte.

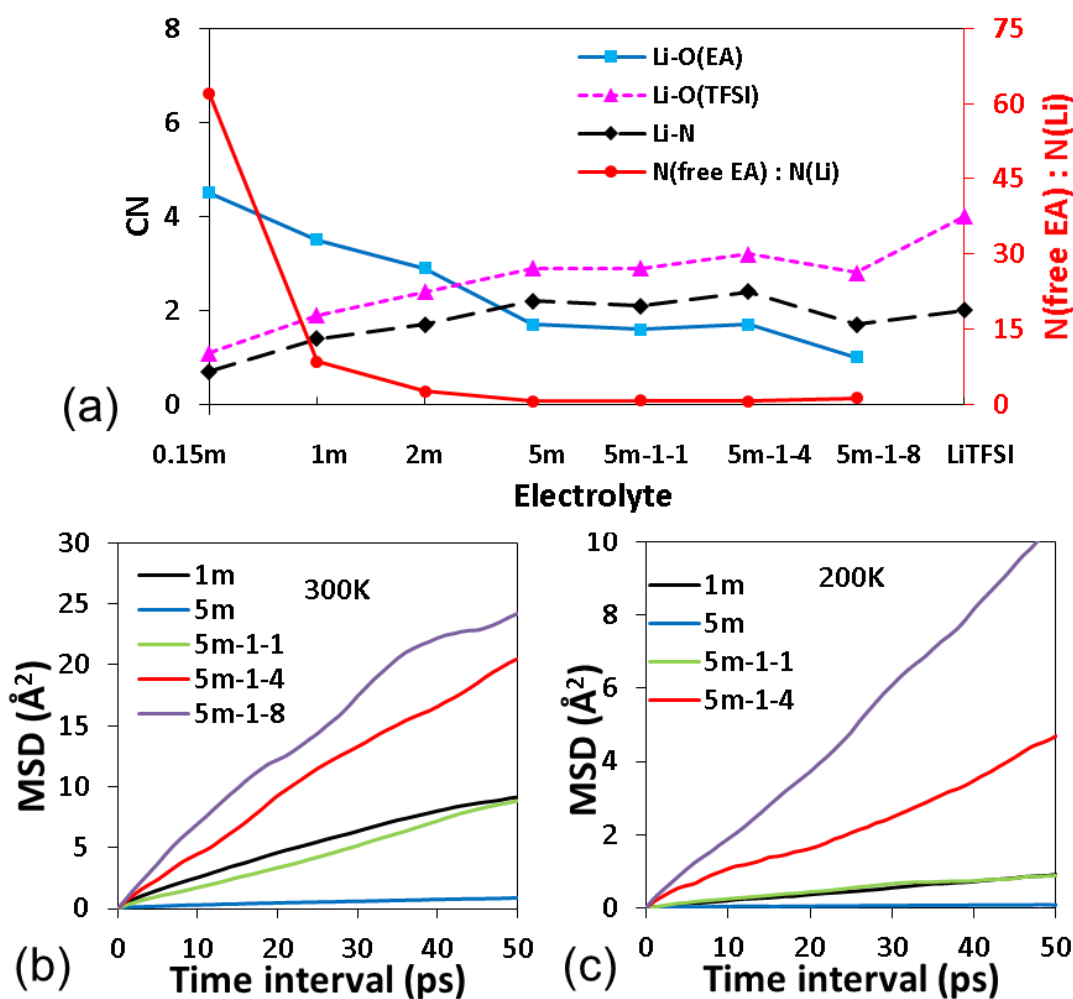


Figure 7.3 Coordinated numbers of EA molecules and TFSI⁻ anions around Li⁺, and mole fraction of free EA molecules in different electrolytes and LiTFSI crystal (a). The Li⁺ cation mean-squared displacements (MSD) in various electrolytes at +25 °C (b) and -70 °C (c).

7.5.4 HOMO and LUMO levels

The calculated HOMO and LUMO levels for each molecule species are listed in Table 7.4.

It can be seen that the LUMO levels ranked in the following order: TFSI⁻>LiTFSI>(Li₂TFSI)⁺.

While free TFSI⁻ anions and LiTFSI contact ion pairs (CIPs, the coordination of TFSI⁻ with one Li⁺) are stable at the Li anode, the reduction of (Li₂TFSI)⁺ in aggregate clusters (AGGs, the coordination of TFSI⁻ with two or more Li⁺) is much easier. The reduced product LiF can form

a relatively stable SEI layer containing LiF on the surface of Li anode and prevent further electrolyte reduction. As more AGGs exist in the concentrated electrolyte, its reduction potential will decrease upon the formation of the stable SEI layer. Furthermore, EA and TFSI⁻ both shared lower HOMO levels and are more difficult to be oxidized after binding with more Li-ions, contributing to a higher oxidation potential in the concentrated electrolyte. The increase of salt concentration will lead to the decreased amount of free EA molecules and increased amount of AGGs, similar to the “water-in-salt” electrolyte [104], thus enabled the wider electrochemical window in the concentrated electrolyte.

Table 7.4 Calculated LUMO and HOMO levels for different species in the electrolytes.

	LUMO (eV)	HOMO (eV)
DCM	-1.57	-7.42
EA	-0.98	-6.37
Li ⁺ ·(EA)	-5.95	-11.71
Li ⁺ ·(2EA)	-5.30	-10.87
TFSI ⁻	2.89	-3.20
LiTFSI	-2.17	-7.63
(Li ₂ TFSI) ⁺	-2.88	-8.40

7.6 Conclusion

In conclusion, a co-solvent electrolyte was designed by adding electrolyte low viscosity and electronically stable dichloromethane (DCM) to the highly-concentrated LiTFSI in ethyl acetate (EA) solvent. The Li binding energy of DCM was very low compared with that of EA and TFSI⁻. The unique co-solvation structure was determined as clusters of partially solvated Li⁺, TFSI⁻, and EA network surrounded by the DCM co-solvent. The partially solvated network

inherited the expanded electrochemical window of the highly-concentrated EA-based electrolyte and surrounding DCM co-solvent accelerated the Li transport at both room temperature and low temperature. Thus, this co-solvent electrolyte facilitate the low temperature batteries.

8 Conclusion and future research

In summary, this thesis focused on understanding of atomic scale electrode-electrolyte interfacial structure, interaction and property, and modeling their connection to the cell-level discharging performance of Li-S batteries. An integrated approach for battery materials design was provided from computation. Looking forward, future work on computational understanding of the electrode-electrolyte interfacial mechanisms is still needed.

On the anode-electrolyte interface, connection was made between the irreversible capacity loss and the electrical insulating property of SEI on anode assuming perfect crystals of inorganic SEI components and a static surface on Li metal anode. However, SEI growth mechanism may also involve other steps, such as porous SEI gradually densifies and dissolution and re-deposition of SEI [88]. Thus, investigation on the influence of the defects and polarons on electron transport mechanisms is needed. Furthermore, Li anode suffers from huge deformation, morphology change and dendrite growth during battery cycling. Therefore, it is needed to connect the mechanical property of SEI to the accommodation of Li deformation, the controlling of morphology change and the suppression of the dendrite growth. In addition, Li-PS shuttle can also be prevented if the deposition of the Li_2S_2 and Li_2S on Li anode surface was inhibited. This suggests the need to connect the adhesion property of SEI to the Li-PS shuttle problem.

On the cathode-electrolyte interface, two models were made to connect the solvation status of Li-PS to the ideal OCV curve and the practical discharging voltage curve, in terms of thermodynamics. Controlling the interfacial interaction between Li-PS and electrolyte by the

sizes of nanopore and sub-nanopore was further connected to the mitigation of “Li-PS shuttle problem”. However, understanding the kinetics of the discharging reaction at the cathode-electrolyte interface is of the same importance. For example, instead of being converted to Li_2S as predicted in thermodynamics, some S stays in the form of insulating and insoluble Li_2S_2 after fully discharging. Thus, another remained problem is to understand how the kinetics in the reaction from Li_2S_2 to Li_2S is connected to the discharging performance. Furthermore, the interaction between Li-PS and surface of carbon matrix should also be considered, especially for the nanopore and sub-nanopore. On one hand, absorbed Li-PS will not participate in the Li-PS shuttle. On the other hand, continuous lithiation of Li-PS is hindered by the absorption, decreasing the capacity. Thus, it is also needed to connect the absorption of the Li-PS on the carbon matrix to the mitigation of Li-PS shuttle and capacity.

BIBLIOGRAPHY

BIBLIOGRAPHY

- [1] M.S. Whittingham, Lithium batteries and cathode materials, *Chemical Reviews*. 104 (2004) 4271–4301. doi:10.1021/cr020731c.
- [2] D. Aurbach, B. Markovsky, G. Salitra, E. Markevich, Y. Talyossef, M. Koltypin, et al., Review on electrode-electrolyte solution interactions, related to cathode materials for Li-ion batteries, *Journal of Power Sources*. 165 (2007) 491–499. doi:10.1016/j.jpowsour.2006.10.025.
- [3] C. Zhang, W. Lv, Y. Tao, Q.-H. Yang, Towards superior volumetric performance: design and preparation of novel carbon materials for energy storage, *Energy Environ. Sci.* 00 (2015) 1–15. doi:10.1039/C5EE00389J.
- [4] K. Santosh, R.C. Longo, K. Xiong, K. Cho, Electrode-Electrolyte Interface for Solid State Li-Ion Batteries: Point Defects and Mechanical Strain, *Journal of the Electrochemical Society*. 161 (2014) F3104–F3110. doi:10.1149/2.0151411jes.
- [5] M.D. Halls, K. Tasaki, High-throughput quantum chemistry and virtual screening for lithium ion battery electrolyte additives, *Journal of Power Sources*. 195 (2010) 1472–1478. doi:10.1016/j.jpowsour.2009.09.024.
- [6] J.Y. Luo, W.J. Cui, P. He, Y.Y. Xia, Raising the cycling stability of aqueous lithium-ion batteries by eliminating oxygen in the electrolyte, *Nature Chemistry*. 2 (2010) 760–765. doi:10.1038/nchem.763.
- [7] C. Liu, Z.G. Neale, G. Cao, Understanding electrochemical potentials of cathode materials in rechargeable batteries, *Materials Today*. 19 (2016) 109–123. doi:10.1016/j.mattod.2015.10.009.
- [8] X. Li, J. Liu, X. Meng, Y. Tang, M.N. Banis, J. Yang, et al., Significant impact on cathode performance of lithium-ion batteries by precisely controlled metal oxide nanocoatings via atomic layer deposition, *Journal of Power Sources*. 247 (2014) 57–69. doi:10.1016/j.jpowsour.2013.08.042.
- [9] K. Xu, Electrolytes and interphases in Li-ion batteries and beyond, *Chemical Reviews*. 114 (2014) 11503–11618. doi:10.1021/cr500003w.
- [10] J.B. Goodenough, Y. Kim, Challenges for Rechargeable Li Batteries, *Chemistry of Materials*. 22 (2010) 587–603. doi:10.1021/cm901452z.

- [11] J.N. Zhang, Q. Li, Y. Wang, J. Zheng, X. Yu, H. Li, Dynamic evolution of cathode electrolyte interphase (CEI) on high voltage LiCoO₂ cathode and its interaction with Li anode, *Energy Storage Materials*. 14 (2018) 1–7. doi:10.1016/j.ensm.2018.02.016.
- [12] P. Verma, P. Maire, P. Novák, A review of the features and analyses of the solid electrolyte interphase in Li-ion batteries, *Electrochimica Acta*. 55 (2010) 6332–6341. doi:10.1016/j.electacta.2010.05.072.
- [13] M.B. Pinson, M.Z. Bazant, Theory of SEI Formation in Rechargeable Batteries: Capacity Fade, Accelerated Aging and Lifetime Prediction, *Journal of the Electrochemical Society*. 160 (2012) A243–A250. doi:10.1149/2.044302jes.
- [14] J. Christensen, J. Newman, A Mathematical Model for the Lithium-Ion Negative Electrode Solid Electrolyte Interphase, *Journal of The Electrochemical Society*. 151 (2004) A1977. doi:10.1149/1.1804812.
- [15] M. Hagen, D. Hanselmann, K. Ahlbrecht, R. Maça, D. Gerber, J. Tübke, Lithium-Sulfur Cells: The Gap between the State-of-the-Art and the Requirements for High Energy Battery Cells, *Advanced Energy Materials*. 5 (2015). doi:10.1002/aenm.201401986.
- [16] K. Lee, The Lithium Ion Battery Technology, *Carbon Science*. 2 (2001) 72–75.
- [17] M.-K. Song, E.J. Cairns, Y. Zhang, Lithium/sulfur batteries with high specific energy: old challenges and new opportunities, *Nanoscale*. 5 (2013) 2186. doi:10.1039/c2nr33044j.
- [18] J. Lochala, D. Liu, B. Wu, C. Robinson, J. Xiao, Research progress toward the practical applications of lithium–sulfur batteries, *ACS Applied Materials & Interfaces*. 9 (2017) 24407–24421. doi:10.1021/acsami.7b06208.
- [19] R. Miao, J. Yang, Z. Xu, J. Wang, Y. Nuli, L. Sun, A new ether-based electrolyte for dendrite-free lithium-metal based rechargeable batteries, *Scientific Reports*. 6 (2016) 2–10. doi:10.1038/srep21771.
- [20] F. Hao, A. Verma, P.P. Mukherjee, Mechanistic insight into dendrite-SEI interactions for lithium metal electrodes, *Journal of Materials Chemistry A*. 6 (2018) 19664–19671. doi:10.1039/c8ta07997h.
- [21] Y. V. Mikhaylik, J.R. Akridge, Polysulfide Shuttle Study in the Li–S Battery System, (2004) 1969–1976. doi:10.1149/1.1806394.

- [22] M.R. Busche, P. Adelhelm, H. Sommer, H. Schneider, K. Leitner, J. Janek, Systematical electrochemical study on the parasitic shuttle-effect in lithium-sulfur-cells at different temperatures and different rates, *Journal of Power Sources*. 259 (2014) 289–299. doi:10.1016/j.jpowsour.2014.02.075.
- [23] C. Wang, Y.S. Meng, K. Xu, Perspective—Fluorinating Interphases, *Journal of The Electrochemical Society*. 166 (2018) A5184–A5186. doi:10.1149/2.0281903jes.
- [24] X. Fan, L. Chen, X. Ji, T. Deng, S. Hou, J. Chen, et al., Highly Fluorinated Interphases Enable High-Voltage Li-Metal Batteries, *Chem*. 4 (2018) 174–185. doi:10.1016/j.chempr.2017.10.017.
- [25] A. Wang, S. Kadam, H. Li, S. Shi, Y. Qi, Review on modeling of the anode solid electrolyte interphase (SEI) for lithium-ion batteries, *Npj Computational Materials*. 4 (2018). doi:10.1038/s41524-018-0064-0.
- [26] L.E. Camacho-Forero, T.W. Smith, P.B. Balbuena, Effects of high and low salt concentration in electrolytes at lithium-metal anode surfaces, *Journal of Physical Chemistry C*. 121 (2017) 182–194. doi:10.1021/acs.jpcc.6b10774.
- [27] X. Fan, L. Chen, O. Borodin, X. Ji, J. Chen, S. Hou, et al., Non-flammable electrolyte enables Li-metal batteries with aggressive cathode chemistries, *Nature Nanotechnology*. 13 (2018) 1–8. doi:10.1038/s41565-018-0183-2.
- [28] L. Suo, O. Borodin, T. Gao, M. Olguin, J. Ho, X. Fan, et al., “Water-in-salt” electrolyte enables high-voltage aqueous lithium-ion chemistries, *Science*. 350 (2015) 938–943. doi:10.1126/science.aab1595.
- [29] N.S. Choi, K.H. Yew, K.Y. Lee, M. Sung, H. Kim, S.S. Kim, Effect of fluoroethylene carbonate additive on interfacial properties of silicon thin-film electrode, *Journal of Power Sources*. 161 (2006) 1254–1259. doi:10.1016/j.jpowsour.2006.05.049.
- [30] M.I. Nandasiri, L.E. Camacho-Forero, A.M. Schwarz, V. Shutthanandan, S. Thevuthasan, P.B. Balbuena, et al., In situ chemical imaging of solid-electrolyte interphase layer evolution in Li-S batteries, *Chemistry of Materials*. 29 (2017) 4728–4737. doi:10.1021/acs.chemmater.7b00374.
- [31] Q. Zhang, J. Pan, P. Lu, Z. Liu, M.W. Verbrugge, B.W. Sheldon, et al., Synergetic Effects of Inorganic Components in Solid Electrolyte Interphase on High Cycle Efficiency of Lithium Ion Batteries, *Nano Letters*. 16 (2016) 2011–2016. doi:10.1021/acs.nanolett.5b05283.

- [32] N.W. Li, Y. Shi, Y.X. Yin, X.X. Zeng, J.Y. Li, C.J. Li, et al., A Flexible Solid Electrolyte Interphase Layer for Long-Life Lithium Metal Anodes, *Angewandte Chemie - International Edition*. 57 (2018) 1505–1509. doi:10.1002/anie.201710806.
- [33] N.S. Choi, Y.M. Lee, W. Seol, J.A. Lee, J.K. Park, Protective coating of lithium metal electrode for interfacial enhancement with gel polymer electrolyte, *Solid State Ionics*. 172 (2004) 19–24. doi:10.1016/j.ssi.2004.05.008.
- [34] J. Lopez, A. Pei, J.Y. Oh, G.J.N. Wang, Y. Cui, Z. Bao, Effects of Polymer Coatings on Electrodeposited Lithium Metal, *Journal of the American Chemical Society*. 140 (2018) 11735–11744. doi:10.1021/jacs.8b06047.
- [35] J. Zheng, X. Fan, G. Ji, H. Wang, S. Hou, K.C. DeMella, et al., Manipulating electrolyte and solid electrolyte interphase to enable safe and efficient Li-S batteries, *Nano Energy*. 50 (2018) 431–440. doi:10.1016/j.nanoen.2018.05.065.
- [36] S. Xin, L. Gu, N. Zhao, Y. Yin, L. Zhou, Y. Guo, et al., Smaller sulfur molecules promise better lithium-sulfur batteries, *Journal of the American Chemical Society*. 134 (2012) 18510.
- [37] Y. Wang, S. Nakamura, M. Ue, P.B. Balbuena, Theoretical studies to understand surface chemistry on carbon anodes for lithium-ion batteries: Reduction mechanisms of ethylene carbonate, *Journal of the American Chemical Society*. 123 (2001) 11708–11718. doi:10.1021/ja0164529.
- [38] K. Leung, J.L. Budzien, Ab initio molecular dynamics simulations of the initial stages of solid-electrolyte interphase formation on lithium ion battery graphitic anodes, *Physical Chemistry Chemical Physics*. 12 (2010) 6583–6586. doi:10.1039/b925853a.
- [39] E. Peled, An Advanced Tool for the Selection of Electrolyte Components for Rechargeable Lithium Batteries, *Journal of The Electrochemical Society*. 145 (1998) 3482. doi:10.1149/1.1838831.
- [40] a. M. Andersson, K. Edström, Chemical Composition and Morphology of the Elevated Temperature SEI on Graphite, *Journal of The Electrochemical Society*. 148 (2001) A1100. doi:10.1149/1.1397771.
- [41] D. Aurbach, E. Pollak, R. Elazari, G. Salitra, C.S. Kelley, J. Affinito, On the Surface Chemical Aspects of Very High Energy Density, Rechargeable Li–Sulfur Batteries, *Journal of The Electrochemical Society*. 156 (2009) A694. doi:10.1149/1.3148721.
- [42] S. Xiong, K. Xie, Y. Diao, X. Hong, Characterization of the solid electrolyte interphase

- on lithium anode for preventing the shuttle mechanism in lithium-sulfur batteries, *Journal of Power Sources*. 246 (2014) 840–845. doi:10.1016/j.jpowsour.2013.08.041.
- [43] H. Shin, J. Park, S. Han, A.M. Sastry, W. Lu, Component-/structure-dependent elasticity of solid electrolyte interphase layer in Li-ion batteries: Experimental and computational studies, *Journal of Power Sources*. 277 (2015) 169–179. doi:10.1016/j.jpowsour.2014.11.120.
- [44] Z. Liu, Y. Qi, Y.X. Lin, L. Chen, P. Lu, L.Q. Chen, Interfacial Study on Solid Electrolyte Interphase at Li Metal Anode: Implication for Li Dendrite Growth, *Journal of The Electrochemical Society*. 163 (2016) A592–A598. doi:10.1149/2.0151605jes.
- [45] S. Shi, P. Lu, Z. Liu, Y. Qi, L.G. Hector, H. Li, et al., Direct calculation of Li-ion transport in the solid electrolyte interphase, *Journal of the American Chemical Society*. 134 (2012) 15476–15487. doi:10.1021/ja305366r.
- [46] J. Pan, Y. Cheng, Y. Qi, General method to predict voltage-dependent ionic conduction in a solid electrolyte, *134116 (2015) 1–9*. doi:10.1103/PhysRevB.91.134116.
- [47] J. Pan, Q. Zhang, X. Xiao, Y.-T. Cheng, Y. Qi, Design of Nanostructured Heterogeneous Solid Ionic Coatings through a Multiscale Defect Model, (2016). doi:10.1021/acsami.5b12030.
- [48] Q. Zhang, J. Pan, P. Lu, Z. Liu, M.W. Verbrugge, B.W. Sheldon, et al., Synergetic Effects of Inorganic Components in Solid Electrolyte Interphase on High Cycle Efficiency of Lithium Ion Batteries, *Nano Letters*. (2016) acs.nanolett.5b05283. doi:10.1021/acs.nanolett.5b05283.
- [49] and Y.Q.Y.-X.L.Z.L.K.L.L.-Q.C. Peng Lu, Connecting the irreversible capacity loss in Li-ion batteries with the electronic insulating properties of solid electrolyte interphase (SEI) components, *Journal of Power Sources*. 309 (2016) 221–230. doi:10.1016/j.str.2014.12.012.
- [50] E. Peled, The Electrochemical Behavior of Alkali and Alkaline Earth Metals in Nonaqueous Battery Systems—The Solid Electrolyte Interphase Model, *Journal of The Electrochemical Society*. 126 (1979) 2047. doi:10.1149/1.2128859.
- [51] D. Li, D. Danilov, Z. Zhang, H. Chen, Y. Yang, P.H.L. Notten, Modeling the SEI-Formation on Graphite Electrodes in LiFePO₄ Batteries, *Journal of the Electrochemical Society*. 162 (2015) A858–A869. doi:10.1149/2.0161506jes.
- [52] K. Leung, Electronic Structure Modeling of Electrochemical Reactions at Electrode /

- Electrolyte Interfaces in Lithium Ion Batteries, *The Journal of Physical Chemistry C*. 117 (2013) 1539–1547.
- [53] K. Leung, Y. Qi, K.R. Zavadil, Y.S. Jung, A.C. Dillon, A.S. Cavanagh, et al., Using atomic layer deposition to hinder solvent decomposition in lithium ion batteries: first principles modeling and experimental studies., *Journal of the American Chemical Society*. (2011) 14741–14754. doi:10.1021/ja205119g.
- [54] F. Joho, B. Rykart, A. Blome, P. Novák, H. Wilhelm, M.E. Spahr, Relation between surface properties, pore structure and first-cycle charge loss of graphite as negative electrode in lithium-ion batteries, *Journal of Power Sources*. 97–98 (2001) 78–82. doi:10.1016/S0378-7753(01)00595-X.
- [55] H. Wu, G. Chan, J.W. Choi, I. Ryu, Y. Yao, M.T. McDowell, et al., Stable cycling of double-walled silicon nanotube battery anodes through solid–electrolyte interphase control, *Nature Nanotechnology*. 7 (2012) 310–315. doi:10.1038/nnano.2012.35.
- [56] C.-F. Sun, K. Karki, Z. Jia, H. Liao, Y. Zhang, T. Li, et al., A beaded-string silicon anode., *ACS Nano*. 7 (2013) 2717–24. doi:10.1021/nm4001512.
- [57] X.-B. Cheng, J.-Q. Huang, Q. Zhang, Review—Li Metal Anode in Working Lithium-Sulfur Batteries, *Journal of The Electrochemical Society*. 165 (2017) A6058–A6072. doi:10.1149/2.0111801jes.
- [58] B.A. Boukamp, G.C. Lesh, R.A. Huggins, All-Solid Lithium Electrodes with Mixed-Conductor Matrix, *Journal of The Electrochemical Society*. 128 (1981) 725. doi:10.1149/1.2127495.
- [59] P.A. Chen, C.Y. Chang, C. Juang, Compressive and tensile strain effects on hole tunneling in an InGaAs/AlInAs asymmetrical coupled quantum well, *Journal of Applied Physics*. 74 (1993) 7294–7301. doi:10.1063/1.355333.
- [60] E. Zallo, R. Trotta, V. Křápek, Y.H. Huo, P. Atkinson, F. Ding, et al., Strain-induced active tuning of the coherent tunneling in quantum dot molecules, *Physical Review B - Condensed Matter and Materials Physics*. 89 (2014) 1–5. doi:10.1103/PhysRevB.89.241303.
- [61] D. Aurbach, M.D. Levi, E. Levi, A. Schechter, Failure and Stabilization Mechanisms of Graphite Electrodes, *The Journal of Physical Chemistry B*. 101 (1997) 2195–2206. doi:10.1021/jp962815t.
- [62] M. Wissler, Graphite and carbon powders for electrochemical applications, *Journal of*

- Power Sources. 156 (2006) 142–150. doi:10.1016/j.jpowsour.2006.02.064.
- [63] D.-W. Wang, Q. Zeng, G. Zhou, L. Yin, F. Li, H.-M. Cheng, et al., Carbon-sulfur composites for Li-S batteries: status and prospects, *Journal of Materials Chemistry A*. 1 (2013) 9382–9394. doi:10.1039/C3TA11045A.
- [64] S.S. Zhang, Liquid electrolyte lithium/sulfur battery: Fundamental chemistry, problems, and solutions, *Journal of Power Sources*. 231 (2013) 153–162. doi:10.1016/j.jpowsour.2012.12.102.
- [65] C. Zhang, Y. Lin, J. Liu, Sulfur double locked by a macro-structural cathode and a solid polymer electrolyte for lithium–sulfur batteries, *J. Mater. Chem. A*. 3 (2015) 10760–10766. doi:10.1039/C5TA01037C.
- [66] Z. Lin, Z. Liu, W. Fu, N.J. Dudney, C. Liang, Lithium polysulfidophosphates: A family of lithium-conducting sulfur-rich compounds for lithium-sulfur batteries, *Angewandte Chemie - International Edition*. 52 (2013) 7460–7463. doi:10.1002/anie.201300680.
- [67] S. Xin, L. Gu, N.H. Zhao, Y.X. Yin, L.J. Zhou, Y.G. Guo, et al., Smaller sulfur molecules promise better lithium-sulfur batteries, *Journal of the American Chemical Society*. 134 (2012) 18510–18513. doi:10.1021/ja308170k.
- [68] M. Helen, M.A. Reddy, T. Diemant, U. Golla-Schindler, R.J. Behm, U. Kaiser, et al., Single step transformation of sulphur to Li₂S₂/Li₂S in Li-S batteries, *Scientific Reports*. 5 (2015) 12146. doi:10.1038/srep12146.
- [69] Y. Zhou, C. Zhou, Q. Li, C. Yan, B. Han, K. Xia, et al., Enabling prominent high-rate and cycle performances in one lithium-sulfur battery: designing permselective gateways for Li⁺ transportation in holey-CNT/S cathodes, *Advanced Materials*. 27 (2015) 3774–3781. doi:10.1002/adma.201501082.
- [70] T. Fujimori, A. Morelos-Gómez, Z. Zhu, H. Muramatsu, R. Futamura, K. Urita, et al., Conducting linear chains of sulphur inside carbon nanotubes, *Nature Communications*. 4 (2013) 1–8. doi:10.1038/ncomms3162.
- [71] X. Ji, K.T. Lee, L.F. Nazar, A highly ordered nanostructured carbon–sulphur cathode for lithium–sulphur batteries, *Nature Materials*. 8 (2009) 500–506. doi:10.1038/nmat2460.
- [72] E. Markevich, G. Salitra, A. Rosenman, Y. Talyosef, F. Chesneau, D. Aurbach, Fluoroethylene carbonate as an important component in organic carbonate electrolyte solutions for lithium sulfur batteries, *Electrochemistry Communications*. 60 (2015) 42–46. doi:10.1016/j.elecom.2015.08.004.

- [73] B. Zhang, C. Lai, Z. Zhou, X.P. Gao, Preparation and electrochemical properties of sulfur-acetylene black composites as cathode materials, *Electrochimica Acta*. 54 (2009) 3708–3713. doi:10.1016/j.electacta.2009.01.056.
- [74] J.-W. Park, K. Yamauchi, E. Takashima, N. Tachikawa, K. Ueno, K. Dokko, et al., Solvent effect of room temperature ionic liquids on electrochemical reactions in lithium–sulfur batteries, *The Journal of Physical Chemistry C*. 117 (2013) 4431–4440. doi:10.1021/jp400153m.
- [75] Y.Z. Zhang, S. Liu, G.C. Li, G.R. Li, X.P. Gao, Sulfur/polyacrylonitrile/carbon multi-composites as cathode materials for lithium/sulfur battery in the concentrated electrolyte, *J. Mater. Chem. A*. 2 (2014) 4652–4659. doi:10.1039/C3TA14914E.
- [76] L. Suo, Y.-S. Hu, H. Li, M. Armand, L. Chen, A new class of Solvent-in-Salt electrolyte for high-energy rechargeable metallic lithium batteries, *Nature Communications*. 4 (2013) 1481. doi:10.1038/ncomms2513.
- [77] D. Lv, P. Yan, Y. Shao, Q. Li, S. Ferrara, H. Pan, et al., High performance Li-ion sulfur batteries enabled by intercalation chemistry, *Chem. Commun*. 51 (2015) 13454–13457. doi:10.1039/C5CC05171A.
- [78] J. Zheng, X. Fan, G. Ji, H. Wang, S. Hou, K.C. DeMella, et al., Manipulating electrolyte and solid electrolyte interphase to enable safe and efficient Li-S batteries, *Nano Energy*. 50 (2018) 431–440. doi:10.1016/j.nanoen.2018.05.065.
- [79] E. Markevich, G. Salitra, Y. Talyosef, F. Chesneau, D. Aurbach, Review—On the mechanism of quasi-solid-state lithiation of sulfur encapsulated in microporous carbons: Is the existence of small sulfur molecules necessary?, *Journal of The Electrochemical Society*. 164 (2017) A6244–A6253. doi:10.1149/2.0391701jes.
- [80] Y.S. Meng, M.E. Arroyo-de Dompablo, First principles computational materials design for energy storage materials in lithium ion batteries, *Energy & Environmental Science*. 2 (2009) 589. doi:10.1039/b901825e.
- [81] S.P. Ong, V.L. Chevrier, G. Hautier, A. Jain, C. Moore, S. Kim, et al., Voltage, stability and diffusion barrier differences between sodium-ion and lithium-ion intercalation materials, *Energy & Environmental Science*. 4 (2011) 3680. doi:10.1039/c1ee01782a.
- [82] Y. Yamaguchi, T. Takeuchi, H. Sakaebe, H. Kageyama, H. Senoh, T. Sakai, et al., Ab initio simulations of Li/pyrite-MS₂ (M=Fe, Ni) battery cells, *Journal of The Electrochemical Society*. 157 (2010) A630. doi:10.1149/1.3365019.

- [83] I.A. Courtney, J.S. Tse, O. Mao, J. Hafner, J.R. Dahn, Ab initio calculation of the lithium-tin voltage profile, *Physical Review B - Condensed Matter and Materials Physics*. 58 (1998) 15583–15588. doi:10.1103/PhysRevB.58.15583.
- [84] G. Yang, S. Shi, J. Yang, Y. Ma, Insight into the role of Li₂S₂ in Li–S batteries: a first-principles study, *J. Mater. Chem. A*. 3 (2015) 8865–8869. doi:10.1039/C5TA00499C.
- [85] L. Wang, T. Zhang, S. Yang, F. Cheng, J. Liang, J. Chen, A quantum-chemical study on the discharge reaction mechanism of lithium-sulfur batteries, *Journal of Energy Chemistry*. 22 (2013) 72–77. doi:10.1016/S2095-4956(13)60009-1.
- [86] H. Okamoto, The Li-S (lithium-sulfur) system, *Journal of Phase Equilibria*. 16 (1995) 94–97. doi:10.1007/BF02646258.
- [87] R. Kumar, J. Liu, J.Y. Hwang, Y.K. Sun, Recent research trends in Li-S batteries, *Journal of Materials Chemistry A*. 6 (2018) 11582–11605. doi:10.1039/c8ta01483c.
- [88] C. Shen, J. Xie, M. Zhang, P. Andrei, M. Hendrickson, E.J. Plichta, et al., Self-Discharge Behavior of Lithium-Sulfur Batteries at Different Electrolyte/Sulfur Ratios, *Journal of The Electrochemical Society*. 166 (2019) A5287–A5294. doi:10.1149/2.0461903jes.
- [89] J. Zheng, D. Lv, M. Gu, C. Wang, J.-G. Zhang, J. Liu, et al., How to Obtain Reproducible Results for Lithium Sulfur Batteries?, *Journal of The Electrochemical Society*. 160 (2013) A2288–A2292. doi:10.1149/2.106311jes.
- [90] J. Zheng, M. Gu, M.J. Wagner, K.A. Hays, X. Li, P. Zuo, et al., Revisit Carbon / Sulfur Composite for Li-S Batteries, 160 (2013) 1624–1628. doi:10.1149/2.013310jes.
- [91] Z. Li, L. Yuan, Z. Yi, Y. Sun, Y. Liu, Y. Jiang, et al., Insight into the electrode mechanism in lithium-sulfur batteries with ordered microporous carbon confined sulfur as the cathode, *Advanced Energy Materials*. 4 (2014) 1–8. doi:10.1002/aenm.201301473.
- [92] S. Berber, Y. Kwon, D. Tománek, Unusually High Thermal Conductivity of Carbon Nanotubes, *Physical Review Letters*. 84 (2000) 4613–4616.
- [93] S.A. Getty, E. Cobas, M.S. Fuhrer, Extraordinary Mobility in Semiconducting Carbon Nanotubes, *Nano Letters*. (2004) 2–6. doi:10.1021/nl034841q.
- [94] D.H. Robertson, D.W. Brenner, Energetics of nanoscale graphitic tubules, *Physical Review Applied*. 45 (1992) 592–595.

- [95] R.H. Baughman, A.A. Zakhidov, W.A. De Heer, Carbon Nanotubes — the Route Toward Applications, *Science*. 297 (2002) 787–793.
- [96] D. V Kosynkin, A.L. Higginbotham, A. Sinitskii, J.R. Lomeda, A. Dimiev, B.K. Price, et al., Longitudinal unzipping of carbon nanotubes to form graphene nanoribbons, *Nature*. 458 (2009) 872–876. doi:10.1038/nature07872.
- [97] G. Gao, M. Pan, C.D. Vecitis, Effect of the oxidation approach on carbon nanotube surface functional groups and electrooxidative filtration performance, *Journal of Materials Chemistry A*. 3 (2015) 7575–7582. doi:10.1039/c4ta07191c.
- [98] S. Osswald, E. Flahaut, H. Ye, Y. Gogotsi, Elimination of D-band in Raman spectra of double-wall carbon nanotubes by oxidation, *Chemical Physics Letters*. 402 (2005) 422–427. doi:10.1016/j.cplett.2004.12.066.
- [99] J. Zhang, H. Zou, Q. Qing, Y. Yang, Q. Li, Z. Liu, et al., Effect of Chemical Oxidation on the Structure of Single-Walled Carbon Nanotubes, *The Journal of Physical Chemistry B*. 107 (2003) 3712–3718. doi:10.1021/jp027500u.
- [100] H. Zhang, X. He, M. Zhao, M. Zhang, L. Zhao, X. Feng, et al., Tunable hydrogen separation in sp-sp² hybridized carbon membranes: A first-principles prediction, *Journal of Physical Chemistry C*. 116 (2012) 16634–16638. doi:10.1021/jp304908p.
- [101] S. Jiao, Z. Xu, Selective gas diffusion in graphene oxides membranes: A molecular dynamics simulations study, *ACS Applied Materials and Interfaces*. 7 (2015) 9052–9059. doi:10.1021/am509048k.
- [102] Y. Song, B. Jiang, F.L. Li, Molecular dynamic simulations of selective self-diffusion of CH₄/CO₂/H₂O/N₂ in coal, *IOP Conference Series: Materials Science and Engineering*. 213 (2017) 012014. doi:10.1088/1757-899X/213/1/012014.
- [103] H. Kim, J. Hong, K.-Y. Park, H. Kim, S.-W. Kim, K. Kang, Aqueous Rechargeable Li and Na Ion Batteries, *Chemical Reviews*. 114 (2014) 11788–11827. doi:10.1021/cr500232y.
- [104] L. Suo, O. Borodin, T. Gao, M. Olguin, J. Ho, X. Fan, et al., “Water-in-salt” electrolyte enables high-voltage aqueous lithium-ion chemistries, 350 (2015).
- [105] L. Suo, F. Han, X. Fan, H. Liu, K. Xu, C. Wang, “water-in-Salt” electrolytes enable green and safe Li-ion batteries for large scale electric energy storage applications, *Journal of Materials Chemistry A*. 4 (2016) 6639–6644. doi:10.1039/c6ta00451b.

- [106] W. Sun, L. Suo, F. Wang, N. Eidson, C. Yang, F. Han, et al., “Water-in-Salt” electrolyte enabled LiMn₂O₄/TiS₂ Lithium-ion batteries, *Electrochemistry Communications*. 82 (2017) 71–74. doi:10.1016/j.elecom.2017.07.016.
- [107] C. Yang, L. Suo, O. Borodin, F. Wang, W. Sun, T. Gao, et al., Unique aqueous Li-ion/sulfur chemistry with high energy density and reversibility, *Proceedings of the National Academy of Sciences*. 114 (2017) 6197–6202. doi:10.1073/pnas.1703937114.
- [108] Q. Dong, X. Yao, Y. Zhao, M. Qi, X. Zhang, H. Sun, et al., Cathodically Stable Li-O₂ Battery Operations Using Water-in-Salt Electrolyte, *Chem*. 4 (2018) 1345–1358. doi:10.1016/j.chempr.2018.02.015.
- [109] X. Dong, Z. Guo, Z. Guo, Y. Wang, Y. Xia, Organic Batteries Operated at –70°C, *Joule*. 2 (2018) 902–913. doi:10.1016/J.JOULE.2018.01.017.
- [110] X. Dong, Y. Lin, P. Li, Y. Ma, J. Huang, D. Bin, et al., Lithium Metal Batteries High-Energy Rechargeable Metallic Lithium Battery at À 70 8 C Enabled by a Cosolvent Electrolyte *Angewandte*, (2019) 1–6. doi:10.1002/anie.201900266.
- [111] X. Ren, S. Chen, H. Lee, J. Liu, X. Ren, S. Chen, et al., Localized High-Concentration Sulfone Electrolytes for High-Efficiency Lithium-Metal Batteries Localized High-Concentration Sulfone Electrolytes for High-Efficiency Lithium-Metal Batteries, (n.d.) 1–16. doi:10.1016/j.chempr.2018.05.002.
- [112] J. Zheng, S. Chen, W. Zhao, J. Song, M.H. Engelhard, J. Zhang, Extremely Stable Sodium Metal Batteries Enabled by Localized High-Concentration Electrolytes, (2018). doi:10.1021/acsenergylett.7b01213.
- [113] M. Endo, C. Kim, K. Nishimura, T. Fujino, K. Miyashita, Recent development of carbon materials for Li ion batteries, *Carbon*. 38 (2000) 183–197. doi:10.1016/S0008-6223(99)00141-4.
- [114] M. Winter, J.O. Besenhard, M.E. Spahr, P. Novák, Insertion Electrode Materials for Rechargeable Lithium Batteries, *Advanced Materials*. 10 (1998) 725–763. doi:10.1002/(SICI)1521-4095(199807)10:10<725::AID-ADMA725>3.0.CO;2-Z.
- [115] H. Buqa, A. Würsig, J. Vetter, M.E. Spahr, F. Krumeich, P. Novák, SEI film formation on highly crystalline graphitic materials in lithium-ion batteries, *Journal of Power Sources*. 153 (2006) 385–390. doi:10.1016/j.jpowsour.2005.05.036.
- [116] S.H. Ng, C. Vix-Guterl, P. Bernardo, N. Tran, J. Ufheil, H. Buqa, et al., Correlations between surface properties of graphite and the first cycle specific charge loss in lithium-

- ion batteries, *Carbon*. 47 (2009) 705–712. doi:10.1016/j.carbon.2008.11.008.
- [117] M. Green, E. Fielder, B. Scrosati, M. Wachtler, J.S. Moreno, Structured Silicon Anodes for Lithium Battery Applications, *Electrochemical and Solid-State Letters*. 6 (2003) A75. doi:10.1149/1.1563094.
- [118] M. Yoshio, S. Kugino, N. Dimov, Electrochemical behaviors of silicon based anode material, *Journal of Power Sources*. 153 (2006) 375–379. doi:10.1016/j.jpowsour.2005.05.052.
- [119] K. Eom, J. Jung, J.T. Lee, V. Lair, T. Joshi, S.W. Lee, et al., Improved stability of nano-Sn electrode with high-quality nano-SEI formation for lithium ion battery, *Nano Energy*. 12 (2015) 314–321. doi:10.1016/j.nanoen.2014.12.041.
- [120] J. Li, X. Xiao, Y. Cheng, M.W. Verbrugge, Atomic Layered Coating Enabling Ultrafast Surface Kinetics at Silicon, *The Journal of Chemistry Letters*. 4 (2013) 3387–3391.
- [121] Y. Liu, Z.Y. Wen, X.Y. Wang, X.L. Yang, a. Hirano, N. Imanishi, et al., Improvement of cycling stability of Si anode by mechanochemical reduction and carbon coating, *Journal of Power Sources*. 189 (2009) 480–484. doi:10.1016/j.jpowsour.2008.12.045.
- [122] E.M. Lotfabad, P. Kalisvaart, A. Kohandehghan, K. Cui, M. Kupsta, B. Farbod, et al., Si nanotubes ALD coated with TiO₂, TiN or Al₂O₃ as high performance lithium ion battery anodes, *Journal of Materials Chemistry A*. 2 (2014) 2504. doi:10.1039/c3ta14302c.
- [123] P. Lu, S.J. Harris, Lithium transport within the solid electrolyte interphase, *Electrochemistry Communications*. 13 (2011) 1035–1037. doi:10.1016/j.elecom.2011.06.026.
- [124] J. Zheng, H. Zheng, R. Wang, L. Ben, W. Lu, L. Chen, et al., 3D visualization of inhomogeneous multi-layered structure and Young's modulus of the solid electrolyte interphase (SEI) on silicon anodes for lithium ion batteries, *Physical Chemistry Chemical Physics*. 16 (2014) 13229. doi:10.1039/c4cp01968g.
- [125] N. Weadock, N. Varongchayakul, J. Wan, S. Lee, J. Seog, L. Hu, Determination of mechanical properties of the SEI in sodium ion batteries via colloidal probe microscopy, *Nano Energy*. 2 (2013) 713–719. doi:10.1016/j.nanoen.2013.08.005.
- [126] P.K. Jha, B. N. Jha, Mechanical Properties of LiF and LiCl Crystals under High Pressure, *Phys. Stat. Sol. (B)*. 175 (1993) K1.
- [127] S. V. Lubenets, E.I. Ostapchuk, L.M. Soifer, F. Appel, H.-J. Kaufmann, The influence of

- OH⁻-ions on the mechanical properties in LiF and NaCl single crystals, *Crystal Research and Technology*. 19 (1984) 349–356. doi:10.1002/crat.2170190311.
- [128] S.-Y. Kim, Y. Qi, Property Evolution of Al₂O₃ Coated and Uncoated Si Electrodes: A First Principles Investigation, *Journal of the Electrochemical Society*. 161 (2014) F3137–F3143. doi:10.1149/2.0301414jes.
- [129] E. Söderlund, I. Reineck, D.J. Rowcliffe, Ultralow load indentation hardness and modulus of K – and α–Al₂O₃ CVD coatings, *Journal of Materials Research*. 9 (1994) 1683–1692. doi:10.1557/JMR.1994.1683.
- [130] Y.A. Du, N.A.W. Holzwarth, Mechanisms of Li⁺ diffusion in crystalline γ- and β-Li₃PO₄ electrolytes from first principles, *Physical Review B - Condensed Matter and Materials Physics*. 76 (2007) 174302. doi:10.1103/PhysRevB.76.174302.
- [131] S. Shi, Y. Qi, H. Li, L.G. Hector, Defect Thermodynamics and Diffusion Mechanisms in Li₂CO₃ and Implications for the Solid Electrolyte Interphase in Li-Ion Batteries, *Journal of Physical Chemistry*. 117 (2013) 8579–8593.
- [132] F.C. Simeone, D.M. Kolb, S. Venkatachalam, T. Jacob, The Au(111)/electrolyte interface: A tunnel-spectroscopic and DFT investigation, *Angewandte Chemie - International Edition*. 46 (2007) 8903–8906. doi:10.1002/anie.200702868.
- [133] F.C. Simeone, D.M. Kolb, S. Venkatachalam, T. Jacob, Tunneling behavior of electrified interfaces, *Surface Science*. 602 (2008) 1401–1407. doi:10.1016/j.susc.2008.01.034.
- [134] M. Kondratenko, S.R. Stoyanov, S. Gusarov, A. Kovalenko, R.L. McCreery, Theoretical Modeling of Tunneling Barriers in Carbon-Based Molecular Electronic Junctions, *The Journal of Physical Chemistry C*. 119 (2015) 11286–11295. doi:10.1021/jp5128332.
- [135] N. Park, S. Hong, Electronic structure calculations of metal-nanotube contacts with or without oxygen adsorption, *Physical Review B - Condensed Matter and Materials Physics*. 72 (2005) 1–5. doi:10.1103/PhysRevB.72.045408.
- [136] M. Bokdam, G. Brocks, M.I. Katsnelson, P.J. Kelly, Schottky barriers at hexagonal boron nitride/metal interfaces: A first-principles study, *Physical Review B*. 90 (2014) 085415. doi:10.1103/PhysRevB.90.085415.
- [137] R. Deshpande, M. Verbrugge, Y.-T. Cheng, J. Wang, P. Liu, Battery Cycle Life Prediction with Coupled Chemical Degradation and Fatigue Mechanics, *Journal of the Electrochemical Society*. 159 (2012) A1730–A1738. doi:10.1149/2.049210jes.

- [138] M.W. Verbrugge, Y.-T. Cheng, Stress and Strain-Energy Distributions within Diffusion-Controlled Insertion-Electrode Particles Subjected to Periodic Potential Excitations, *Journal of The Electrochemical Society*. 156 (2009) A927. doi:10.1149/1.3205485.
- [139] A. Tokranov, B.W. Sheldon, P. Lu, X. Xiao, A. Mukhopadhyay, The Origin of Stress in the Solid Electrolyte Interphase on Carbon Electrodes for Li Ion Batteries, *Journal of The Electrochemical Society*. 161 (2014) A58–A65. doi:10.1149/2.009401jes.
- [140] N.D. Lepley, N.A.W. Holzwarth, Y. a. Du, Structures, Li⁺ mobilities, and interfacial properties of solid electrolytes Li₃PS₄ and Li₃PO₄ from first principles, *Physical Review B*. 88 (2013) 104103. doi:10.1103/PhysRevB.88.104103.
- [141] H. Gerischer, Fermi levels in electrolytes and the absolute scale of redox potentials, *Applied Physics Letters*. 43 (1983) 393. doi:10.1063/1.94356.
- [142] A.J. Bard, A.B. Bocarsly, F.R.F. Fan, E.G. Walton, M.S. Wrighton, The concept of Fermi level pinning at semiconductor/liquid junctions. Consequences for energy conversion efficiency and selection of useful solution redox couples in solar devices, *Journal of the American Chemical Society*. 102 (1980) 3671–3677. doi:10.1021/ja00531a001.
- [143] M. Razavy, *Quantum Theory of Tunneling*. Singapore, SGP: World Scientific Publishing Co., 2003. ProQuest ebrary. Web. 3 November 2015. Copyright © 2003. World Scientific Publishing Co.. All rights reserved., n.d.
- [144] lithium-fluoride-lif-data-sheet.pdf, (n.d.). www.crystran.co.uk/userfiles/files/lithium-fluoride-lif-data-sheet.pdf.
- [145] A. Kiejna, J. Peisert, P. Scharoch, Quantum-size effect in thin Al (110) slabs, *Surface Science*. 432 (1999) 54–60. doi:10.1016/S0039-6028(99)00510-5.
- [146] S. Baskoutas, A.F. Terzis, Size-dependent band gap of colloidal quantum dots, *Journal of Applied Physics*. 99 (2006) 013708. doi:10.1063/1.2158502.
- [147] L. Lin, Z. Li, J. Feng, Z. Zhang, Indirect to direct band gap transition in ultra-thin silicon films., *Physical Chemistry Chemical Physics: PCCP*. 15 (2013) 6063–7. doi:10.1039/c3cp50429h.
- [148] P.T. Salo, R. Laihia, K. Mansikka, First-principles calculations for work function and surface energy of thin lithium films, *Surface Science*. 348 (1996) 168–174.
- [149] S.J. Binnie, *Ab initio surface energetics: beyond chemical accuracy*, University College London, 2011. <http://discovery.ucl.ac.uk/1318067/>.

- [150] M. Stossel, J. Staudigel, F. Steuber, J. Simmerer, A. Winnacker, Impact of the Cathode Metal Work Function on the Performance of Vacuum-Deposited Organic Light Emitting Devices, *Appl. Phys. A - Mater.* 68 (1999) 387–390. doi:10.1007/s003399900011.
- [151] J.E. Saal, S. Kirklin, M. Aykol, B. Meredig, C. Wolverton, Materials design and discovery with high-throughput density functional theory: The open quantum materials database (OQMD), *Jom.* 65 (2013) 1501–1509. doi:10.1007/s11837-013-0755-4.
- [152] Y.-N. Xu, Comparative studies of the electronic structure of LiFePO₄, FePO₄, Li₃PO₄, LiMnPO₄, LiCoPO₄, and LiNiPO₄, *Journal of Applied Physics.* 95 (2004) 6583. doi:10.1063/1.1667422.
- [153] A. Zunger, A.J. Freeman, Ground- and excited-state properties of LiF in the local-density formalism, *Physical Review B.* 16 (1977) 2901–2926. doi:10.1103/PhysRevB.16.2901.
- [154] B. Delley, E.F. Steigmeier, Size dependence of band gaps in silicon nanostructures, *Applied Physics Letters.* 67 (1995) 2370. doi:10.1063/1.114348.
- [155] S.Q. Wu, Z.F. Hou, Z.Z. Zhu, First-principles study on the structural, elastic, and electronic properties of γ -LiAlO₂, *Computational Materials Science.* 46 (2009) 221–224. doi:10.1016/j.commatsci.2009.02.028.
- [156] P. Scharoch, M. Winiarski, An efficient method of DFT/LDA band-gap correction, *Computer Physics Communications.* 184 (2013) 2680–2683. doi:10.1016/j.cpc.2013.07.008.
- [157] R.C. Chaney, E.E. Lafon, C.C. Lin, Energy Band Structure of Lithium Fluoride Crystals by the Method of Tight Binding, *Physical Review B.* 4 (1971) 2734. doi:10.1103/PhysRevB.4.2734.
- [158] M. Piacentini, D.W. Lynch, C.G. Olson, Thermoreflectance of LiF between 12 and 30 eV, *Physical Review B.* 13 (1976) 5530–5543. doi:10.1103/PhysRevB.13.5530.
- [159] D. Roessler, W. Walker, Optical Constants of Magnesium Oxide and Lithium Fluoride in the Far Ultraviolet, *J. Phys. Chem. Solids.* 28 (1967) 1507–1509. doi:10.1364/JOSA.57.000835.
- [160] M.G. Silveirinha, C.A. Fernandes, A Hybrid Method for the Efficient Calculation of the Band Structure of 3-D Metallic Crystals, *IEEE Transactions on Microwave Theory and Techniques.* 52 (2004) 889–902. doi:10.1109/TMTT.2004.823563.

- [161] F. Tran, P. Blaha, Accurate band gaps of semiconductors and insulators with a semilocal exchange-correlation potential, *Physical Review Letters*. 102 (2009) 5–8. doi:10.1103/PhysRevLett.102.226401.
- [162] M. Vos, G.G. Marmitt, Y. Finkelstein, R. Moreh, Determining the band gap and mean kinetic energy of atoms from reflection electron energy loss spectra, *The Journal of Chemical Physics*. 143 (2015) 104203. doi:10.1063/1.4929911.
- [163] J. Shim, R. Kostecky, T. Richardson, X. Song, K.A. Striebel, Electrochemical analysis for cycle performance and capacity fading of a lithium-ion battery cycled at elevated temperature, *Journal of Power Sources*. 112 (2002) 222–230. doi:10.1016/S0378-7753(02)00363-4.
- [164] P. Novák, J. Ufheil, H. Buqa, F. Krumeich, M.E. Spahr, D. Goers, et al., The importance of the active surface area of graphite materials in the first lithium intercalation, *Journal of Power Sources*. 174 (2007) 1082–1085. doi:10.1016/j.jpowsour.2007.06.036.
- [165] D. Aurbach, B. Markovsky, I. Weissman, E. Levi, Y. Ein-Eli, On the correlation between surface chemistry and performance of graphite negative electrodes for Li ion batteries, *Electrochimica Acta*. 45 (1999) 67–86. doi:10.1016/S0013-4686(99)00194-2.
- [166] M.J. van Setten, V.A. Popa, G.A. de Wijs, G. Brocks, Electronic structure and optical properties of lightweight metal hydrides, *Phys. Rev. B*. 75 (2007) 035204. doi:10.1103/PhysRevB.75.035204.
- [167] S.S. Zhang, K. Xu, T.R. Jow, EIS study on the formation of solid electrolyte interface in Li-ion battery, *Electrochimica Acta*. 51 (2006) 1636–1640. doi:10.1016/j.electacta.2005.02.137.
- [168] S. Jiao, J. Zheng, Q. Li, X. Li, M.H. Engelhard, R. Cao, et al., Behavior of Lithium Metal Anodes under Various Capacity Utilization and High Current Density in Lithium Metal Batteries, *Joule*. 2 (2018) 110–124. doi:10.1016/j.joule.2017.10.007.
- [169] L. Qie, W.M. Chen, Z.H. Wang, Q.G. Shao, X. Li, L.X. Yuan, et al., Nitrogen-doped porous carbon nanofiber webs as anodes for lithium ion batteries with a superhigh capacity and rate capability, *Advanced Materials*. 24 (2012) 2047–2050. doi:10.1002/adma.201104634.
- [170] B. Zhang, X. Qin, G.R. Li, X.P. Gao, Enhancement of long stability of sulfur cathode by encapsulating sulfur into micropores of carbon spheres, *Energy & Environmental Science*. 3 (2010) 1531. doi:10.1039/c002639e.

- [171] A. Rosenman, E. Markevich, G. Salitra, Y. Talyosef, F. Chesneau, D. Aurbach, Facile synthesis and very stable cycling of polyvinylidene dichloride derived carbon: sulfur composite cathode, *Journal of The Electrochemical Society*. 163 (2016) A1829–A1835. doi:10.1149/2.0151609jes.
- [172] O. Ogoke, G. Wu, X. Wang, A. Casimir, L. Ma, T. Wu, et al., Effective strategies for stabilizing sulfur for advanced lithium–sulfur batteries, *J. Mater. Chem. A*. 5 (2017) 448–469. doi:10.1039/C6TA07864H.
- [173] D.-W. Wang, G. Zhou, F. Li, K.-H. Wu, G.Q. (Max) Lu, H.-M. Cheng, et al., A microporous–mesoporous carbon with graphitic structure for a high-rate stable sulfur cathode in carbonate solvent-based Li–S batteries, *Physical Chemistry Chemical Physics*. 14 (2012) 8703. doi:10.1039/c2cp40808b.
- [174] Y. Xu, Y. Wen, Y. Zhu, K. Gaskell, K.A. Cychosz, B. Eichhorn, et al., Confined sulfur in microporous carbon renders superior cycling stability in Li/S batteries, *Advanced Functional Materials*. 25 (2015) 4312–4320. doi:10.1002/adfm.201500983.
- [175] J. Chen, K.S. Han, W.A. Henderson, K.C. Lau, M. Vijayakumar, T. Dzwiniel, et al., Restricting the solubility of polysulfides in Li-S batteries via electrolyte salt selection, *Advanced Energy Materials*. 6 (2016) 1–6. doi:10.1002/aenm.201600160.
- [176] B. Wang, S.M. Alhassan, S.T. Pantelides, Formation of large polysulfide complexes during the lithium-sulfur battery discharge, *Physical Review Applied*. 2 (2014) 1–7. doi:10.1103/PhysRevApplied.2.034004.
- [177] R.S. Assary, L.A. Curtiss, J.S. Moore, Toward a molecular understanding of energetics in Li-S batteries using nonaqueous electrolytes: A high-level quantum chemical study, *Journal of Physical Chemistry C*. 118 (2014) 11545–11558. doi:10.1021/jp5015466.
- [178] L.E. Camacho-Forero, T.W. Smith, S. Bertolini, P.B. Balbuena, Reactivity at the lithium-metal anode surface of lithium-sulfur batteries, *Journal of Physical Chemistry C*. 119 (2015) 26828–26839. doi:10.1021/acs.jpcc.5b08254.
- [179] J.J. Chen, R.M. Yuan, J.M. Feng, Q. Zhang, J.X. Huang, G. Fu, et al., Conductive lewis base matrix to recover the missing link of Li₂S₈ during the sulfur redox cycle in Li-S battery, *Chemistry of Materials*. 27 (2015) 2048–2055. doi:10.1021/cm5044667.
- [180] P. Canepa, S. Jayaraman, L. Cheng, N.N. Rajput, W.D. Richards, G.S. Gautam, et al., Elucidating the structure of the magnesium aluminum chloride complex electrolyte for magnesium-ion batteries, *Energy & Environmental Science*. 8 (2015) 3718–3730.

doi:10.1039/C5EE02340H.

- [181] Q. Wang, J. Zheng, E. Walter, H. Pan, D. Lv, P. Zuo, et al., Direct observation of sulfur radicals as reaction media in lithium sulfur batteries, *Journal of the Electrochemical Society*. 162 (2015) A474–A478. doi:10.1149/2.0851503jes.
- [182] T. Gao, M. Noked, A.J. Pearse, E. Gillette, X. Fan, Y. Zhu, et al., Enhancing the reversibility of Mg/S battery chemistry through Li⁺ mediation, *Journal of the American Chemical Society*. 137 (2015) 12388–12393. doi:10.1021/jacs.5b07820.
- [183] B. Delley, An all electron numerical method for solving the local density functional for polyatomic molecules, *J. Chem. Phys. Additional Information on J. Chem. Phys. Journal Homepage*. 92 (1990). doi:10.1063/1.458452.
- [184] B. Delley, From molecules to solids with the DMol3 approach, *The Journal of Chemical Physics*. 113 (2000) 7756–7764. doi:10.1063/1.1316015.
- [185] J.P. Perdew, Y. Wang, Accurate and simple analytic representation of the electron-gas correlation energy, *Phys. Rev. B*. 45 (1992) 244–249.
- [186] J.P. Stewart, *MOPAC Manual (Seventh Edition)*, 1993.
- [187] P.E. Blöchl, Projector augmented-wave method, *Physical Review B*. 50 (1994) 17953–17979. doi:10.1103/PhysRevB.50.17953.
- [188] J.P. Perdew, K. Burke, M. Ernzerhof, Generalized gradient approximation made simple, *Physical Review Letters*. 77 (1996) 3865–3868. doi:10.1103/PhysRevLett.77.3865.
- [189] K. Leung, C.M. Tenney, Toward first principles prediction of voltage dependences of electrolyte/electrolyte interfacial processes in lithium ion batteries, *Journal of Physical Chemistry C*. 117 (2013) 24224–24235. doi:10.1021/jp408974k.
- [190] A. Klamt, G. Schüürmann, COSMO: a new approach to dielectric screening in solvents with explicit expressions for the screening energy and its gradient, *J. Chem. Soc., Perkin Trans. 2*. (1993) 799–805. doi:10.1039/P29930000799.
- [191] M. Cossi, N. Rega, G. Scalmani, V. Barone, Energies, structures, and electronic properties of molecules in solution with the C-PCM solvation model, *Journal of Computational Chemistry*. 24 (2003) 669–681. doi:10.1002/jcc.10189.
- [192] S. Yanase, T. Oi, Solvation of lithium ion in organic electrolyte solutions and its isotopic reduced partition function ratios studied by ab initio molecular orbital method, *Journal of*

- Nuclear Science and Technology. 39 (2002) 1060–1064. doi:10.1080/18811248.2002.9715294.
- [193] Y. Li, K. Leung, Y. Qi, Computational exploration of the Li-electrode|electrolyte interface in the presence of a nanometer thick solid-electrolyte interphase layer, *Accounts of Chemical Research*. 49 (2016) 2363–2370. doi:10.1021/acs.accounts.6b00363.
- [194] I. Skarmoutsos, V. Ponnuchamy, V. Vetere, S. Mossa, Li⁺ solvation in pure, binary, and ternary mixtures of organic carbonate electrolytes, *Journal of Physical Chemistry C*. 119 (2015) 4502–4515. doi:10.1021/jp511132c.
- [195] M. Shakourian-Fard, G. Kamath, K. Smith, H. Xiong, S.K.R.S. Sankaranarayanan, Trends in Na-ion solvation with alkyl-carbonate electrolytes for sodium-ion batteries: insights from first-principles calculations, *Journal of Physical Chemistry C*. 119 (2015) 22747–22759. doi:10.1021/acs.jpcc.5b04706.
- [196] B. Jiang, V. Ponnuchamy, Y. Shen, X. Yang, K. Yuan, V. Vetere, et al., The anion effect on Li⁺ ion coordination structure in ethylene carbonate solutions, *Journal of Physical Chemistry Letters*. 7 (2016) 3554–3559. doi:10.1021/acs.jpcclett.6b01664.
- [197] A. Warshel, S.T. Russell, Calculations of electrostatic interactions in biological systems and in solutions, *Q. Rev. Biophys.* 17 (1984) 283–422.
- [198] D. Meyerstein, A clathrate hydrate of 1,3-dioxolanel, *Canadian Journal of Chemistry*. 45 (1967) 884–886.
- [199] H. Sun, COMPASS: An ab Initio Force-Field Optimized for Condensed-Phase Applications Overview with Details on Alkane and Benzene Compounds, *J Phys Chem B*. 102 (1998) 7338–7364. doi:10.1021/jp980939v.
- [200] S. Nosé, A molecular dynamics method for simulations in the canonical ensemble, *Molecular Physics*. 52 (1984) 255–268. doi:10.1080/00268978400101201.
- [201] H.J.C. Berendsen, J.P.M. Postma, W.F. Van Gunsteren, A. Dinola, J.R. Haak, Molecular dynamics with coupling to an external bath, *The Journal of Chemical Physics*. 81 (1984) 3684–3690. doi:10.1063/1.448118.
- [202] I.A. Courtney, J.S. Tse, O. Mao, J. Hafner, J.R. Dahn, Ab initio calculation of the lithium-tin voltage profile, *Physical Review B - Condensed Matter and Materials Physics*. 58 (1998) 15583–15588. doi:10.1103/PhysRevB.58.15583.

- [203] Z. Liu, S. Bertolini, P.B. Balbuena, P.P. Mukherjee, Li₂S film formation on lithium anode surface of Li-S batteries, *ACS Applied Materials and Interfaces*. 8 (2016) 4700–4708. doi:10.1021/acsami.5b11803.
- [204] M. Barghamadi, A. Kapoor, C. Wen, A Review on Li-S Batteries as a High Efficiency Rechargeable Lithium Battery, *Journal of The Electrochemical Society*. 160 (2013) A1256–A1263. doi:10.1149/2.096308jes.
- [205] X. Tao, J. Wan, C. Liu, H. Wang, H. Yao, G. Zheng, et al., Balancing surface adsorption and diffusion of lithium-polysulfides on nonconductive oxides for lithium-sulfur battery design, *Nature Communications*. 7 (2016) 1–9. doi:10.1038/ncomms11203.
- [206] Z. Li, Y. Huang, L. Yuan, Z. Hao, Y. Huang, Status and prospects in sulfur-carbon composites as cathode materials for rechargeable lithium-sulfur batteries, *Carbon*. 92 (2015) 41–63. doi:10.1016/j.carbon.2015.03.008.
- [207] Z. Li, Y. Jiang, L. Yuan, Z. Yi, C. Wu, Y. Liu, et al., A highly ordered Meso@microporous carbon-supported Sulfur@smaller sulfur core-shell structured cathode for Li-s batteries, *ACS Nano*. 8 (2014) 9295–9303. doi:10.1021/nn503220h.
- [208] M.J. Klein, G.M. Veith, A. Manthiram, Rational Design of Lithium-Sulfur Battery Cathodes Based on Experimentally Determined Maximum Active Material Thickness, *Journal of the American Chemical Society*. 139 (2017) 9229–9237. doi:10.1021/jacs.7b03380.
- [209] C. Weller, S. Thieme, P. Härtel, H. Althues, S. Kaskel, Intrinsic Shuttle Suppression in Lithium-Sulfur Batteries for Pouch Cell Application, *Journal of The Electrochemical Society*. 164 (2017) A3766–A3771. doi:10.1149/2.0981714jes.
- [210] USABC Goals for Advanced Batteries for EVs., n.d.
- [211] C. Park, M. Kanduč, R. Chudoba, A. Ronneburg, S. Risse, M. Ballauff, et al., Molecular simulations of electrolyte structure and dynamics in lithium–sulfur battery solvents, *Journal of Power Sources*. 373 (2018) 70–78. doi:10.1016/j.jpowsour.2017.10.081.
- [212] K. Hayamizu, Y. Aihara, S. Arai, C.G. Martinez, Pulse-Gradient Spin-Echo ¹H, ⁷Li, and ¹⁹F NMR Diffusion and Ionic Conductivity Measurements of 14 Organic Electrolytes Containing LiN(SO₂CF₃)₂, *The Journal of Physical Chemistry B*. 103 (2002) 519–524. doi:10.1021/jp9825664.
- [213] G. Li, W. Cai, B. Liu, Z. Li, A multi functional binder with lithium ion conductive polymer and polysulfide absorbents to improve cycleability of lithium-sulfur batteries,

- Journal of Power Sources. 294 (2015) 187–192. doi:10.1016/j.jpowsour.2015.06.083.
- [214] C. Noiriél, L. Luquot, B. Madé, L. Raimbault, P. Gouze, J. van der Lee, Changes in reactive surface area during limestone dissolution: An experimental and modelling study, *Chemical Geology*. 262 (2009) 353–363. doi:10.1016/j.chemgeo.2009.01.032.
- [215] N. Gavish, K. Promislow, Dependence of the dielectric constant of electrolyte solutions on ionic concentration: A microfield approach, *Physical Review E*. 94 (2016) 1–7. doi:10.1103/PhysRevE.94.012611.
- [216] W.-J. Zhang, A review of the electrochemical performance of alloy anodes for lithium-ion batteries, *Journal of Power Sources*. 196 (2011) 13–24. doi:10.1016/j.jpowsour.2010.07.020.
- [217] S. Homaeigohar, M. Elbahri, Graphene membranes for water desalination, *Nature Publishing Group*. (2017) 1–16. doi:10.1038/am.2017.135.
- [218] J.T. Lee, K. Eom, F. Wu, H. Kim, D.C. Lee, B. Zdyrko, et al., Enhancing the stability of sulfur cathodes in Li-S cells via in situ formation of a solid electrolyte layer, *ACS Energy Letters*. 1 (2016) 373–379. doi:10.1021/acsenerylett.6b00163.
- [219] P.G. Bruce, S. a. Freunberger, L.J. Hardwick, J.-M. Tarascon, Li–O₂ and Li–S batteries with high energy storage, *Nature Materials*. 11 (2011) 172–172. doi:10.1038/nmat3237.
- [220] M. Helen, M.A. Reddy, T. Diemant, U. Golla-Schindler, R.J. Behm, U. Kaiser, et al., Single step transformation of sulphur to Li₂S₂/Li₂S in Li-S batteries, *Scientific Reports*. 5 (2015) 12146. doi:10.1038/srep12146.
- [221] Y. Lin, J. Zheng, C. Wang, Y. Qi, Origin of the two-plateaued or one-plateaued open circuit voltage in Li / S batteries from first principle calculation, Submitted. (n.d.).
- [222] D.J. Mann, W.L. Hase, Direct dynamics simulations of the oxidation of a single wall carbon nanotube, *Physical Chemistry Chemical Physics*. 3 (2001) 4376–4383. doi:10.1039/b103762p.
- [223] A. Bagri, C. Mattevi, M. Acik, Y.J. Chabal, M. Chhowalla, V.B. Shenoy, Structural evolution during the reduction of chemically derived graphene oxide., *Nature Chemistry*. 2 (2010) 581–587. doi:10.1038/nchem.686.
- [224] S.Y. Kim, A.C.T. Van Duin, J.D. Kubicki, Molecular dynamics simulations of the interactions between TiO₂ nanoparticles and water with Na⁺ and Cl⁻, methanol, and formic acid using a reactive force field, *Journal of Materials Research*. 28 (2013) 513–

520. doi:10.1557/jmr.2012.367.

- [225] C.Y. Wang, G. Zhang, S. Ge, T. Xu, Y. Ji, X.G. Yang, et al., Lithium-ion battery structure that self-heats at low temperatures, *Nature*. 529 (2016) 515–518. doi:10.1038/nature16502.
- [226] M.C. Smart, B. V. Ratnakumar, L.D. Whitcanack, K.B. Chin, S. Surampudi, H. Croft, et al., Improved low-temperature performance of lithium-ion cells with quaternary carbonate-based electrolytes, *Journal of Power Sources*. 119–121 (2003) 349–358. doi:10.1016/S0378-7753(03)00154-X.
- [227] E.J. Plichta, M. Hendrickson, R. Thompson, G. Au, W.K. Behl, M.C. Smart, et al., Development of low temperature Li-ion electrolytes for NASA and DoD applications, *Journal of Power Sources*. 94 (2001) 160–162. doi:10.1016/S0378-7753(00)00578-4.
- [228] J. Qian, W.A. Henderson, W. Xu, P. Bhattacharya, M. Engelhard, O. Borodin, et al., High rate and stable cycling of lithium metal anode, *Nature Communications*. 6 (2015) 6362. doi:10.1038/ncomms7362.
- [229] N.L. Cheng, *Solvents Handbook*, 4th ed., Chemical Industry Press, 2007.